Astrophysical Applications of Quantum Mechanics

Thesis by
Elena M. Murchikova

In Partial Fulfillment of the Requirements for the
Degree of
Doctor of Philosophy

Caltech

CALIFORNIA INSTITUTE OF TECHNOLOGY
Pasadena, California

2018
Defended May 29, 2018

ACKNOWLEDGEMENTS

ABSTRACT

From an outside point of view, astrophysics and quantum mechanics as sub-classes of the physical sciences could not be further from each other. Yet these two sides of nature are deeply intertwined. The influence of quantum mechanics on astrophysics and astrophysics on quantum mechanics has been profound: spectral lines as diagnostics, radiative transport, the interiors of celestial bodies, neutrino oscillations, constraints on neutrino mass and graviton mass. In this work, I discuss several applications of quantum mechanics in astrophysics: (1) I examine the use of submm recombination lines of H, He and He$^+$ to probe the extreme ultraviolet luminosity of starbursts and Active Galactic Nuclei. (2) I use the hydrogen recombination line H30α to study the accretion zone of the Milky Way's Galactic Center black hole. I discuss detection of an accretion disk of radius <0.008 pc, consisting of $\sim 10^4$ K gas the disk properties, and its importance in the context of accretion on the black hole. (3) I carry out an extensive study and comparison of M1 closure schemes for neutrino radiation transport, using the protoneutron star interior as a background. (4) I study first-order hydrodynamics of a chiral fluid on a vortex background, and in an external magnetic field, as the precursor for a study of neutron star interiors. I show that there are two previously undiscovered modes describing heat waves propagating along the vortex and magnetic field.

PUBLISHED CONTENT AND CONTRIBUTIONS

Nick Scoville, and Lena Murchikova,
"Submm Recombination Lines in Dust-Obscured Starbursts and AGN,"
The Astrophysical Journal,
Volume 779, Issue 1, article id. 75, 12 pp. (2013).

I performed all of the quantum mechanical calculations presented in detail and the Appendices and used in the body of the paper, independently conducted all calculations, derived the scaling of the emissivities with the electron temperature, wrote the Appendices and made the plot for it, and calculated the data used for making Figure 2.4 (the data plotted in most other figures is taken from Storey & Hummer (1995b)).

E. M. Murchikova, E. Abdikamalov, and T. Urbatsch,
"Analytic Closures for M1 Neutrino Transport",
Monthly Notices of the Royal Astronomical Society,
Volume 469, Issue 2, Pages 1725 –1737 (2017).

I performed the numerical calculation, developed the closure comparison technique and coded them in Python, made modification to existing codes to include the closure relations, derived analytical relations, and wrote 90% the paper.

Tigran Kalaydzhyan, and Elena Murchikova,
"Thermal chiral vortical and magnetic waves:
new excitation modes in chiral fluids",
Nuclear Physics B, 919 (2017) 173–181.

The order of authors is alphabetic. The authors equally contributed to the paper. I proposed the project, independently conducted all calculations as did the co-author, and wrote 50% of the paper.

TABLE OF CONTENTS

LIST OF ILLUSTRATIONS

LIST OF TABLES

C h a p t e r   1

ASTROPHYSICAL APPLICATIONS OF QUANTUM MECHANICS

1.1   Introduction

From an outside point of view, astrophysics and quantum mechanics as sub-classes of the physical sciences could not be further from each other. One deals with scales like the solar masses $M_\odot \sim 10^{33}$ g and the parsecs $\mathrm{pc} = 3 \times 10^{18}$ cm the other with the electron masses $m_e \sim 10^{-27}$ g and the Bohr radii $a_0 \sim 5 \times 10^{-9}$ cm. Yet these two sides of nature are deeply intertwined.

McCrea (1950) reviewed quantum mechanical contributions to astrophysics and concluded that there were not many. Almost 70 years later we here make an attempt at a brief update on the subject. This update by no means claims to be comprehensive. It only mentions the most prominent contributions such as spectral lines, descriptions of the interiors of celestial bodies, neutrino oscillations, and constraints on the masses of elementary particles.

We do not discuss cosmology here mainly because covering this topic thoroughly would require a separate thesis. We only mention that today's cosmology is inseparable from quantum field theory and cannot be taught without it (Baumann, 2013).

1.2   Spectral lines

In the second half of 19th century astronomers embraced spectroscopy and photography, which revolutionized the field. At first, they relied on laboratory-produced spectra of the elements and matched them with the lines seen in the stars. With the development of quantum mechanics, it became possible to calculate atomic and molecular transitions.

Modern astronomy is virtually impossible without spectroscopy and radiative transport calculations. Spectral lines are used to study virtually everything from stars and galaxies to molecular clouds and intergalactic medium. Spectral lines and their profiles carry the information about the composition, temperature, density, magnetic fields and redshift of astronomical objects.

The first and the only chemical element discovered using an astronomical object was helium, first seen in the spectra of the Sun. It was first observed by

Jules Janssen during a total solar eclipse on August 18, 1868, as a bright yellow (587.49 nm) line in the spectrum of the chromosphere of the Sun (Kochhar, 1991). The same year in on October 20 Norman Lockyer observed a yellow line in the solar spectrum (Lockyer, 1868) and concluded that it is from a chemical element in the Sun unknown on Earth. Together with chemist Edward Frankland, they named it after Helios, the Sun in Greek (Thomson, 1871). Helium was discovered on Earth in 1895 by Per Teodor Cleve and Nils Abraham Langlet. It was emanating from a crystalline variety of the mineral uraninite. Large reserves of helium were found in natural gas fields in the United States in 1903.

Further attempts to find chemical elements unknown on Earth were less successful. "Nebulium" lines (Huggins & Miller, 1864) ended up being the forbidden transitions of ionized O, N, and Ne (Bowen, 1927), while "Coronium" lines (Gruenwald, 1887) turned out to be the forbidden transitions of highly ionized Fe, Ni, Ca, and Ar, as identified by Walter Grotrian and Bengt Edlen (Morison, 2008). These lines are only strong enough to be detectable at extremely low densities unattainable on Earth.

If not new chemical elements, new molecules and materials are certainly expected to be in the outer space. The study of unidentified infrared emission (UIR) bands – a prominent emission with the main features at around 3.3, 6.2, 7.7, 8.6, 11.2, and 12.7 μm from presumably unknown complex molecules with aromatic C−H and C=C chemical bonds (Leger & Puget, 1984) became a whole field in astrophysics. For a long time it was believed that the materials responsible should be polycyclic aromatic hydrocarbon (PAH) molecules (Allamandola et al., 1989). However recent data from ESA's Infrared Space Observatory and NASA's Spitzer Space Telescope suggests that the UIR emission bands arise from compounds that are far more complex in composition and structure than PAH molecules (Kwok & Zhang, 2011). These unknown spectral features wait to be produced in model spectra of newly synthesised in the laboratory or in the simulations molecules or proven to be a previously unknown excitation mode of known complex molecules. After all, materials unknown on Earth are known to be created in the other parts of the universe, such as the forbidden 5-fold crystals found in meteorites (Bindi et al., 2016).

1.3 Interiors of astrophysical bodies

Since the mid-1920s, when Ralph H. Fowler first applied quantum degeneracy to explaining characteristics of white-dwarfs (Fowler, 1926), quantum theory

has played a prominent role in describing the internal structure of the celestial bodies. Electron degeneracy pressure prevents gas giants like Jupiter from igniting nuclear fusion in their cores and prevents white-dwarfs from collapsing. The interior of stars is composed of multiple zones in which various stages of nuclear burning determine the star's radius, luminosity, and internal structure.

We owe our own existence to the nuclear burning (Burbidge et al., 1957). The three out of four atoms of life oxygen, hydrogen, carbon, nitrogen are produced inside stars. A great amount of these elements sufficient to produce life in the Universe and the fact that they are not converted into heavier elements are due to (1) the existence of an excites state of ^{8}Be, which is almost exactly the energy of two alpha particles, allowing them to fuse directly, (2) the existence of an excites state of ^{12}C, which is almost exactly the energy of ^{8}Be and an alpha particle, allowing them to fuse directly, and (3) the absence of such a state for oxygen in reaction ^{12}C + ^{4}He $\rightarrow$ ^{16}O, preventing convertion of too much C into O. The resonance state of ^{12}C at 7.68 MeV was predicted by Hoyle, in order for enough carbon to be formed in stars, and later discovered experimentally (Dunbar et al., 1953). The existence of the excited state of ^{8}Be was confirmed by Salpeter (1952).

The other aspect of the influence of the quantum world on astrophysical objects lies in the domain of dense matter. On Earth producing matter at above nuclear density requires heavy ion collisions and was accomplished on Brookhaven National Laboratory's Relativistic Heavy Ion Collider and CERN's Large Hadron Collider (Pb-Pb runs). In the colliders the state lasts only a tiny fraction of a second and is hot. In celestial bodies, such matter is routinely encountered in both cold and hot states. It comprises substantial fraction of a neutron star's interior. The difficulties involved in obtaining matter above nuclear density in laboratory conditions complicate direct experiments resulting in the greatly uncertain equations of state of neutron stars (see for example Richers et al. (2017)).

The uncertainty in equations of state describing interiors of compact objects (excluding black holes), influences their mass-radius relations, evolution, collapse, the very ability of the star to go supernovae, the gravitational wave signal from core-collapse supernovae, and more. Breakthroughs are yet to come here, and the hopes largely lie in astrophysical observations.

1.4 Neutrino oscillations

Bahcall (1964) and Davis (1964) proposed testing the Solar model using a neutrino detector. "When we started the Homestake solar neutrino experiment, we thought we understood how the Sun worked and that a measurement of the solar neutrino flux would confirm the theory. This clearly did not turn out as planned," wrote Ray Davis in his Nobel lecture. Indeed the observations robustly showed that only $\frac{1}{3}$ of the expected neutrino flux from the Sun was detected on Earth (Davis et al., 1968). Theorists considered the discrepancy an experimental error, while experimentalists blamed astrophysics uncertainties. Yet no serious mistakes were found on either side. The solar neutrino problem prompted/revived interest in neutrino oscillations, and was completely resolved in the early 2000s when SNO Collaboration confirmed the appearance of ν_μ and ν_τ in the solar neutrino flux (Ahmad et al., 2002) and the KamLAND collaboration confirmed the disappearance of ν_e from terrestrial reactors (Eguchi et al., 2003).

1.5 Constrains on neutrino mass and graviton mass

The great distance from astrophysical events to the observer on Earth affords us an opportunity to constrain the mass of the elementary particles by measuring the lag between the arrival of the signal at different locations or the lag between the arrival of the signals of different carriers.

Arnett & Rosner (1987) set a limit on neutrino mass at $m_\nu < 12\,\mathrm{eV}$ by measuring the difference between the time of arrival of the neutrinos from the supernova 1987A at Kamiokande and IMB detectors.[1]

Using a similar technique: measuring the difference between the time of arrival of the gravitational signal at Hanford and Livingston detectors, LIGO has put an upper limit on the mass of graviton at $1.2 \times 10^{-22}\,\mathrm{eV}$ (Abbott et al., 2016).

1.6 In this thesis

In this work, I discuss several applications of quantum mechanics to astrophysics:

In Chapter 2 we examine the use of submm and mm recombination lines of H, He and He$^+$ to probe the extreme ultraviolet (EUV) luminosity of starbursts and Active Galactic Nuclei. We find that the mm-submm recombination lines

---

[1] If only the neutrino observatories had high-precision clocks the limit would have been much stronger.

of H, He and He$^+$ are in fact extremely reliable and quantitative probes of the EUV continuum at 13.6 eV to above 54.6 eV.

In Chapter 3 we put the result of Chapter 2 to the test and investigate the accretion zone of the Milky Way's Galactic Center black hole – Sagittarius A* – in the hydrogen recombination line H30α. The Galactic Center black hole is the nearest supermassive black hole and thus provides a unique opportunity for observing the black hole's immediate environment and accretion. We detected and spatially resolved an accretion disk of radius <0.008 pc, consisting of $\sim 10^4$ K gas. Previous work has found only X-ray emitting quasi-spherical hot gas at much larger radii, and nonthermal synchrotron-emitting electrons. We discuss the properties of the disk and their importance in the context of accretion on Sagittarius A*.

Chapter 4 is dedicated to the problem of neutrino transport. Carefully accounting for neutrino transport is an essential component of many astrophysical studies particularly in supernovae and collisions of neutron stars. Solving the full transport equation is too expensive for most realistic applications, especially those involving multiple spatial dimensions. For such cases, resorting to approximations is often the only viable option for obtaining solutions. One such approximation, which recently became popular, is the M1 method. It utilizes the system of the lowest two moments of the transport equation and closes the system with an ad hoc closure relation. The accuracy of the M1 solution depends on the quality of the closure. Several closures have been proposed in the literature and have been used in various studies. We perform an extensive study and quantitative comparison of these closures We compare the results of M1 calculations with precise Monte Carlo calculations of the radiation field around spherically-symmetric protoneutron star models. We find that no closure performs consistently better or worse than others in all cases. The level of accuracy of a given closure depends on the matter configuration, neutrino type, and neutrino energy. Given this limitation, the maximum entropy closure by Minerbo yields accurate results in the broadest set of cases considered in this work.

In Chapter 5 we discuss the properties of chiral fluids. In certain circumstances, chiral (parity-violating) medium can be described hydrodynamically as a chiral fluid with microscopic quantum anomalies. Possible examples of such systems include strongly coupled quark-gluon plasma, liquid helium ^{3}He-A, neutron stars and the Early Universe. We study the first-order hydrodynamics of a

chiral fluid on a vortex background and in an external magnetic field. We show that there are two previously undiscovered modes describing heat waves propagating along the vortex and magnetic field. This chapter is a first step of a program to use chiral fluid to describe (a part of) the neutron star interior, which is a long-term goal of the author.

Chapter 2

SUBMM RECOMBINATION LINES IN DUST-OBSCURED STARBURSTS AND AGN

We examine the use of submm recombination lines of H, He, and He$^+$ to probe the extreme ultraviolet (EUV) luminosity of starbursts (SB) and AGN. We find that the submm recombination lines of H, He, and He$^+$ are in fact extremely reliable and quantitative probes of the EUV continuum at 13.6 eV to above 54.6 eV. At submm wavelengths, the recombination lines originate from low energy levels (n = 20 – 50). The maser amplification, which poses significant problems for quantitative interpretation of the higher n, radio frequency recombination lines, is insignificant. Lastly, at submm wavelengths the dust extinction is minimal. The submm line luminosities are therefore directly proportional to the emission measures ($\mathbf{EM}_{\mathrm{ion}} = n_e \times n_{\mathrm{ion}} \times \mathbf{vol}$) of their ionized regions. We also find that the expected line fluxes are detectable with ALMA and can be imaged at $\sim 0.1''$ resolution in low redshift ULIRGs. Imaging of the HI lines will provide accurate spatial and kinematic mapping of the star formation distribution in low-z IR-luminous galaxies. And the relative fluxes of the HI and HeII recombination lines will strongly constrain the relative contributions of starbursts and AGN to the luminosity. The HI lines should also provide an avenue to constraining the submm dust extinction curve.

2.1   Introduction

The most energetic periods of evolution in galaxies are often highly obscured by dust at short wavelengths, with the luminosity reradiated in the far infrared. Merging of galaxies will concentrate the interstellar gas and dust (ISM) in the nucleus since the gas is very dissipative where it can fuel a nuclear starburst or AGN. The Ultraluminous Infrared Galaxies (ULIRGs) and Submm Galaxies (SMGs) emit nearly all their radiation in the far infrared (Carilli & Walter, 2013; Sanders et al., 1988). Although their power originates as visible, UV and X-ray photons, the emergent IR continuum only weakly differentiates the power source(s) – starburst or AGN – and their relative contributions. This is a significant obstacle to understanding the evolution of the nuclear activity since the star formation and AGN fueling may occur at different stages and with varying rates for each. Many of the signatures of star formation or black

hole activity (e.g. X-ray, radio or optical emission lines) can be indicative that starbursts or AGN are present but provide little quantitative assessment of their relative contributions or importance (a summary of the various SFR indicators is provided in Murphy et al., 2011).

In this paper we develop the theoretical basis for using the submm recombination lines of H, He, and He$^+$ to probe star formation and AGN. We find that the emissivities of these lines can provide reliable estimates of the EUV luminosities from 13.6 eV to $\sim 10^2$ eV and hence the relative luminosities associated with star formation (EUV near the Lyman limit) and AGN accretion (harder EUV).

Although the extremely high infrared luminosities of ULIRGs like Arp 220 and Mrk231 are believed to be powered by starburst and AGN activity, the distribution of star formation and the relative contributions of AGN accretion is very poorly constrained. This is due to inadequate angular resolution in the infrared and the enormous and spatially variable extinctions in the visible ($A_V \sim 500 - 2000$ mag). The submm lines will have minimal dust extinction attenuation. And, given the large number of recombination lines across the submm band, lines of the different species may be found which are close in wavelength and provide the capability to move to longer wavelengths to further reduce the dust opacity (in the most opaque sources). Although mid-IR fine structure transitions of heavy ions have been used in some heavily obscured galaxies, the line ratios depend on density, temperature and metallicity; in contrast, the H and He$^+$ lines have none of these complications. Lastly, we find that the expected fluxes in the lines are quite readily detectable with ALMA.

In the following, we first derive the emissivities and line opacities for the submm recombination lines as a function of density and temperature (Section 2.2). Then using simplified models for the ionizing continuum associated with OB stars and with AGN, we derive the relative emission measures of the H$^+$, He$^+$, and He^{++} regions for these two EUV radiation fields (Section 2.3). Lastly, we compare the expected line fluxes in HI and HeII with the sensitivity of ALMA and find that the lines should be readily detectable from ULIRG nuclei at low z. The observations of these lines can therefore provide the first truly quantitative assessment of the relative contributions of starbursts and AGN to the luminosity of individual objects.

2.2 Submm Recombination Lines

The low-n HI recombination lines at mm/submm wavelengths trace the emission-measure of the ionized gas and hence the Lyman continuum production rate associated with high mass stars and AGN. In contrast to the m/cm-wave radio HI recombination lines which can have substantial maser amplification (Brown et al., 1978; Gordon & Walmsley, 1990; Puxley et al., 1997), the submm recombination emission is predominantly spontaneous emission with relatively little stimulated emission and associated non-linear amplification (see Section 2.2.4). Since the submm HI lines (and the free-free continuum) are also optically thin, their line fluxes are a linear tracer of the ionized gas emission measure ($EM = \int n_e n_p d^3 r$). Therefore these lines are an excellent probe of the EUV luminosity of OB stars and AGN (assuming the EUV photons are not appreciably absorbed by dust). Lastly, we note that in virtually all sources, the dust extinction of the recombination lines at $\lambda \sim 350 \mu$m to 1mm will be insignificant.

Early observations of the mm-wave recombination lines were made in Galactic compact HII regions – in these regions the continuum is entirely free-free and hence one expects fairly constant line-to-continuum flux ratio if the mm-line emission arises from spontaneous decay in high density gas with little stimulated emission contribution. This is indeed the case – Gordon & Walmsley (1990) observed the H40α line at 99 GHz in 7 HII regions and found a mean ratio for the integrated-line brightness (in K km s^{-1}) to continuum of 31.6 (K km s^{-1}/K). Less than 3% variation in the ratio is seen across the sample. The optically thin free-free emission provides a linear probe of the HII region emission measure (EM) and hence the OB star Lyman continuum production rate. The observed constancy of the line-to-continuum ratios then strongly supports the assertion that the integrated recombination line fluxes are also a linear probe of the Lyman continuum production rates.

2.2.1 HII Line Emissivities

To calculate the expected HI line emission we make use of standard recombination line analysis (as described in Osterbrock & Ferland, 2006). The volume emissivity, ϵ is then given by

$$\begin{aligned}
\epsilon &= n_u A_{ul} h\nu \\
&= b_{n_u} n_u(TE) A_{ul} h\nu,
\end{aligned} \tag{2.1}$$
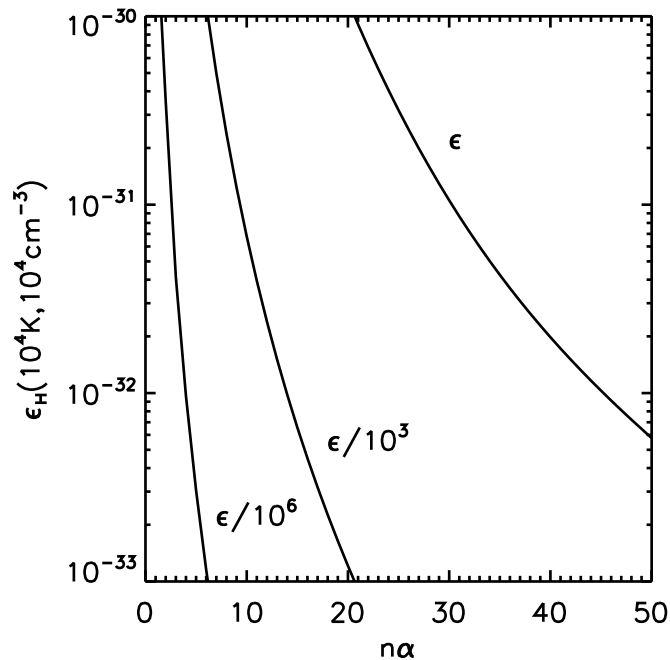
Figure 2.1: The emissivities of the HI α recombination lines are shown for $T = 10^4$ K. The emissivity is given per unit emission measure and has dimension $\mathrm{erg\,cm^{-3}\,s^{-1}}$ and the x-axis has the lower quantum number of the Hα transitions. The emissivities were calculated for $n_e = 10, 1000$, and 10^4 cm^{-3}; and the curves for all densities are coincident.

where n_u and $n_u(TE)$ are the actual and thermal equilibrium upper-level population densities. The exact HI spontaneous decay rates from levels u to l, A_{ul}, are available in tabular form online from Kholupenko et al. (2005). The most complete and up to date departure coefficients (from TE)(b_n and $d(\ln b_n)/dn$ are from Hummer & Storey (1987); Storey & Hummer (1995a,b). The latter work includes population transfer by electron and ion collisions and has emissivities for HI and HeII up to principal quantum number $n = 50$. They also calculate optical depth parameters for a wide range of electron temperature (T_e) and electron density (n_e). We make use of these numerical results in this paper; Figure 2.1 shows the Storey & Hummer (1995b) HI recombination line emissivities at $T = 10^4$K.

Figure 2.2 shows the submm HI-nα line emissivities ϵ per unit emission measure, for $T = 7500$ and 10^4 K. These volume emissivities were computed for density $n = 10^2$ and 10^4 cm^{-3} but the separate density curves are essentially identical. This is because, for these low energy levels, the spontaneous decay rates are very high ($A_{\Delta n=1}(HI) > 200$ s^{-1} for n < 30). The level populations are therefore determined mainly by the radiative cascade following recombi-
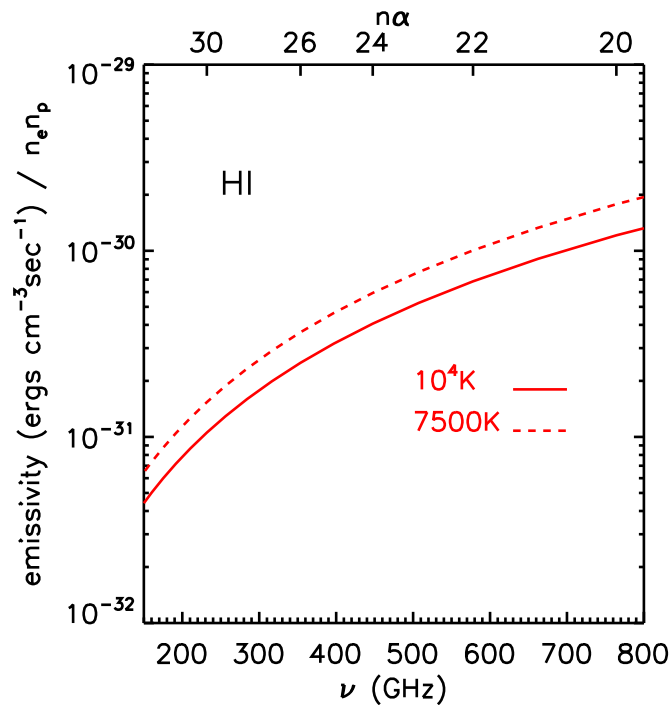
Figure 2.2: The emissivities of the HI submm recombination lines are shown for $T = 7500$ and 10^4 K. The emissivity is given per unit $n_e n_p$. The top border has the quantum number of the α transitions and their rest frequencies are on the bottom axis. The emissivities were calculated for $n_e = 10$, 1000, and 10^4 cm^{-3}; and the curves for all densities are coincident.

nation to high levels. The latter is proportional to the recombination rate and hence $n_e n_p$.

To translate the curves in Figure 2.2 into expected emission line luminosities, one needs to multiply by the total emission measure of each source. Consider the detectability of a luminous star forming region in a nearby galaxy. In Section 2.3 we show that for a starburst type EUV spectrum with integrated luminosity in the ionizing continuum at $\lambda < 912$Å, $L_{EUV} = 10^{12} \, L_\odot$, the total Lyman continuum photon production rate is $Q_{LyC} = 1.20 \times 10^{56}$ s^{-1}. Scaling this down to the luminosity of an OB star cluster with $L_{EUV} = 10^6$ $L_\odot$ gives $Q_{LyC} = 1.20 \times 10^{50}$s^{-1}. For Case B recombination in which all the ionizing photons are absorbed (i.e the HII is ionization bounded) and the $n \geq 2$ photons escape. (In fact, most of the Lyα may be absorbed by any residual dust.) In this case, the standard Strömgren condition equating the supply of fresh Lyman continuum photons (Q_{LyC}) to the volume integrated rate of

recombination to states above the ground state,

$$Q_{LyC} = \alpha_B n_e n_p \text{vol}, \tag{2.2}$$

implies an HII region emission measure (EM $= n_e n_p \text{vol}$) of EM $= 4.60 \times 10^{62}$ cm^{-3} (using $\alpha_B = 2.6 \times 10^{-13}$ cm^{3}s^{-1} at $T_e = 10^4$ K). Using the specific emissivity of 3×10^{-31} ergs cm^{-3} s^{-1} for HI-26α from Figure 2.2, the recombination line luminosity will be L$_{\text{H26}\alpha} = 1.38 \times 10^{32}$erg s^{-1}. For a source distance of 1 Mpc and a line width of 30 km s^{-1}, this corresponds to a peak line flux density of $\sim$ 3.3 mJy. This flux density is readily detectable at signal to noise ratio 10σ within $\sim$ 1 hr with ALMA Cycle 1 sensitivity.

2.2.2   He Line Emission

HeI has an ionization potential of 24.6 eV and its photoionization requirements are not very different than those of HI. Thus the HeI recombination lines probe the ionizing UV radiation field in much the same way as HI (see Section 2.3). Since the HeI submm lines will be weaker than those of HI due to the lower He abundance, we don't examine the HeI emission extensively here and instead focus on HeII.

The ionization potential of HeII is 54.4 eV corresponding to photons with $\lambda = 228$ Å for conversion of He$^+$ to He^{++}. Since the Wolf-Rayet / the most massive star in a starburst will have surface temperatures $\sim$ 50000 K, the ionizing EUV from such a population will have only a very small fraction of the photons with energy sufficient to produce He^{++}. Thus the recombination lines of HeII (He$^+$) which are produced by recombination of e + He^{++} can be a strong discriminant for the existence of an AGN with a relatively hard EUV-X-ray continuum. In starbursts there can be some HeII emission associated with Wolf-Rayet stars. However, the emission measure of the He^{++} region relative to that of the H$^+$ region will be much less than for an AGN.

The emissivities of the HeII recombination lines are taken from Storey & Hummer (1995a,b). For the interested reader, a simple model for the scaling of rate coefficients between Hydrogen and hydrogenic ions is developed analytically in Appendix 2.7 and those relations are compared with the numerical results from Storey & Hummer (1995b) in Appendix 2.8.

The HeII submm α lines near a given fixed frequency are at higher quantum numbers n than those of HI since the energy levels scale as the nuclear charge Z^2, i.e., a factor of 4 larger for the same principal quantum number n in He$^+$.
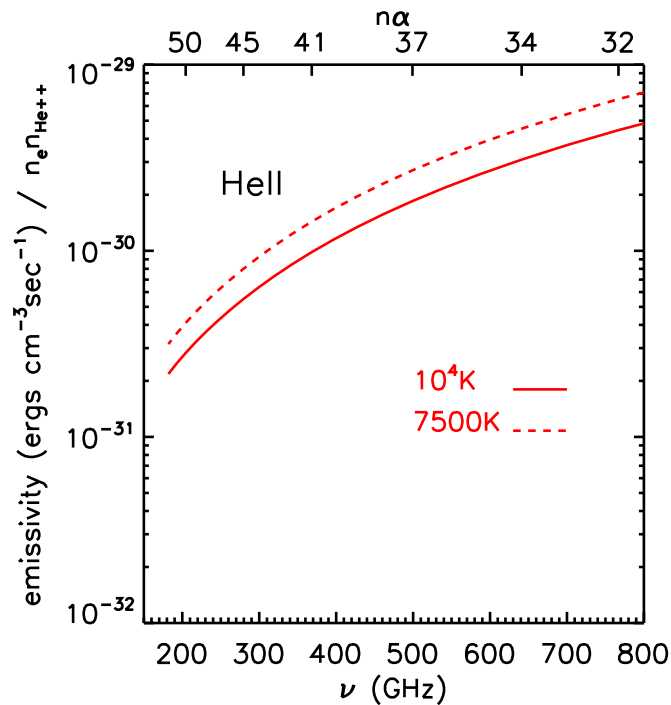
Figure 2.3: The emissivities of the HeII submm recombination lines are shown for T = 7500 and 10^4 K. For HeII it is per unit $n_e n_{He^{++}}$. The top border has the quantum number of the α transitions and their rest frequencies are on the bottom axis. The emissivities were calculated for n_e = 10, 1000, and 10^4 cm^{-3}; and the curves for all densities are coincident. Note that the emissivities for HeII per unit $n_e n_{He^{++}}$ are 4-5 times greater than those for HI at similar frequency – this partially compensates for the lower He abundance relative to H if their ionized volumes are similar (as would be the case for a very hard ionizing continuum).

For the submm HeII transitions, n = 30 - 50, versus 20 - 35 for HI. In Figure 2.3 the expected HeII line emissivities per unit $n_e n_{He^{++}}$ are shown for the submm band. The values of these emissivities are $\sim$ 5 times those of HI (Figure 2.1; however, since the He/H abundance ratio is 0.1 the actual values per unit $n_e n_p$ are quite similar in a plasma where all the H is ionized and all the He is He^{++}.

2.2.3 HeII/HI Emission Line Ratios with T_e and n_e

In Figure 2.4 the ratios of HeII/HI α recombination line emissivities (Storey & Hummer, 1995a) are shown as a function of principal quantum number for large ranges of both T_e and n_e. Note two cautions in viewing these plots: 1) as noted above the lines of HI and HeII are not at the same frequency for each n and 2) the emissivity ratios are per $n_e\, n_{He^{++}}$ and per $n_e\, n_p$ for HeII and HI, respectively. In the case of the latter, the EM for He++ will be almost always
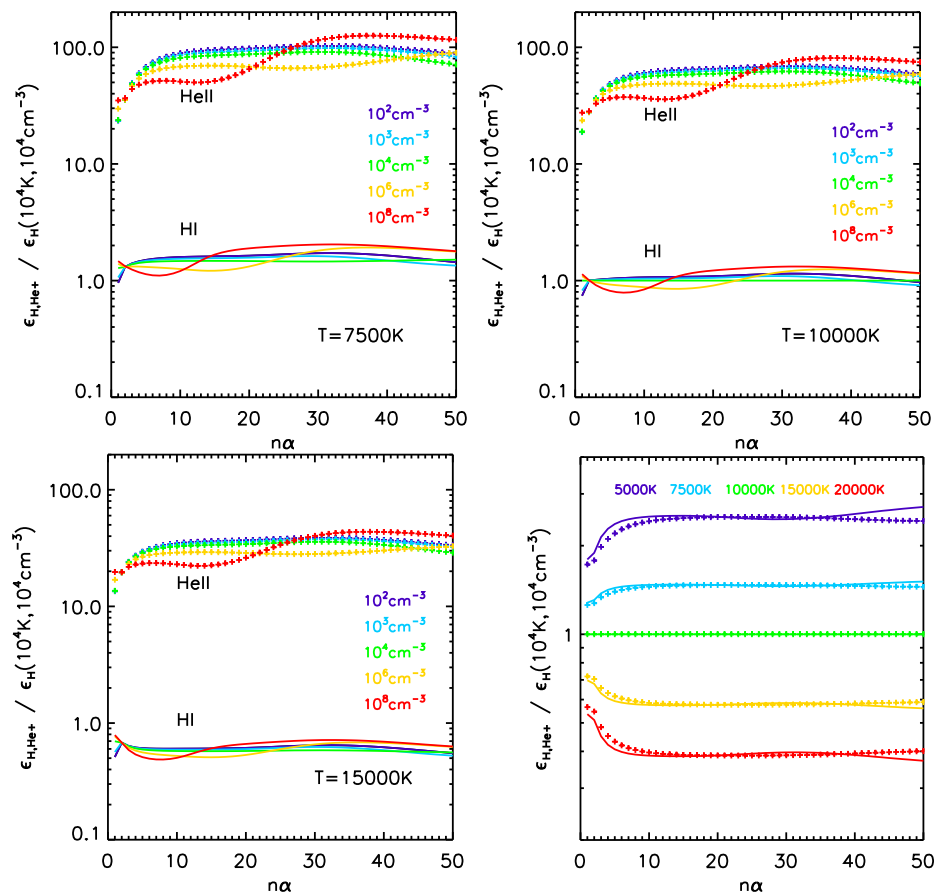
Figure 2.4: The emissitvity ratios of HeII to HI in the unit of their subsequent emission measure are shown as a function of principal quantum number n for $n_e = 10^2 - 10^8$ and T_e =7500, 10000, and 15000 K. [The emissivities are normalized to HI at 10^4 K and density 10^4 cm^{-3} so one can see the dependence on ion, temperature and density. The line ratios are very nearly independent of density for all the temperatures but they do depend on temperature as $T_e^{-4/3}$ for quantum number n ~ 10 to 50. The latter is clearly shown in the lower-right panel where the emissivity ratio is shown for 5 temperatures at $n_e = 10^4$ cm^{-3}.

< 0.1 of that for H+ due to the lower cosmic abundance of He.

Figures 2.4-top and lower-left clearly show that at a given temperature, T_e, the HeII/HI line ratio is virtually constant as a function of both quantum number and electron density. Thus, varying density in the ionize gas should have almost no influence on the line ratios of HeII to HI. On the other hand, it is clear from these figures that increasing T_e leads to a decrease in the HeII/HI emissivity ratio. In Figure 2.4-lower-right, the ratio is shown for a single density $n_e = 10^4$ cm^{-3} but $T_e = 5000$ to 20,000 K and the temperature dependence is clear and the same for all n transitions. Thus, the temperature and density dependence of the HeII to HI line ratios at fixed nα can be empirically fit by:

$$\frac{\epsilon_{\text{HeII}-n\alpha}}{\epsilon_{\text{HI}-n\alpha}} \quad \propto \quad n_e^0 \, T_e^{-4/3}. \tag{2.3}$$

Although the HeII/HI line ratios are temperature dependent, the actual range of temperatures expected for the ionized gas is very limited, $T_e = 7500 - 10000$ K in star forming HII regions due to the strong thermostating of the cooling function which decreases strongly at lower temperatures and increases steeply at higher temperatures (see Osterbrock & Ferland, 2006). For the AGN sources, it is also unlikely that the temperatures will be much higher since most of the heating is still provided by LyC photons near the Lyman limit (even though there are harder photons in their EUV spectra).

In Appendix 2.7, we show that the recombination rates coefficients scale as

$$\alpha_{\text{He}^+}(T_e) = Z\alpha_H(T_e/Z^2) \text{ with } Z \ = \ 2 \text{ for He}^+. \tag{2.4}$$

However, the line emission rates also depend on the radiative and collisional cascade through the high n levels and it is not possible to derive the emissivity scaling analytically to better than a factor of 2 accuracy.

2.2.4 Maser Amplification?

As noted above, it is well known that the m/cm-wave recombination lines ($n > 100$) of HI have substantial negative optical depths and hence maser amplification of the line emission. In such instances, the recombination line intensity will not accurately reflect the ionized gas emission measure and the associated Lyman continuum emission rates of the stellar population. For the submm HI and HeII lines we can analyze the possibility of maser amplifica-
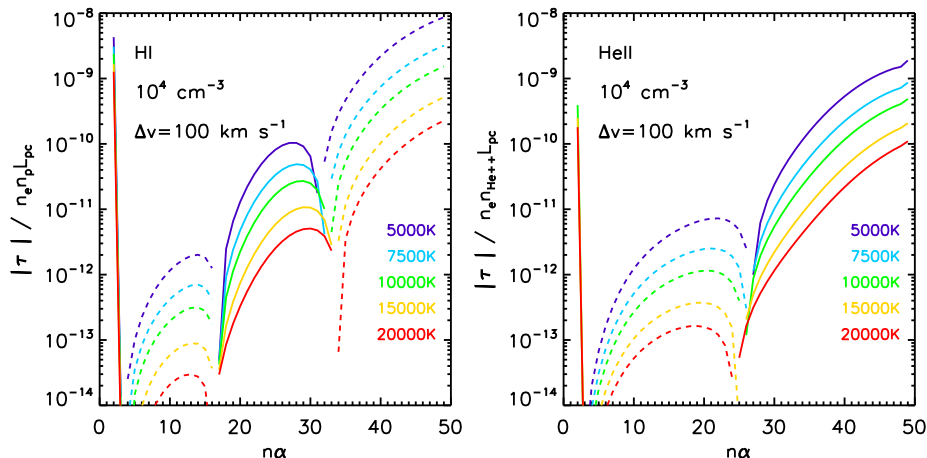
Figure 2.5: The specific optical depths of the HI and HeII recombination lines are shown with level populations calculated for $T = 5000$ to 20,000 K and density $n_e = 10^4$ cm^{-3}. A fiducial line width of 100 km s^{-1} was adopted. The specific optical depth is per unit $n_e n_p L_{pc}$, where L_{pc} is the line of sight length, and the lines are dashed where the optical depth is negative, implying a population inversion and possible maser amplification. A likely maximum line-of-sight emission measure is $\int n_e n_p dl \sim 10^9$ cm^{-6} pc, corresponding to a ULIRG starburst nucleus.
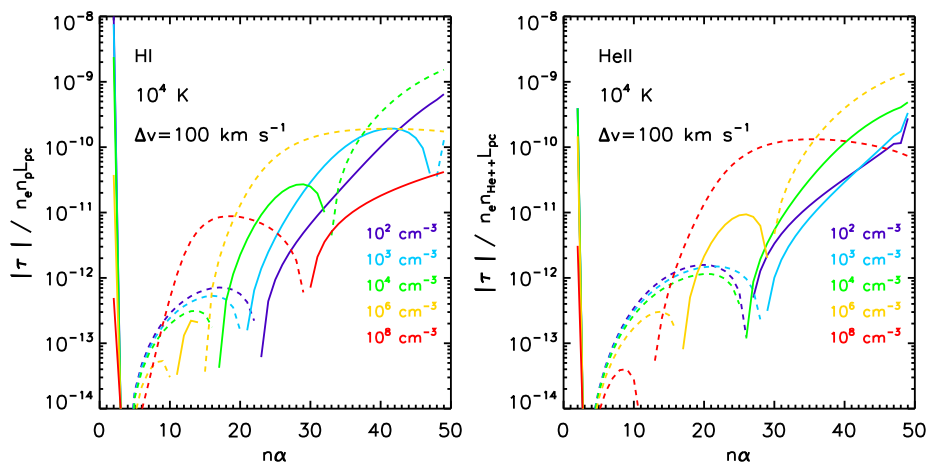
Figure 2.6: The specific optical depths of the HI and HeII recombination lines are shown with level populations calculated for $T = 10^4$ K and densities ranging between $n_e = 10^2$ and 10^8 cm^{-3}. A fiducial line width of 100 km s^{-1} was adopted. The specific optical depth is per unit $n_e n_p L_{pc}$ and the lines are dashed where the optical depth is negative, implying a population inversion and possible maser amplification. A likely maximum line-of-sight emission measure is $\int n_e n_p dl \sim 10^9$ cm^{-6} pc, corresponding to a ULIRG starburst nucleus.

tion using the optical depth information of Storey & Hummer (1995a). They provide an optical depth parameter $\Omega_{n,n'}$ which is related to the line center optical depth $\tau_{n,n'}$ by

$$\tau_{n,n'} = n_e n_{\mathrm{ion}} \Omega_{n,n'} L, \qquad (2.5)$$

where L is the line-of-sight path length. $\Omega_{n,n'}$ is inversely proportional to the line width in Hz, $\Delta_{n,n'}$, and in their output they used a thermal doppler width, implying a velocity full width at half maximum intensity

$$\Delta v_{FWHM} \;=\; \left(\frac{8 \, \ln 2 \, kT_e}{m_{\mathrm{ion}}} \right)^{1/2} \qquad (2.6)$$

or $21.7 \mathrm{km\,s^{-1}}$ for HI at 10^4 K. In most situations relevant to the discussion here, the line widths will exceed the thermal width due to large scale bulk motions within the host galaxies. We have therefore rescaled the optical depths to $\Delta v_{FWHM} = 100$ km s^{-1}. We have also scaled the optical depth to a *specific* optical depth τ per unit $n_e n_{\mathrm{ion}} L_{pc}$ where L_{pc} is the path length in parsecs and the volume densities in cm^{-3}.

Figures 2.5 and 2.6 show the *specific* optical depths for the HI and HeII lines as a function of T_e and n_e. The actual optical depths for a particular source may be obtained by scaling these curves by the factor $n_e n_p L_{pc}/\Delta v_{100}$. In these plots, the dashed lines are for transitions with a population inversion and hence negative optical depth.

The submm transitions of HI and HeII are principal quantum number $n \sim 20$ to 32 and 32 to 50, respectively. For both HI and HeII these particular transitions have positive specific optical depths and hence no maser amplification at virtually all densities and temperatures shown in Figures 2.5 and 2.6. The exceptions to this are that at very high densities, $n_e > 10^6$ cm^{-3}, there can be population inversions (see Figure 2.6). However, even at these high densities, significant amplification would occur only if the scale factor is sufficiently large.

An extreme upper limit for the HII in a ULIRG starburst nucleus might be $n_e n_p L_{pc} \sim 10^4 \times 10^4 \times 10 = 10^9$ cm^{-6} pc and $n_e n_{\mathrm{He^{++}}} L_{pc} \sim 10^8$ cm^{-6} pc for HeII. Applying the first scale factor to the curves shown in Figure 2.6 yields

upper limits to the negative optical depth $|\tau| < 0.1$, implying insignificant amplification even for these extreme conditions.

In summary, the observed emission line fluxes for the submm recombination lines will provide a linear probe of the HII and HeIII EMs; they will not be affected by non-linear radiative transfer effects, either maser amplification or optically thick saturation of the emission.

As an aside, it is interesting to note that the behavior of the HI opacities shown in Figure 2.5-left is reflected in the HeII opacities (Figure 2.5-left) but translated to higher nα transitions. This is of course expected since HeII is hydrogenic and the energy levels are scaled by a factor 4, implying higher principal quantum number in HeII to obtain similar line frequencies and A coefficients.

2.2.5 Excitation by Continuum Radiation in Lines?

Lastly, we consider the possibility that absorption and stimulated emission could alter the bound level populations away from those of a radiative cascade following recombination. Wadiak et al. (1983) analyzed this effect on the cm-wave recombination lines in powerful, radio-bright QSOs. For the submm lines considered here, the radiative excitation would be provided by the infrared continuum. Significant coupling of the level populations to the local radiation field at the line frequencies occurs when the net radiative excitation rate (i.e., absorption minus stimulated emission) is comparable with the spontaneous decay rate. It is easily shown that this happens when the local energy density of the radiation field exceeds that of a black body with temperature greater than T_x, where T_x is the excitation temperature characterizing the cascade level populations. (This is the radiative equivalent of the critical density often used to characterize the collisional coupling of levels to the gas kinetic temperature.) Neglecting departures from thermal equilibrium and letting $T_x \sim 10^4$ K, the effective radiation temperature T_R must be therefore be $> 10^4$ K at the submm line frequencies.

This scenario is probably only of conceivable relevance for an AGN and not for a starburst. For example, suppose the AGN luminosity is $\sim 10^{12}$ $L_\odot$, then the effective black body radius for 10^4 K is 0.007 pc. Inside this radius the radiation energy density will exceed that of a 10^4 K black body, but at larger radius the induced radiative transitions become much less important. For the ionization case of an AGN as discussed below (Section 2.3), the radii
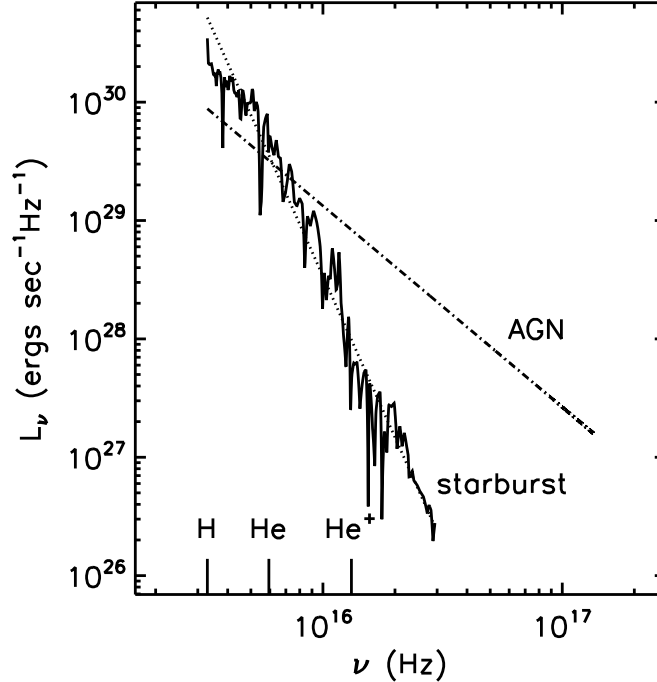
Figure 2.7: The input ionizing continua are shown for starburst and AGN sources. The starburst EUV down to $\lambda = 90$Å was computed from Starburst99 with a Kroupa IMF, solar metallicity and a constant SFR. The AGN EUV continuum was taken as a power-law with specific luminosity index $\nu^{-1.7}$. Both EUV spectra were normalized so that the integrated EUV luminosity (at $\lambda <$ 912 Å) was $10^{12}L_\odot$. The ionization thresholds for H, He, and He$^+$ are shown as vertical lines on the bottom axis. The dotted line along the SB spectrum is a power-law fit to the Starburst99 spectrum with $L_\nu \propto \nu^{-4.5}$ used for the analytic treatment in section 2.3.1.

of the HeIII and HII regions are 16 and 27 pc respectively, as shown in Figure 2.9. For this very simplified example, we do not therefore expect radiative excitation in the bound-bound transitions to be significant in the bulk of the ionized gas. For other instances, one can easily perform a similar analysis as a check.

2.3 Ionization Structure of Starbursts and AGN Sources

To evaluate the expected line luminosities for the HI and HeII lines, we now calculate the ionized gas emission measures for the typical EUV spectra associated with starbursts and AGN. With the derived EMs for H$^+$ and He^{++} as scale factors for HI and HeII emissivities per unit EM (Section 2.2.2 and 2.2.1), one can then calculate the line luminosities.

For the starburst (SB) spectrum, we adopt a Kroupa IMF (0.1 to 100 M$_\odot$)

and use the Starburst99 spectral synthesis program (Leitherer et al., 1999) to calculate the EUV spectrum at solar metallicity for a continuous SFR. For starburst durations longer than 10 Myr, the EUV at $\lambda < 912$ Å saturates at a duration-independent value since the early type star population has reached a steady state with equal numbers of new massive stars being created to replace those evolving off the main sequence. This EUV continuum can then be taken to represent a steady state SFR – applicable to starbursts lasting more the 10^7 yrs. For the AGN EUV-X-ray continuum, we adopt a simple power-law $L_\nu \propto \nu^{-1.7}$ (e.g. Osterbrock & Ferland, 2006). We scale both the SB and AGN L_ν to have integrated EUV luminosity = 10^{12} $L_\odot$ at $\lambda < 912$Å. For the starburst spectrum, this EUV luminosity corresponds to a steady-state SFR = 874 $M_\odot yr^{-1}$ for a Kroupa IMF. These two ionization spectra are shown in Figure 2.7. The figure clearly demonstrates the significant difference between the SB and AGN EUV spectra, with the former having almost no photons capable of ionizing He^+ to He^{++}, compared to the number of HI ionizing photons.

Using these EUV continua, we have computed the ionization structure for a cloud with H density $n = 10^4$ cm^{-3}, assuming all EUV photons are used for ionization, i.e., the plasma is ionization bounded and no EUV is absorbed by dust within the ionized gas. The He/H abundance ratio was 0.1. The EUV continuum was assumed to originate in a central point source and the specific luminosity of the ionizing photons at each radius was attenuated by the optical depth at each frequency due to H, He, and He^+ along the line of sight to the central source. The secondary ionizing photons produced by recombinations with sufficient energy to ionize H or He were treated in the "on the spot" approximation, i.e., assumed to be absorbed at the radius they were produced. Lastly, we simplified the analysis of these secondary photons by assuming a fraction 0.96 and 0.66 of the He^+ recombinations yielded a photon which ionizes HI at electron densities below and above 4000 cm^{-3} (see Osterbrock & Ferland, 2006), respectively.

Figures 2.8 and 2.9 show the relative sizes of the HII, HeII, and HeIII regions for the SB and AGN. These figures clearly show the marked contrast in size (and hence EM) of the He^{++} regions in the two instances. Much less contrast is seen in the He^+ emission measures between the two models. The HeIII region is much smaller relative to the HII region for the starburst, while in the AGN with more highly ionizing photons, the difference is size is more modest.

From ionization equilibrium calculations for the SB and AGN EUV spectra,
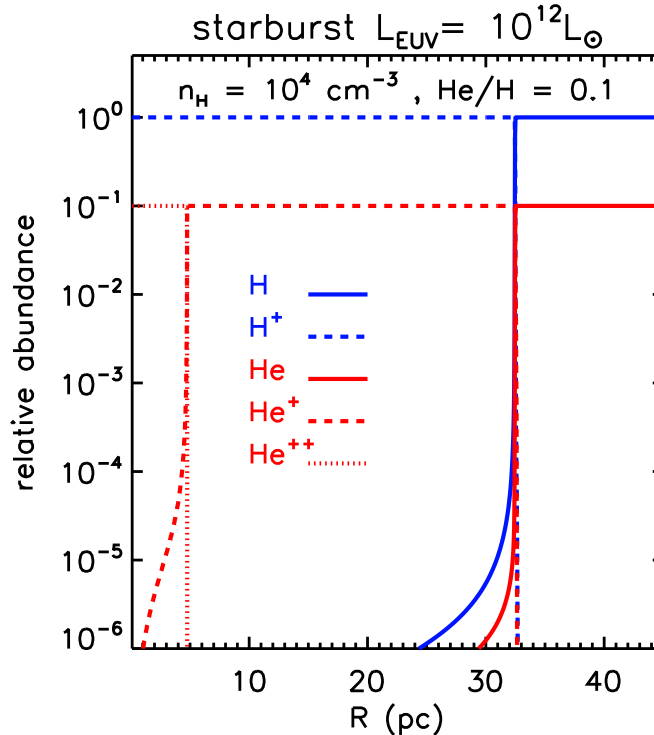
Figure 2.8: For a starburst EUV spectrum with $L_{EUV} = 10^{12}$ $L_\odot$ and Hydrogen density $n = 10^4$ cm^{-3}, the radii of the H$^+$, He$^+$, and He^{++} regions are shown. The He/H abundance ratio was 0.1.

we derive the EM of the ionized regions in HII, HeII, and HeIII (Table 2.1). For both ionizing sources the spectra were normalized to have $L_{EUV} = 10^{12}$ $L_\odot$. From the EMs shown in Table 2.1, we draw two important conclusions: 1) despite the very different spectral shapes, the bulk of the ionizing continuum is absorbed in the HII region and the EM$_{H^+}$ provides a reasonably accurate estimate of the total EUV luminosity, differing less than a factor 2 between the two cases, and 2) the EM ratio, EM$_{He^{++}}$/EM$_{H^+}$, is 50 times greater for the AGN than for the SB, indicating that this ratio provides an excellent diagnostic of AGN versus SB ionizing sources.

2.3.1 Ionization Structure – Analytics

In the previous section, we made use of a full ionization equilibrium model using Starburst99 for the starburst EUV spectrum and a power law approximation for the AGN EUV. In this numerical treatment, we track the competition of all three species (HI, HeI, and HeII) for ionizing photons at each wavelength. However, an analytic treatment, which turns out to reproduce quite well the full numerical approach, can be developed using a few simplifying assumptions
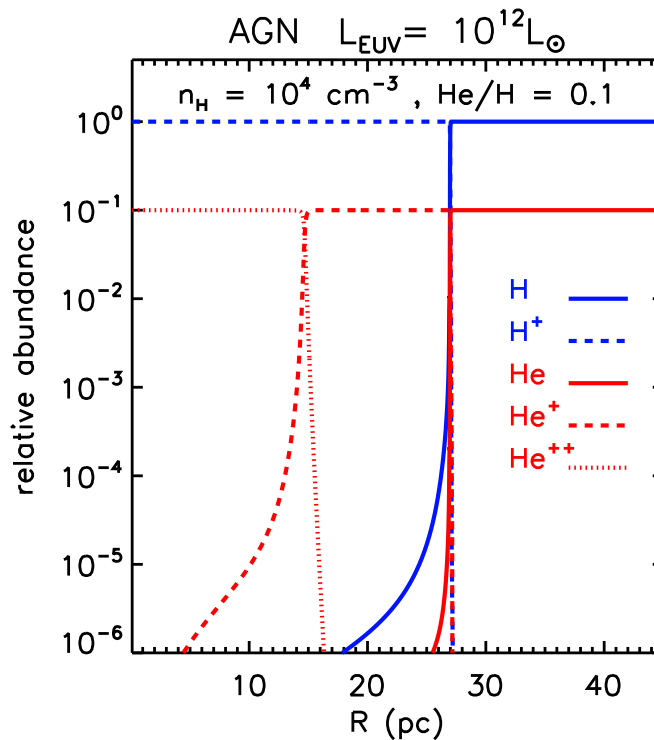
Figure 2.9: For an AGN power-law EUV-X-ray spectrum with $L_{EUV} = 10^{12}$ $L_\odot$ and Hydrogen density $n = 10^4$ cm^{-3}, the radii of the HII, HeII, and HeIII regions are shown. The He/H abundance ratio was 0.1.

Emission Measures of Ionized Regions

EUV	L_{EUV}	SFR/$\dot{M}_{acc}$	Q_{Lyc}	$n_e n_p$vol	$n_e n_{He^+}$vol	$n_e n_{He}^{++}$vol	$L_{H26\alpha}$/$L_{HeII-42\alpha}$
	$L_\odot$	$M_\odot$/yr	s^{-1}	cm^{-3}	cm^{-3}		
Starburst	10^{12}	674	1.20×10^{56}	4.61×10^{68}	4.59×10^{67}	1.59×10^{65}	0.0017
AGN	10^{12}	0.65	6.97×10^{55}	2.68×10^{68}	2.21×10^{67}	4.64×10^{66}	0.084

Table 2.1: L$_\nu$ for the SB and AGN were normalized to both have 10^{12} $L_\odot$ in the Lyman continuum at $\lambda < 912$ Å(Column 2). Based on comparing Figures 2.2 and 2.3, the HeII-42α line has 4.82 times larger flux per unit EM than the H26α line; this factor is used to estimate the line luminosity ratio given in column 8. Line ratio is for $T = 10^4$K. The emission measures (EM) are given in cm^{-3}. Here SFR/$\dot{M}_{acc}$ stands for SFR or AGN accretion rate required to give this L_{EUV}. The SFR assumes a Kroupa IMF; it would be factor 1.6 higher for a Salpeter IMF. The AGN accretion rate assumes 10% of the mass accretion rate is converted to EUV luminosity. Note that H26α and HeII-42α are at 353.623 and 342.894 GHz respectively, separated by 10.7 GHz and therefore observable in a single tuning with ALMA Band 7.

regarding the EUV spectra and the competition between the 3 species for the ionizing photons in the energy regimes above 24.6 ev.

At photon energies between 24.6 to 54.4 eV, both HI and HeI can be ionized, and at energies above 54.4 eV all three species (HI, HeI, and HeII) can be ionized. However, for all three species, the ionization cross sections are highest at the thresholds and drop as ν^{-3} above their respective thresholds. At 24.6 eV (the HeI ionization threshold), the HeI ionization cross section is 8 times larger than that of HI at the same energy. Thus, provided HI is mostly ionized, the photons above this energy are largely used to ionize HeI. These two factors (the higher cross section and the fact that HI is mostly ionized) more than make up for the fact that the He/H abundance ratio is 0.1 (see Figures 2.8 and 2.9). A fraction of the HeI recombination photons can ionize HI so effectively that each of the photons above 24.6 eV will ionize both HeI and HI. This fraction varies between 0.96 (for $n_e < 4000$ cm^{-3}) and 0.66 (for $n_e > 4000$ cm^{-3}) (see Osterbrock & Ferland, 2006). Thus, one can approximate the number of photons available to ionize HI as all those above 13.6 eV. Above 54.4 eV, the photons are predominantly used for HeII ionization since the abundance of HI will be very low in the HeII region. (This last assumption presumes that the ionizing continuum is hard enough that the gas is easily ionized to HeII.)

In comparing the ionization associated with a SB versus an AGN, we assume that the ionized regions are ionization bounded and that dust within the ionized regions does not significantly deplete the EUV. The latter could be a significant issue for very young ionized regions but is perhaps less likely for SB and AGN ionized regions where the timescales are $> 10^7$ yrs and the dust within the ionized gas is likely to have been destroyed. Under these assumptions, the standard Strömgren relation implies that the total volume integrated emission measure of each species ionized region will be determined by the total production rate of fresh ionizing photons. For comparing the SB and AGN cases, we normalize both EUV spectra to have the same total integrated EUV luminosity,

$$L = \int_{\nu_{th}}^{\infty} L_\nu d\nu, \tag{2.7}$$

where ν_{th} is the ionization threshold frequency. The production rate of ionizing photons is then given by Q, with

$$Q = \int_{\nu_{th}}^{\infty} L/h\nu \ d\nu. \tag{2.8}$$

We consider the three regimes in the EUV

1. $h\nu \geq 13.6$ eV and $h\nu_{th} = h\nu_0 = 13.6$ eV

2. $h\nu \geq 24.6$ eV and $h\nu_{th} = h\nu_1 = 24.6$ eV

3. $h\nu \geq 54.4$ eV and $h\nu_{th} = h\nu_2 = 54.4$ eV

corresponding to H ionization, He to He^+ ionization, and He^+ to He^{++} ionization.

For the EUV spectra we make the assumption that *both* SB and AGN EUV spectra can be represented by power-laws with $L_\nu = C_{SB}\nu^{-\alpha_{SB}}$ and $C_{AGN}\nu^{-\alpha_{AGN}}$. For the AGN, this is a commonly used assumption with $\alpha_{AGN} = 1.7$. For the SB this assumption may appear surprising but Figure 2.7 clearly shows that the EUV spectrum obtained from the spectral synthesis of a continuous SB can be fit by a power-law with $\alpha_{SB} = 4.5$. For these simple power-laws, the luminosity normalization yields the relation

$$\frac{C_{AGN}}{C_{SB}} = \frac{(1 - \alpha_{AGN})}{(1 - \alpha_{SB})}\nu_0^{-\alpha_{SB}+\alpha_{AGN}} \tag{2.9}$$

and for $\alpha_{AGN} = 1.7$ and $\alpha_{SB} = 4.5$, this reduces to $C_{AGN}/C_{SB} = 5\nu_0^{2.8}$.

The Strömgen ionization equilibrium for a power-law ionizing spectrum then yields

$$\frac{Q_{He^{++}}}{Q_{H^+}} = \left(\frac{\nu_2}{\nu_0}\right)^{-\alpha} = 4^{-\alpha} \tag{2.10}$$

since $\nu_2 = 4\nu_0$. For the AGN with $\alpha_{AGN} = 1.7$, $Q_{He^{++}}/Q_{H^+} = 0.095$ and for the SB, $\alpha_{SB} = 4.5$, $Q_{He^{++}}/Q_{H^+} = 1.95 \times 10^{-3}$.

For Case B recombination, the Qs are related to the emission measures of their respective Strömgren spheres by the recombination coefficients to states above the ground state and the electron density

$$\begin{aligned} Q_{H^+} &= n_e n_p \ \alpha_b(H) \ \text{vol} \\ &\simeq 2.60 \times 10^{-13} n^2 \ (T/10^4)^{1/2} \ \text{vol} \end{aligned} \tag{2.11}$$

and

$$
\begin{aligned}
Q_{\mathrm{He^{++}}} &= n_e n_{\mathrm{He^{++}}} \, \alpha_b(He^+) \text{ vol} \\
&\simeq 1.85 \times 10^{-12} n n_{\mathrm{He^{++}}} \, (T/10^4)^{1/2} \text{ vol,}
\end{aligned} \tag{2.12}
$$

where n is the number density of H nuclei, **vol** is the volume of the ionized region and we set $n_e = 1.1 \times n_{\mathrm{H}}$ and $1.2 \times n_{\mathrm{H}}$ for the H^+ and He^{++} regions respectively.

For $T = 10^4$K and $[\mathrm{He/H}] = 0.1$, the emission measures are

$$
\begin{aligned}
EM_{\mathrm{H^+}} &= Q_{\mathrm{H^+}}/2.60 \times 10^{-13} \\
&= 3.85 \times 10^{12} Q_{\mathrm{H^+}}
\end{aligned} \tag{2.13}
$$

and

$$
\begin{aligned}
EM_{\mathrm{He^{++}}} &= Q_{\mathrm{He^{++}}}/1.85 \times 10^{-12} \\
&= 5.41 \times 10^{11} Q_{\mathrm{He^{++}}}.
\end{aligned} \tag{2.14}
$$

The emission measure ratio is therefore

$$
EM_{\mathrm{He^{++}}}/EM_{\mathrm{H^+}} = 0.141 Q_{\mathrm{He^{++}}}/Q_{\mathrm{H^+}}. \tag{2.15}
$$

Thus, $EM_{\mathrm{He^{++}}}/EM_{\mathrm{H^+}} = 1.34\times10^{-2}$ and 2.75×10^{-4} for the AGN and SB EUVs, respectively. From the results of the numerical calculation given in Table 2.1, the ratios were 1.73×10^{-2} and 3.45×10^{-4}, respectively. We therefore conclude that the simple analytic approach provides excellent agreement with the results quoted above for a full numerical ionization equilibrium calculation obtained using the detailed SB99 spectrum for the starburst.

Lastly, we note that the change in the AGN / SB ratio of EMs (He^{++}/H^+) is easily shown from Eq. 2.10 to be

$$
\frac{EM(\mathrm{He^{++}/H^+})_{\mathrm{AGN}}}{EM(\mathrm{He^{++}/H^+})_{\mathrm{SB}}} = 4^{-\alpha_{\mathrm{AGN}}+\alpha_{\mathrm{SB}}} = 48.5 \tag{2.16}
$$

as compared with 49.4 from the numerical analysis above. Contrasting this

HI and HeII Paired Submm Lines

HI $n\alpha$	ν GHz	HeII $n\alpha$	ν (GHz) GHz	$\Delta\nu$ (GHz) GHz	ϵ_{HI} erg s^{-1} cm^3	ϵ_{HeII} erg s^{-1} cm^3
20	764.230	32	766.940	-2.710	1.21×10^{-30}	4.45×10^{-30}
21	662.404	34	641.108	21.296	9.05×10^{-31}	3.09×10^{-30}
22	577.896	35	588.428	-10.531	6.85×10^{-31}	2.59×10^{-30}
23	507.175	37	499.191	7.985	5.25×10^{-31}	1.85×10^{-30}
24	447.540	38	461.286	-13.746	4.06×10^{-31}	1.57×10^{-30}
25	396.901	40	396.254	0.647	3.17×10^{-31}	1.15×10^{-30}
26	353.623	42	342.894	10.729	2.50×10^{-31}	8.47×10^{-31}
27	316.415	43	319.781	-3.366	1.99×10^{-31}	7.32×10^{-31}
28	284.251	45	279.432	4.818	1.60×10^{-31}	5.50×10^{-31}
29	256.302	46	261.787	-5.485	1.29×10^{-31}	4.79×10^{-31}
30	231.901	48	230.713	1.187	1.05×10^{-31}	3.67×10^{-31}
31	210.502	50	204.370	6.132	8.67×10^{-32}	2.83×10^{-31}
32	191.657	51	192.693	-1.036	7.18×10^{-32}	2.48×10^{-31}

Table 2.2: In ALMA Band 7 (275 to 365 GHz), the IF frequency is 4 GHz and the correlator has a nominal coverage of 4×2 GHz or 8 GHz in each sideband. Therefore a single tuning can cover ~16 GHz of bandwidth.

large change in the He^{++} between the SB and AGN EUVs, Table 2.1 shows only ~ 10% change in the ratio of He$^+$ relative to H$^+$ between the two cases, implying that the HeI recombination lines cannot be used to discriminate AGN and SB EUVs.

As an aside, we note that we were surprised to find that the SB99 EUV spectrum shown in Figure 2.7 could be fit by a power-law. Upon investigating this further, we found that there is enormous variation in the model EUV spectra depending on which stellar atmosphere model was employed, and due to the very uncertain contributions of Wolf-Rayet stars. Given these large uncertainties in the predicted SB EUV spectra, the specific power law index adopted above should only be taken as illustrative. Instead, it would be more appropriate to take the power-law as a "parameterization" which allows simple exploration of the EUV spectral properties and HI and HeII emission line ratios. In fact, measurements of the $EM(\text{He}^{++}/\text{H}^+)$ ratio might be used to constrain the very uncertain EUV spectra of SB regions and OB star clusters. An alternative parameterization might be to model the SB EUV as a blackbody. For $T_{BB} = 45,000$K, $Q_{\text{He}^{++}}/Q_{\text{H}^+} \simeq 2.8 \times 10^{-4}$, implying a similar ratio for the emission measures. This is effectively a factor 10 lower than the ratio

obtained for SB99 EUV and the $\alpha_{SB} = 4.5$ power-law used above.

2.4   Paired HI and HeII Recombination Lines

In Table 2.2 we provide a list of the submm HI recombination lines together with their closest frequency-matched HeII lines. The ALMA IF frequency is 4 GHz and each correlator has a maximum bandwidth of 1.8 GHz, thus in a single tuning the spectra can cover up to 16 GHz. One prime pairing for simultaneous coverage of HI and HeII occurs at 350 GHz where HI-26α and HeII-42α can be observed within a good atmospheric window (ALMA Band 7). In Table 2.1, the last column gives the expected line ratio, HeII-42α/HI-26α derived from the EM given in Table 2.2. The emissivities are shown in Figures 2.2 and 2.3. The line ratio varies by a factor 50 between the two cases, clearly demonstrating the efficacy of the HeII/HI submm line ratios to discriminate the nature of the ionizing sources. By contrast, the ratio EM_{H^+}/EM_{He^+} is different only by a factor 10% between the SB and AGN cases, indicating that the HeI/HI recombination line ratios are not a good SB versus AGN discriminant.

2.5   Star Formation Rates and AGN Luminosity

Derivation of SFRs and AGN accretion rates from the HI and HeII recombination lines are potentially quite straightforward provided the form of each EUV spectrum can be parameterized. For the preceding analysis we normalized the EUV luminosity to 10^{12} $L_\odot$ for both the SB and AGN. For a continuous SB (extending over $> 10^7$ yrs) the EUV luminosity will be constant. This EUV luminosity (10^{12} $L_\odot$) translates to the steady state SFR = 874 $M_\odot yr^{-1}$ for a Kroupa IMF. The implied SFR is a factor 1.6 higher for a Salpeter IMF. (The total stellar luminosity integrated over all wavelengths would be 5.5×10^{12} $L_\odot$ at 10^7 yrs.) For an AGN with $L_{EUV} = 10^{12}$ $L_\odot$, this EUV luminosity corresponds to an accretion rate of 0.65 $M_\odot yr^{-1}$ assuming 10% conversion of accreted mass to EUV photon energy. [Note that the above luminosities refer to that in the EUV, not the total bolometric luminosities.]

For galaxies with these luminosities, the submm recombination lines of both HI and HeII are detectable with ALMA out to distance $\sim$ 100 Mpc in a few hours integration. As an example, consider the H-26α line in a ULIRG like Arp 220 (or NGC 6240) at a distance $\sim$ 100 Mpc with an HII emission measure EM_{H^+} (see Table 2.1). For a specific emissivity ϵ, emission measure EM and source distance D (all in cgs units), the velocity-integrated line flux in observer

units Jy km s^{-1} is given by

$$S\Delta V = \frac{\epsilon \ EM_{\text{H}^+}}{4\pi D^2} \frac{c}{\nu_{\text{obs}}} 10^{18} \text{ Jy km s}^{-1}.$$

Using the volume emissivity of $\epsilon = 2.5 \times 10^{-31}$ ergs cm^{-3} s^{-1} / $n_e n_p$vol from Figure 2.1, one finds the velocity-integrated line flux for H-26α:

$$S_{\text{HI}-26\alpha}\Delta V \quad = \quad 7.17\frac{EM_{\text{H}^+}}{4 \times 10^{68}}D_{100\text{Mpc}}^{-2}\nu_{350\text{GHz}}^{-1} \quad \text{Jy km s}^{-1}. \qquad (2.17)$$

The frequency-paired HeII42α line will have an integrated flux $\sim 8\%$ of HI-26α in the case of AGN. Both lines should be simultaneously detectable in a few hours with ALMA. For reasonable densities, the emission in these lines will be directly proportional to the EM of the gas. Even at $n_e = 10^6$ cm^{-3}, the emission rate in the HI-26α and HeII42α lines are altered by only 1 and 2%, respectively. If the source is known to be a 'continuous' starburst, one may substitute SFR/(674 M$_\odot$yr^{-1}) for $EM_{\text{H}^+}/(4 \times 10^{68})$ in the equation above,

$$S_{\text{HI}-26\alpha}\Delta V \quad = \quad 1.06\frac{SFR}{100M_\odot \text{ yr}^{-1}}D_{100\text{Mpc}}^{-2}\nu_{350\text{GHz}}^{-1} \quad \text{Jy km s}^{-1}. \qquad (2.18)$$

We have recently detected the HI-26α in Arp 220 in ALMA Cycle0 observations with a line flux indicating a $SFR \simeq 100$ M$_\odot$yr^{-1} (Scoville et al., 2015). Yun et al. (2004) also report detection of HI-41α at 90 GHz yielding a similar SFR.

As noted earlier, the free-free (Bremsstrahlung) continuum emission can also be used to probe the ionized gas EM. For completeness, the free-free flux density in the submm regime is given by

$$S_{ff} = 75.0\frac{EM_{\text{H}^+}}{4 \times 10^{68}} \ \nu_{300\text{GHz}}^{-0.17} \ T_{10^4\text{K}}^{-0.5} \ D_{100\text{Mpc}}^{-2} \text{ mJy}, \qquad (2.19)$$

where we have included a factor 1.1 to account the the He$^+$ free-free emission assuming [He/H] $= 0.1$ and $\nu^{-0.17}$ is the frequency dependence of the Gaunt factor at submm wavelengths. In most instances the thermal dust emission

will dominate the free-free so the latter is not generally a useful tracer of the ionized gas EM.

2.5.1 Dust Extinction

We have stressed that a major advantage of the submm recombination lines is that they are at sufficiently long wavelengths that dust extinction should be negligible, since for standard dust properties the extinction should be $A(\lambda) \sim 10^{-4}(\lambda_{\mu m}/300\mu m)^{-1.8}A_V$ at submm and longer wavelengths (e.g. Battersby et al., 2011; Planck Collaboration et al., 2011a,b). Thus for $A_V < 1000$ mag, extinction at $\lambda > 300\mu m$ should be minimal. However, there are a few extreme cases such as Arp 220 and young protostellar objects which may have somewhat higher dust columns. In these cases, the recombination lines provide a unique probe of the dust extinction through measurements of HI lines at different submm wavelengths. Their intrinsic flux ratios can be determined from Figure 2.2; the extinction is then obtained by comparison of the intrinsic and observed line ratios. In sufficiently bright recombination line sources with high extinction, such observations could potentially be used to determine the frequency dependence of the dust extinction in the submm – this has been a major uncertainty in the analysis of submm continuum observations.

2.6 Conclusions

We have evaluated the expected submm wavelength line emission of HI, HeI, and HeII as probes of dust embedded star formation and AGN luminosity. We find that the low-n α transitions should provide a linear probe of the emission measures of the different ionized regions. Although their energy levels will have population inversions, the negative optical depths will be $\ll 0.1$ for the maximum gas columns expected and hence there is no significant maser amplification.

The submm HI and HeII lines have major advantages over other probes of SF and AGN activity: 1) the dust extinction should be minimal; 2) the emitting levels (n < 30 for HI and < 50 for HeII) have high critical densities ($n_{crit} >$ 10^4 cm^{-3}, Sejnowski & Hjellming, 1969) and hence will not be collisionally suppressed; 3) they arise from the most abundant species and therefore do not have metallicity dependences; and 4) they will not be little affected by masing. The emission line luminosities of the HI (and HeI) submm recombination lines are therefore a direct and linear probe of the EUV luminosity and hence SFR if the source is a starburst.

The emission ratios of HI to HeII can be a sensitive probe of the hardness of the EUV ionizing radiation field, providing a clear discriminant between AGN and SBs, and the test for evolution of the characteristics of EUV spectra of SBs at different redshifts.

The observed ratios of the submm HI recombination lines may also be used to determine the extinction in highly extincted luminous sources and to constrain the shape of the submm extinction curve.

Lastly, we find that these lines should be readily detectable for imaging with ALMA in luminous galaxies out to 100 Mpc and less luminous sources at lower redshift. We note that the far infrared fine structure lines observed with Herschel often show line deficits in the ULIRGs relative to the IR luminosity, possibly indicating either dust absorption of the EUV or collisional suppression of the emission rates at high density (Graciá-Carpio et al., 2011); the latter will not be a problem since the HI and HeII lines are permitted transitions with high spontaneous decay rates.

2.7   Appendix: Scaling Relations for Hydrogenic Ions

The aim of this appendix is to lay the basis of partial analytical explanation of HeII to HI emissivities scaling relation discussed previously. To this end, in this following sections of this Appendix, we analyze radiative processes involving Hydrogen-like atom consisting of Z charged nucleus and single electron orbiting it and put them in use in Appendix B. In this notations HI corresponds to $Z = 1$ and HeII to $Z = 2$.

Below we refer to Landau & Lifshitz (1977) and Berestetski et al. (1982), as examples of standard course in quantum mechanics and QED. The choice is dictated by our personal preferences. The reader is free to refer to any standard textbook in quantum mechanics and QED or original papers, references to which can be found in Landau & Lifshitz (1977) and Berestetski et al. (1982).

2.7.1 Radiation

Scaling of the Einstein A-coefficients for spontaneous radiative decay can be explicitly derived in the dipole approximation. The probability of dipole transitions between two states of the hydrogenic ion is given by

$$A_{n_1 \to n_2} = \frac{4(\omega_{n_1 \to n_2})^3}{3\hbar c^3} d^2_{n_1 \to n_2}, \tag{2.20}$$

where $w_{n_1 \to n_2} = Z^2 \frac{me^4}{2\hbar^3} \left(\frac{1}{n_2^2} - \frac{1}{n_1^2} \right) = Z^2 w^H_{n_1 \to n_2}$ is the frequency of radiated photon and $d^2_{n_1 \to n_2}$ is the average over l's and m's of the transition dipole moment $d_{n_1 l_1 m_1 \to n_2 l_2 m_2}$. Here

$$d^2_{n_1 \to n_2} = \frac{1}{n^2} \sum_{l_1, m_1, l_2, m_2} d^2_{n_1 l_1 m_1 \to n_2 l_2 m_2} \quad \text{and} \tag{2.21}$$

$$d^2_{n_1 l_1 m_1 \to n_2 l_2 m_2} = \langle d_x \rangle^2 + \langle d_y \rangle^2 + \langle d_z \rangle^2 \tag{2.22}$$

with $\langle d_i \rangle = -\langle \psi_{n_2 l_2 m_2} | e r_j | \psi_{n_1 l_1 m_1} \rangle$, $j = x, y, z$ and r_j is the component of electron radius vector in atom (we neglect the motion of nucleus). The wave functions $\psi_{in} = \psi_{n_1 l_1 m_1}$ and $\psi_f = \psi_{n_2 l_2 m_2}$ are the initial and final wave functions of the electron on $n_1 l_1 m_1$ and $n_2 l_2 m_2$ levels of hydrogenic ion.

One can show (see any standard course in quantum mechanics, for example, Landau & Lifshitz (1977)) that the transition dipole moment can be written as

$$\langle d_j \rangle = -\frac{a_0}{Z} \int_0^\infty \tilde{\psi}^\dagger_{n_2 l_2 m_2}(\tilde{\mathbf{r}}) e \tilde{r}_j \tilde{\psi}_{n_1 l_1 m_1}(\tilde{\mathbf{r}}) d^3 \tilde{r} = \frac{1}{Z} \langle d_j^H \rangle, \tag{2.23}$$

where $\tilde{r} = Zr/a_0$ is a dimensionless variable, $a_0 = \hbar^2/me^2$ is the Bohr radius and $\tilde{\psi}_{n_{ion} l_{ion} m_{ion}}$ are the wave functions of the electron in the Hydrogen-like atom written in terms of $\tilde{r}$. The integral is independent of Z. We observe that there is a simple scaling for the A-coefficients between hydrogenic Z ion and H

$$A_{n_1 \to n_2} = Z^4 \frac{4(\omega^H_{n_1 \to n_2})^3}{3\hbar c^3} (d^H_{n_1 \to n_2})^2 = Z^4 A^H_{n_1 \to n_2}. \tag{2.24}$$

2.7.2 Recombination Rate Coefficients

Recombination coefficients and recombination cross sections for a free electron with the hydrogenic nucleus in its exact form cannot be simply scaled from HI. However, for our application, the recombining electrons are non-relativistic and

we restrict our attention to this limit to obtain the scaling in the leading, dipole approximation. Assuming that the recombining electrons are non-relativistic implies that the energy of the emitted photon is much less than the electron mass[1] $\omega \ll m$. The recombination cross section can then be written as (see Berestetski et al. (1982) and references there in)

$$d\sigma_{\text{rec}} \simeq e^2 \frac{\omega m}{\pi p} |\mathbf{e} v_{if}|^2 d\Omega, \tag{2.25}$$

where p is the momentum of the incoming electron, ω is the energy of the outgoing photon, $\mathbf{e}$ is the photon polarization vector, $d\Omega$ is the angular measure and $\mathbf{v}_{if}$ is the transition element $\mathbf{v}_{if} = \int \psi_f^\dagger \mathbf{v} \psi_i d^3 x$ and $\mathbf{v} = -\frac{i}{m}\nabla$. Here ψ_i and ψ_f are the initial and the final wave functions of the electron.

The initial electron wave function is the continuous spectrum wave function in the attractive potential of the hydrogenic nucleus $V = -Ze^2/r$. For its explicit form see, for example, Landau & Lifshitz (1977). The final wave function of the electron is the discrete spectrum wave function in the attractive potential of the Z-ion nucleus, i.e., the electron wave function in the hydrogenic ion with Z charged nucleus discussed in the previous section.

One can show that the transition element can be written as

$$\begin{aligned}
\mathbf{v}_{if}(p \to nlm) &= -\frac{i}{m} \left(Ze^2 m \right)^{-1/2} \int \tilde{\psi}_f^\dagger(\tilde{\mathbf{r}}) \tilde{\nabla} \tilde{\psi}_i(\tilde{\mathbf{r}}) d^3\tilde{r} \\
&= Z^{-1/2} \mathbf{v}_{if}^H (\frac{p}{Z} \to nlm).
\end{aligned} \tag{2.26}$$

Here $\tilde{\psi}_i$ and $\tilde{\psi}_f$ are the initial and final wave functions written in terms of dimensionless variables $\tilde{r} = Ze^2 m r$ and $\tilde{p} = \frac{p}{Ze^2 m}$, and $\tilde{\nabla} = \partial/\partial\tilde{\mathbf{r}}$.

Change of the momentum from p for the hydrogenic ion to p/Z for HI becomes obvious if we examine the energy conservation relation,

$$\frac{p^2}{2m} = E_n^Z + \omega \quad vs. \quad \frac{(p/Z)^2}{2m} = E_n^H + (\omega/Z^2),$$

where $E_n^Z = Z^2 E_n^H = -\frac{Z^2 e^4 m}{2n^2}$ is the energy of an electron on n's level of hydrogenic ions. For the recombination cross section we find

$$d\sigma_{\text{rec}}(p \to nlm) = e^2 Z \frac{1}{Z} \frac{\omega/Z^2 m}{\pi p/Z} |\mathbf{e}\tilde{\mathbf{v}}_{if}^H|^2 d\Omega = d\sigma_{\text{rec}}^H(\frac{p}{Z} \to nlm).$$

---

[1]In this section we work in the standard for QED units $\hbar = c = 1$ to avoid cluttering.

After integration over angles $d\Omega$ and averaging over projections of the orbital moment m and the photon polarizations $\mathbf{e}$, we find $\sigma_{\mathrm{rec}}(p \to nl) = \sigma_{\mathrm{rec}}^{H}(p/Z \to nl)$.

Lastly, to obtain recombination coefficients $\alpha_{nl}(T)$, we need to average $u\sigma_{nl}$ over a Maxwellian distribution for the electrons,

$$\alpha_{nl}(T) = \int\limits_{0}^{\infty} u\sigma_{nl}(p)f(u,T)du, \quad f(u,T) = \frac{4}{\sqrt{\pi}}\left(\frac{m}{2kT}\right)^{3/2}u^2 e^{-\frac{mu^2}{kT}}, \quad p = mu.$$
(2.27)

Changing variables $T \to T^2/Z^2$ and $p \to p/Z$ in the integration, we find the scaling

$$\alpha_{nl}(T) = Z\alpha_{nl}^{H}(T/Z^2).$$
(2.28)

2.8 Application to He^{++}

Here, we use the results from the Appendix A to partially explain the numerical results from Storey & Hummer (1995a). To this end we make a simplifying assumptions that the recombination line emissivities are dominated by recombination rates of He^{++} and H^{+} (then scale this ratio by the energies of their respective photons). The cascade following recombination is determined largely by radiative decay as described by the A-coefficients and to a much less extent by collisions. Under this assumptions we can write the emissivities as linear combinations of the recombination rates:

$$\epsilon(n_1 \to n_2) \simeq \hbar\omega_{n_1 \to n_2}\frac{A_{n_1 \to n_2}}{\sum A_{n_1 \to all}}\sum_{m \geq n_1}\alpha_m C_{m \to n_1}.$$
(2.29)

Coefficients $C_{m \to n}$ describe cascading down from m to n and are the functions of branching ratios. The radiative branching ratios will be the same for HeII as HI since all A-coefficients scale simply as Z^4 (Section 2.7.1). Therefore $C_{m \to n}$ are independent of nuclei charge Z.

The recombination coefficients for HeII and HI, as derived in the Appendix A, scale as

$$\alpha_{nl}^{He^+}(T) \simeq 2\alpha_{nl}^{H}(T/4).$$
(2.30)

For the emissivity of $n\alpha$ line we obtain

$$
\begin{aligned}
\epsilon_{\mathrm{He}^+-n\alpha}(T) &\simeq 2^2\hbar\omega_{n+1\to n}^H \frac{A_{n+1\to n}^H}{\sum A_{n+1\to all}^H} \times 2 \sum_{m\ge n+1} \alpha_m^{\mathrm{H}}(T/4)C_{m\to n+1} \\
&\simeq 8\epsilon_{\mathrm{H}-n\alpha}(T/4).
\end{aligned}
\tag{2.31}
$$

In Figure 2.10 the emissivity ratios from Storey & Hummer (1995b) are shown for HeII at 20000 K compared to HI at 5000 K, illustrating that the numerical results reasonably confirm the approximate analytic prediction of a factor 8 difference.

It is very hard and probably impossible to find exact scaling with temperature of recombination coefficients. So we use the result we found numerically above that

$$
\frac{\epsilon_{\mathrm{H}-n\alpha}(T_1)}{\epsilon_{\mathrm{H}-n\alpha}(T_2)} \simeq \left(\frac{T_1}{T_2}\right)^{-4/3}.
\tag{2.32}
$$
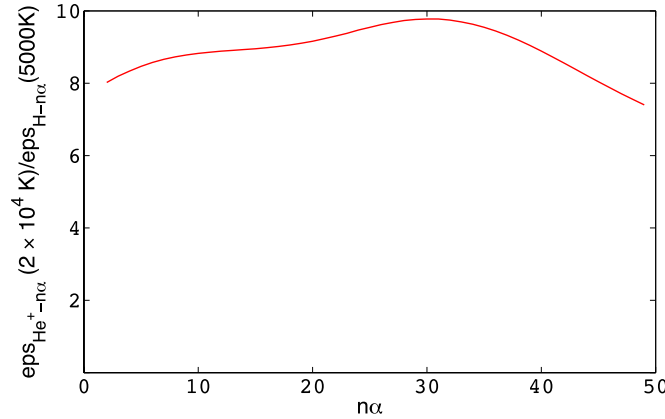
Figure 2.10: The ratio of emissivities for HeII at 20000 K to HI at 5000 K from the full numerical results of Storey & Hummer (1995b) for comparison with the 'analytic' expectation of a ratio = 8.

Combining Equations 2.31 and 2.32, we obtain the following relation between HeII and HI emissivities for the same $n\alpha$ lines:

$$
\frac{\epsilon_{\mathrm{He}^+-n\alpha}(T)}{\epsilon_{\mathrm{H}-n\alpha}(T)} \sim 8\frac{\epsilon_{\mathrm{H}-n\alpha}(T/4)}{\epsilon_{\mathrm{H}-n\alpha}(T)} \sim 8\left(\frac{1}{4}\right)^{-4/3} \sim 50.
\tag{2.33}
$$

The true numerical scaling factor varies between 50 and 65 for $n\alpha \le 50$ (see Fig. 2.4), which reasonably confirms our 'analytical' prediction.

Chapter 3

THE ACCRETION DISK AROUND THE GALACTIC CENTER BLACK HOLE SAGITTARIUS A*

3.1 Abstract

The Galactic Center black hole Sagittarius A* (SgrA*) is the nearest super-massive black hole and thus provides a unique opportunity for observing the black hole's immediate environment and accretion. There exists a variety of models describing black hole accretion mechanisms; however, little is defini-tively known about the accretion processes. This is primarily due to the lack of observational constraints to the accretion flow at $< 10^5$ Schwarzschild radii (R_{Sch}) from the black hole. Our observations provide such a constraint.

In this work, we used a millimeter wavelength recombination line of Hydrogen – H30α – to probe the accretion zone of SgrA* with Atacama Large Millimeter Array (ALMA). We detected and spatially resolved an accretion disk of radius ≤ 0.008 pc ($\sim 10\,000\,R_{\mathrm{Sch}}$), consisting of $\sim 10^4$ K ionized gas. This is the first detection of an accretion disk around the supermassive black hole at the center of our galaxy, and provides a new window for probing black hole physics and accretion.

3.2 Introduction

The supermassive black hole resides in the centre of our galaxy. Its location is identified with a nonthermal radio source hole Sagittarius A* (SgrA*). There is a discrepancy in the estimates of its mass and the distance to it: $M_{\mathrm{SgrA*}} = 4.0 \times 10^6 M_\odot$ and $D_{\mathrm{SgrA*}} = 8.0$ kpc (Boehle et al., 2016), and $M_{\mathrm{SgrA*}} = 4.3 \times 10^6 M_\odot$ and $D_{\mathrm{SgrA*}} = 8.3$ kpc (Gillessen et al., 2017). The black hole's close proximity and the angular size on the sky 2×10^{-5} arcsec large enough to be resolvable with earth-sized interferometer such as Event Horizon Telescope (Doeleman et al., 2009) make it an ideal candidate to study black hole environment, accretion, and physics near the event horizon. A schematic plot of the inner $\sim 1\,\mathrm{pc}$ of the Galactic Center region indicating the main structures and the directions of their rotations is on Figure 3.1.

Understanding accretion onto massive black holes is an important to under-standing the evolution of galaxies, the growth of massive black holes, the
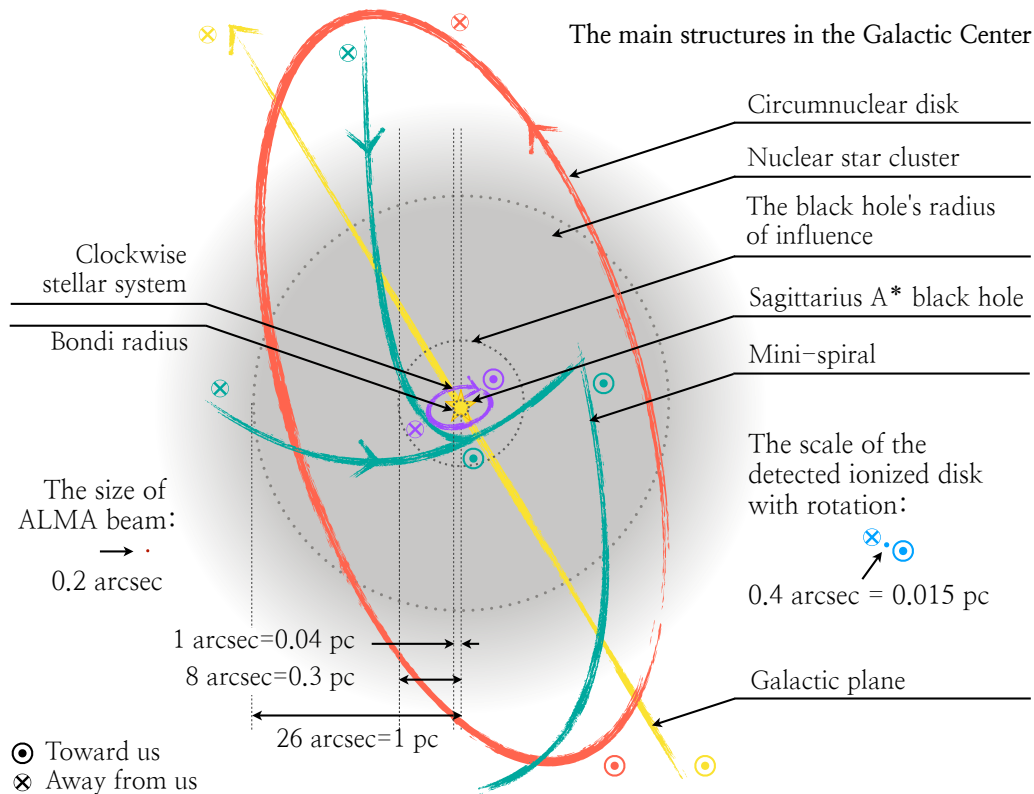
Figure 3.1: A schematic to scale plot of the inner two parsecs of the Galactic Center region. The main structures are indicated by different colors. The distances in pc calculated assuming that the distance to the Galactic Center is $D_{\mathrm{SgrA*}}$ = 8.0 kpc (Boehle et al., 2016). Yellow star: The Galactic Center black hole Sagittarius A*. Red: The the molecular ring, or the circumnuclear disk, containing molecular gas. It is a circle of a radius about 2 pc inclined to the line of sight. Cyan: The mini-spiral consists of three streams of ionized gas rotating counterclockwise either inflowing or orbiting the black hole (Zhao et al., 2016). Filled grey circle: The nuclear star cluster. Most of its mass $\sim 1.0 \times 10^6 M_\odot$ is concentrated within a radius of about 1 pc. The outer boundary extends to a few pc. Yellow: The galactic plane. We look at it edge on which makes it look like a line. The black hole's radius of influence is the radius at which the gravity of the black hole dominates the motion of the stars is at 0.3 pc. The Bondi radius is 0.04 pc. The dark red dot on the left-hand-side: The size half power width diameter of ALMA beam for the present observations. The blue dot on the right-hand-side: The detected 10^4 K disk. The direction of rotation, where relevant, are shown with arrows, the circled cross indicating going away from us, and the circled dot indicating going toward us. The colours of the rotation markers coincides with the color of the rotating structure.

physics of jets, and the black hole physics in general. X-ray measurements of the gas density and temperature at the outer edge of the accretion flow couples with the spherical adiabatic and constant rate of accretion (Bondi, 1952) predicts that the hot-phase accretion rate onto the Galactic Center is $\dot{M}_{\mathrm{Bondi}} \sim 10^{-5} M_{\odot} \, \mathrm{yr}^{-1}$ (Baganoff et al., 2003; Quataert, 2002, 2004). In standard thin disk accretion onto a black hole, the disk radiates between 6% (0 spin) and 42% (maximal spin) of the rest mass of the material falling in. If both the Bondi accretion rate and the thin disk efficiency applied, the luminosity of Sgr A* $\sim 10^{41} \, \mathrm{erg \, s^{-1}}$. This is $\sim 3 \times 10^4$ times greater than the observed $L_{\mathrm{bol}} \sim 3 \times 10^{36} \, \mathrm{erg \, s^{-1}}$ (Mahadevan, 1998).

Extensive theoretical efforts were put into resolving the mystery of Sgr A* accretion and similar black holes with the Radiatively Inefficient Accretion Flows (RIAF): the Advection-Dominated Accretion Flow (Narayan & Yi, 1995), the Advection-Dominated Inflow-Outflow Solution (Blandford & Begelman, 1999) and the Convection-Dominated Accretion Flow (Quataert & Gruzinov, 2000). All of the models deal with a disk which cannot efficiently cool (Phinney, 1981; Rees et al., 1982) and is geometrically thick. This is in contrast to Sakura-Sunyaev disk model (Shakura & Sunyaev, 1973) in which gas cools very efficiently and settles into a thin disk. The physics of the inefficiently cooling disk is as follows. The macroscopic effects transfer energy primarily to the ions. The ions lose only a small fraction of their energy to the electrons through Coulomb scattering on an inflow/heating timescale. As the result the radiation efficiency of such a flow is very low. The gas falling under the horizon radiates only a fraction of $0.1 \dot{M} c^2$.

Here is the brief overview of the RIAF models:

ADAF: Narayan & Yi (1995) proposed an Advection-Dominated Accretion Flow (ADAF). This accretion flow resembles a thick disc rotating at an angular velocity much less that Keplerian velocity $\Omega \ll \Omega_{\mathrm{K}}$. The amount of radiation loss, i.e., the amount of energy transferred from ions to electrons is set to be a free parameter. The black hole is fed at a constant rate and no material escapes. The density of such a disk scales as $\rho \sim r^{-\frac{3}{2}}$.

ADIOS: An ADAF may be unstable to driving a wind. (The binding energy of 1 g of gas at a few R_{Sch} can drive off 500 kg of gas at $\sim 10^5 \, R_{\mathrm{Sch}}$.) The possibility of outflow was pointed out in the original paper (Narayan & Yi, 1995), and analysed by Blandford & Begelman (1999), who derived an

Advection Dominated Inflow Outflow Solution (ADIOS). This accretion model is characterized by the presence of both an inflow and an outflow. It has the geometrical characteristics of the ADAF solution – a thick disk rotating at an angular velocity much less that Keplerian velocity $\Omega \ll \Omega_K$. The disk also has a constant rate of accretion, but because the material is inflowing and outflowing the density profile is less steep $\rho \sim r^{-\frac{3}{2}+p}$, where p is a constant parameter, and the absolute value of the density is lower than the one of the ADAF.

CDAF: Quataert & Gruzinov (2000) pointed out that ADAF may be unstable to convection. They proposed a Convection-Dominated Accretion Flow (CDAF). This accretion flow is marginally stable when the convection dominates advection in carrying the material in. A CDAF's disk is also a thick disc rotating at an angular velocity much less that Keplerian velocity, and feeding the black hole at a constant rate, but the density of such a flow scales as $\rho \sim r^{-\frac{1}{2}}$.

simulations: We should also mention that McKinney et al. (2012) obtained $\rho \sim r^{-1}$ in their numerical simulations which included magnetic fields and a jet.

A detailed fit of no-wind ADAF models to the observed Sgr A* spectra from radio to γ-rays (Mahadevan, 1998; Mahadevan et al., 1997) led to the estimate of the black hole accretion rate at

$$\dot{M}_{\mathrm{SgrA*}} = 7 \times 10^{-6} \left(\frac{\alpha}{0.3}\right) \frac{M_\odot}{\mathrm{yr}}. \tag{3.1}$$

Here α is the dimensionless Shakura-Sunyaev viscosity parameter.

The no-wind ADAF cause a pile up of material in the accretion zone such that it becomes inconsistent with the Faraday rotation measurements (Agol, 2000; Marrone et al., 2007; Quataert & Gruzinov, 2000). Assuming that the magnetic field is ordered and at equipartition strength, the rotation measure constrains the accretion rate at

$$\dot{M} < 2 \times 10^{-7} \frac{M_\odot}{\mathrm{yr}}. \tag{3.2}$$

Inclusion of an outflow solves the pile up issue. The detailed fit of the RIAF models with an outflow to the spectrum of Sgr A* from radio to γ-rays (Yuan
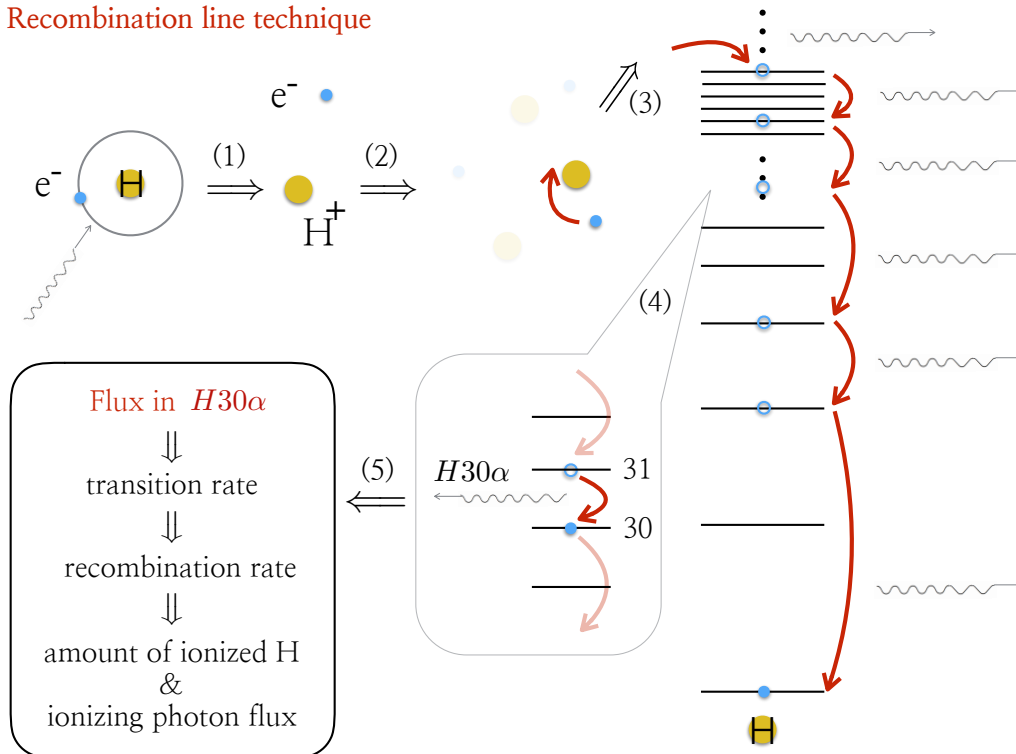
Figure 3.2: Schematic plot illustrating the recombination line technique. If photons with energies $E_\gamma \geq 13.6$ eV are present they ionize neutral hydrogen. As the electrons and the protons recombine, some recombinations occurs to $n \gg 1$. Then the electrons cascades down to the ground level. During the cascade, some electrons pass through the levels of interest, in this case the H30α : n = 31 → 30. The amount of radiation coming out in H30α give us how many H30α transitions are happening, how many atoms are recombining, how much ionized material is in the region, and the background flux of the ionizing photons.

& Narayan, 2014) results in

$$\dot{M}_{\text{Bondi}} \sim 3 \times 10^{-6} M_\odot/\text{yr} \tag{3.3}$$

$$\dot{M}_{\text{SgrA}*} = 1.2 \times 10^{-7} M_\odot/\text{yr}, \tag{3.4}$$

which is consistent with the constraint from the Faraday rotation measurements.

There is, however, no observational evidences for the presence of an outflow near Sgr A*. There is no evidence excluding such a possibility either.

In their recent hydrodynamics simulations of the inner accretion flow of Sgr A*

fueled by stellar winds Ressler et al. (2018) obtained

$$\dot{M}_{\mathrm{SgrA*}} = 2.4 \times 10^{-8} \frac{M_\odot}{\mathrm{yr}} \left(\frac{R}{R_{\mathrm{Sch}}} \right)^{1/2} . \tag{3.5}$$

The general picture of the accretion onto Sgr A* is that the accretion at the Bondi radius is $M_{\mathrm{Bondi}} \sim 3 \times 10^{-6} - 10^{-5} \, M_\odot/\mathrm{yr}$, the accretion near the black hole is $M_{\mathrm{SgrA*}} \sim 10^{-7} - 10^{-8} \, M_\odot/\mathrm{yr}$, and what exactly happens in between is a subject to debate.

It difficult to favor or rule out any of the RIAF models for Sgr A* primarily due to the lack of model-independent observational probes of the gas at between $\sim 10 - 10^5 \, R_{\mathrm{Sch}}$. Part of the reason is that our main source of information about the accretion zone around Sgr A* is X-ray observations by Chandra and XMM, which only probes gas at $T \geq 10^7$ K. However, there is a large reservoir of cooler gas in the Galactic Center in the circumnuclear disk and the mini-spiral. X-ray emission cannot probe this gas and it is, therefore, uncertain how much of this $T \sim 10^4$ K gas accretes onto the black hole. Here we provide such a constraint using a mm recombination line of hydrogen H30α. Scoville & Murchikova (2013) discussed that submm and mm hydrogen recombination lines can serve as a direct probe of the non-X-ray-emitting, ionized gas around Active Galactic Nuclei and in particular Sgr A*. The schematic plot illustrating the recombination line technique is presented on Figure 3.2.

3.3 Results

We observed a millimetre wavelength recombination line of hydrogen H30α line – the transition n = 31 $\rightarrow$ 30 – at 231.9 GHz on ALMA for 5.1 hours. This particular line was selected for it is in mm range and therefore not a subject to dust extinction and it is free from known molecular emission (Crockett et al., 2014). Our observations detect a 2200 km s^{-1} wide line with a double-peaked profile centered at the frequency of H30α within 0.2 arcsec (0.008 pc) radius around Sgr A*.[1] The emission is spatially resolved (Figure 3.3). The spatial distribution of the redshifted and blueshifted parts H30α emission are shown in the bottom panel of Figure 3.3. They are displaced from the centre of the continuum emission of Sgr A* indicated with the white contours. The spatial

---

[1]The extent of the emission is determined by analyzing the spectra within the apertures of a various sizes. An increase in the aperture size beyond 0.2 arcsec does not increase the amount of H30α flux within it. An amount of emission, if any, outside the 0.2 arcsec (0.008 pc) radius around Sgr A* is < 10% of what it is inside.

and spectral structures are consistent with a rotating disk with position angle on the sky ~ 64 degrees.
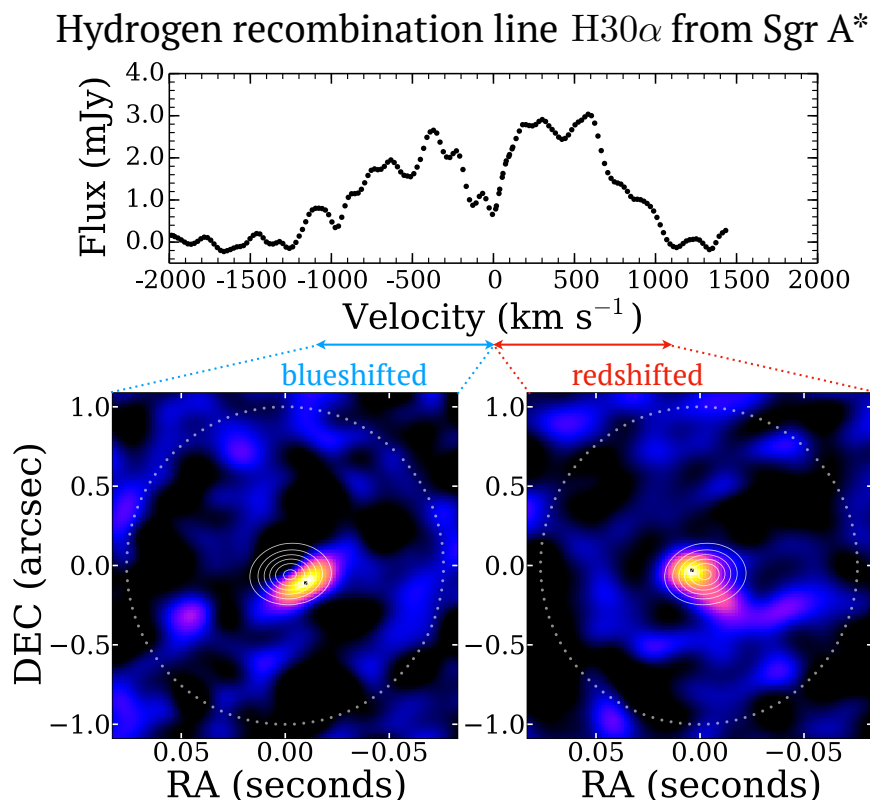
Figure 3.3:   Upper panel: The detection of recombination H30α line from within 0.2 arcsec ($0.008\,\mathrm{p}c$) radius around SgrA* with ALMA Cycle 3. The rest frequency of H30α is at zero velocity. Each point is averaging of the observed spectral data over $50\,\mathrm{km\,s^{-1}}$. Lower panel: The spatial distribution of the blueshifted and the redshifted H30α emission. The white contours indicated the continuum emission from Sgr A* at $\sim$ 220 GHz. Continuum emission is $\sim$ 3.5 Jy. The contour are 0.5, 1.0, 1.5, 2.0, 2.5, 3.0, and 3.5 Jy. The semitransparent white dotted circle indicates the Bondi radius. The images in the bottom panel are $2.2 \times 2.2\,\mathrm{arcsec^2}$. The units on the X-axes are converted to the conventional for RA seconds of time versus DEC's the seconds of arc (arcseconds). The size of the ALMA beam is $0.4 \times 0.3\,\mathrm{arcsec^2}$ with the PA $\simeq 0$.

Let us derive the disk properties. The velocity-integrated line flux of H30α ($S\Delta V_{H30\alpha}$), i.e., the integral under the line in Figure 3.3, allows us to estimate the mass of the disk and the ionizing radiation flux to keep the gas ionized.

The H30α line luminosity is given by the integration over the line emitting

region

$$L_{\text{H30}\alpha} = \int \epsilon_{\text{H30}\alpha} n_e n_p d^3r \tag{3.6}$$

and the flux received by the telescope is

$$S_{\text{H30}\alpha} = \frac{\int \epsilon_{\text{H30}\alpha} n_e n_p d^3r.}{4\pi D^2}. \tag{3.7}$$

Here $\epsilon_{\text{H30}\alpha}$ is the emissivity of H30α which in general is a function of density and temperature, n_e is the electron number density, n_p is the proton number density, and D is the distance to the emitting source.

The integrated line flux is then

$$\int S d\nu = \int S dV \frac{\nu_{\text{obs}}}{c} = S\Delta V_{\text{H30}\alpha} \frac{\nu_{\text{obs}}}{c} = \frac{\int \epsilon_{\text{H30}\alpha} n_e n_p d^3r.}{4\pi D^2}, \tag{3.8}$$

where S in the line flux, c is the speed of light, and V is the radio velocity corresponding to the observed frequency shift from the rest frequency of H30α line ($\nu_{\text{obs}} = \nu_{\text{H30}\alpha}$). We arrive at

$$S\Delta V_{\text{H30}\alpha} = \frac{\int \epsilon_{\text{H30}\alpha} n_e n_p d^3r}{4\pi D^2} \frac{c}{\nu_{\text{obs}}}. \tag{3.9}$$

Substituting $\nu_{\text{obs}} = \nu_{\text{H30}\alpha} = 231.9$ GHz, $D_{\text{H30}\alpha} = 8.0$ kpc, $1\text{Jy} = 10^{-23} \frac{\text{erg}}{\text{s cm}^2 \text{Hz}}$ and $\epsilon_{\text{H30}\alpha}(10^4 \text{ K}, 10^6 \text{ cm}^{-3}) = 1.25 \times 10^{-31} \text{ erg s}^{-1}\text{cm}^3$ (Storey & Hummer, 1995b), we get

$$S\Delta V_{\text{H30}\alpha} = 2.1 \times 10^{-60} \int \frac{\epsilon_{\text{H30}\alpha}(T, n)}{\epsilon_{\text{H30}\alpha}(10^4 \text{ K}, 10^6 \text{ cm}^{-3})} n_e n_p d^3r \qquad \text{Jy km s}^{-1}. \tag{3.10}$$

The emissivity $\epsilon_{\text{H30}\alpha}(T, n)$ varies weakly with n. Here are a few examples:

$$\frac{\epsilon_{\text{H30}\alpha}(10^4 \text{ K}, 10^7 \text{ cm}^{-3})}{\epsilon_{\text{H30}\alpha}(10^4 \text{ K}, 10^6 \text{ cm}^{-3})} = \frac{1.359}{1.251} \quad \text{and} \quad \frac{\epsilon_{\text{H30}\alpha}(10^4 \text{ K}, 10^6 \text{ cm}^{-3})}{\epsilon_{\text{H30}\alpha}(10^4 \text{ K}, 10^5 \text{ cm}^{-3})} = \frac{1.251}{1.08}. \tag{3.11}$$

Therefore for simplicity in what follows we assume that

$$\frac{\epsilon_{\text{H30}\alpha}(T, n)}{\epsilon_{\text{H30}\alpha}(10^4 \text{ K}, 10^6 \text{ cm}^{-3})} \simeq 1. \tag{3.12}$$

Integrating the observed spectra, Figure 3.3, we find the velocity integrated

line flux is

$$S\Delta V_{\mathrm{H}30\alpha} = 3.8 \, \mathrm{Jy \, km \, s^{-1}}, \tag{3.13}$$

and the volume emission measure of the ionized hydrogen (**EM**) derived from Equation 3.10 is

$$\mathrm{EM} = \int n_e n_p d^3 r = 1.8 \times 10^{60} \, \mathrm{cm^{-3}}. \tag{3.14}$$

Let us now estimate the physical properties of the disk and the accretion rate. For simplicity we assume $n_e = n_p = n$.

Let us consider an isothermal disk at $T = 10^4$ K with the outer radius $r_{\mathrm{max}} = 0.2$ arcsec and the inner radius $r_{\mathrm{min}} = 0.1$ arcsec, half opening angle ϕ, such that $h/r = \tan\phi$, where h is the scale height of the disk measured from the midplane to the top, the electron number density

$$n(r) = Cr^{-3/2}, \tag{3.15}$$

where C is the constant to be determined from Equation 3.14. The disk rotates with the azimuthal velocity V_Ω proportional to the Keplerian velocity V_{K} with the proportionality coefficient χ ($V_\Omega = \chi V_{\mathrm{K}}$).

For such a disk the emission measure is given by[2]

$$\mathrm{EM} = \int_{r_{\mathrm{min}}}^{r_{\mathrm{max}}} dr \int_{-r\tan\phi}^{r\tan\phi} dz 2\pi r C^2 r^{-3} = 4\pi \tan\phi C^2 \ln\frac{r_{\mathrm{max}}}{r_{\mathrm{min}}}. \tag{3.17}$$

Making use of the Equations 3.15, 3.14 and 3.17 we find

$$n = \frac{1.2 \times 10^5}{\sqrt{\tan\phi}} \left(\frac{r}{0.2 \, \mathrm{arcsec}}\right)^{-3/2} \left(\frac{\mathrm{EM}}{1.8 \times 10^{60}}\right)^{1/2} \mathrm{cm^{-3}}. \tag{3.18}$$

_____

[2]If we generalize the electron number density to $n(r) = Cr^{-3/2+p}$, where p is a constant (see ADIOS), we find

$$\mathrm{EM} = 4\pi \tan\phi C^2 \frac{r_{\mathrm{max}}^{2p}}{2p}\left[1 - \left(\frac{r_{\mathrm{min}}}{r_{\mathrm{max}}}\right)^{2p}\right]. \tag{3.16}$$

Then the mass accretion rate onto a black hole $\dot{M}$ is given by

$$\dot{M} = 2\pi r 2h(r)V_r\rho(r), \tag{3.19}$$

where V_r is the radial inflow velocity of the gas at the radius r and $\rho = nm_p$ is the gas mass density. Using the standard expression for the radial inflow velocity in the accretion disk

$$V_r = \alpha \left(\frac{h}{r}\right)^2 V_\Omega \tag{3.20}$$

where c_s is the speed of sound and α is the dimensionless Shakura-Sunyaev viscosity parameter, we find

$$\begin{aligned}\dot{M} &= 4\pi r^2 nm_p v_\Omega \alpha \left(\frac{h}{r}\right)^3 \\ &= 3.6 \times 10^{-4} \, (\tan\phi)^{5/2} \left(\frac{\alpha}{0.1}\right) \left(\frac{V_\Omega}{1100\,\mathrm{km\,s^{-1}}}\right) \left(\frac{\mathrm{EM}}{1.8 \times 10^{60}\mathrm{cm^{-3}}}\right)^{1/2} \frac{M_\odot}{.}\mathrm{yr}\end{aligned} \tag{3.21}$$

The scale height of the disk can be estimated using

$$\frac{c_s}{V_\Omega} = \frac{h}{r}. \tag{3.22}$$

The speed of sound in the ideal gas is $c_s = \sqrt{\frac{\gamma p}{\rho}} = \sqrt{\frac{\gamma(n_e+n_p)k_BT}{n_p m_p}} = \sqrt{\frac{\gamma 2k_BT}{m_p}}$. We have

$$c_s = 16.6 \left(\frac{T}{10^4}\right)^{1/2} \mathrm{km\,s^{-1}}, \tag{3.23}$$

then

$$\frac{h}{r} \simeq 0.02 \left(\frac{T}{10^4}\right)^{1/2}, \tag{3.24}$$

and finally

$$n = 0.9 \times 10^6 \left(\frac{T}{10^4}\right)^{-1/4} \left(\frac{r}{0.2\,\mathrm{arcsec}}\right)^{-3/2} \left(\frac{\mathrm{EM}}{1.8 \times 10^{60}}\right)^{1/2} \mathrm{cm^{-3}} \tag{3.25}$$

$$\dot{M} = 1.0 \times 10^{-8} \left(\frac{T}{10^4}\right)^{5/4} \left(\frac{\alpha}{0.1}\right) \left(\frac{V_\Omega}{1100\,\mathrm{km\,s^{-1}}}\right) \left(\frac{\mathrm{EM}}{1.8 \times 10^{60}}\right)^{1/2} \frac{M_\odot}{\mathrm{yr}}. \tag{3.26}$$

A disk with these properties is gravitationally stable, since the Toomre Q is

$$Q = \frac{\Omega c_s}{\pi G \rho h} = \frac{\chi \Omega_K^2}{\pi G m_p n} \sim 6 \times 10^7 \left(\frac{r}{0.2\,\mathrm{arcsec}}\right)^{-3/2} \gg 1. \qquad (3.27)$$

For the material in the disk to be ionized, we need an ionizing photon flux large enough to counteract the recombination loses. Assuming that the disk is in equilibrium, i.e., that the number of recombinations per unit time is equal to the number of ionizations, we get

$$Q_0 = \int \alpha_B n_p n_e d^3 r \simeq \alpha_B \mathrm{EM}. \qquad (3.28)$$

Here Q_0 is the flux of ionizing photons with energies $E_\gamma > 13.6$ eV, and α_B is the sum of the recombination coefficients to all levels $n \geq 2$, i.e., the recombinations resulting in the destruction of an ionizing photon. Using $\alpha_B(T = 10^4\mathrm{K}) = 2.59 \times 10^{-13}$ cm^3, we find

$$Q_0 = 4.6 \times 10^{47} \left(\frac{\mathrm{EM}}{1.8 \times 10^{60}}\right) \mathrm{s}^{-1}. \qquad (3.29)$$

This is more than we could expect from Sgr A*.

Let us then estimate the ionizing photon flux from the surrounding stars. We assume that most of the ionizing flux comes from 15 Wolf-Rayet (WR) stars on the orbits at around 4 arcsec. Most of these stars belong to the counterclockwise disk. The bolometric luminosity of WR stars ranges from $L_{\mathrm{WR}} \sim 10^4 - 10^6 L_\odot$ and we expect $\sim 39\% - 69\%$ of these luminosity emitted at $E_\gamma \geq 13.6$ eV (Crowther, 2007). Therefore these 15 WR stars produce the flux of the ionizing photons of

$$Q_0^{\mathrm{WR}} \sim \frac{15 \times 10^5 L_\odot \times 0.55}{13.6 \times 1.6 \times 10^{-12}} \times \frac{\pi(0.2\mathrm{arcsec})^2}{4\pi(4\mathrm{arcsec})^2} \sim 0.9 \times 10^{46}\,\mathrm{s}^{-1}. \qquad (3.30)$$

near the location of the disk.

This estimate can be considered as an upper limit, since the characteristics of WR stars vary widely and the emitted EUV may sustain a considerable losses before reaching the disk due to the presence of neutral hydrogen in the region. There is a factor of ~10 tension with our estimations from the H30α emission.

There is a more pressing issue, however. If we assume that the value of the emission measure is in Equation 3.14 we must expect the detection of the disk

in Brγ. Indeed

$$\frac{S\Delta V^{\mathrm{obs}}_{\mathrm{Br}\gamma}}{S\Delta V_{\mathrm{H}30\alpha}} = \frac{\epsilon_{\mathrm{Br}\gamma}}{\epsilon_{\mathrm{H}30\alpha}} \frac{\nu_{\mathrm{Br}\gamma}}{\nu_{\mathrm{H}30\alpha}} 10^{-a/2.5} = 5.2 \qquad (3.31)$$

Here we used that the extinction toward the galactic center at the frequencies of Brγ is $a = 2.1$. We expect to see a double peaked Brγ line with a maximal value of the flux ~ 15 mJy. But no Brγ from this region were observed. The detection limit for Brγ is around ~ 0.1 Jy. In order to see no Brγ our emission measure must be al least a factor of ~ 100 lower than the estimate in Equation 3.14:

$$\left(\frac{\mathrm{EM}}{1.8 \times 10^{60}}\right) \leq 10^{-2}. \qquad (3.32)$$

But how can we observe that much H30α emission as in Figure 3.3, if our emission measure is a factor of ~ 100 times lower? For the estimations above we used an extremely simplified model. In reality the disk is heated by magneto-viscous dissipation and external radiation, most relevantly the continuum associated with the black hole with the temperature of $\sim 10^4$ K and the peak of the spectra at $\sim \nu_{\mathrm{H}30\alpha}$. Also at large values of n, the occupancy of the levels is determined by collisions, whereas at low values of n (Brγ) spontaneous emission dominates. At intermediate values of n ~ 30 (H30α) collisions, spontaneous and stimulated emission and absorption are all important and possibly enhance the emissivity of H30α relative to the Brγ. The exact calculation of the relative fluxes requires further investigation.

3.4 Conclusion

We detected a cool 10^4 K accretion disk around the Milky Way's Galactic Center black hole Sgr A* using a novel probe for this region a mm recombination line of hydrogen H30α, which is a reliable probe of the 10^4 K gas in the accretion on zone of Sgr A*, unobservable in X-rays. The disk is spatially resolved. It extends to about 0.008 pc (0.2 arcsec) and has position angle on the sky of ~ 64 degrees. It rotates in the direction consistent with the main structures at the Galactic Center. Our analysis shows that the disk is gravitationally stable. If we assume the the temperature of the disk is $T = 10^4$ K we conclude that it possesses thin disk geometry $h/r \sim 0.02$. This would be inconsistent with the RIAF accretion models (ADAF, ADIOS and CDAF) all of which possess thick disk geometries. However, the observed emission, instead

of coming from a smooth disk, might be distributed over a vast number of tiny 10^4 K cloudlets, similar to the broad region of quasars and Seyfert galaxies. In this case the distribution of the cloudlets might easily form a thick torus. This uncertainty can be resolved with higher resolution ALMA observations. (We have proposed eight times higher resolution observations than the ones presented here for ALMA Cycle 6.)

Our limits on the disk density and accretion rate are

$$n \le 1.7 \times 10^5 \left(\frac{T}{10^4}\right)^{-1/4} \left(\frac{r}{0.2\,\text{arcsec}}\right)^{-3/2} \left(\frac{\text{EM}}{1.8 \times 10^{58}}\right)^{1/2} \text{cm}^{-3} \quad (3.33)$$

$$\dot{M} \le 1.0 \times 10^{-9} \left(\frac{T}{10^4}\right)^{5/4} \left(\frac{\alpha}{0.1}\right) \left(\frac{V_\Omega}{1100\,\text{km s}^{-1}}\right) \left(\frac{\text{EM}}{1.8 \times 10^{58}}\right)^{1/2} \frac{M_\odot}{\text{yr}}. \quad (3.34)$$

The inequalities are due to the limit set on the volume emission measure of the disk from non-detection of Brγ and the necessity of a careful account for the external radiation and inverted population on n $\sim$ 30, leading to potential relative increase of H30α emission with respect to Brγ. This is the topic of our followup study.

In our future observations we will study the extent of the line beyond $\sim$ 3000 km s^{-1} unavailable in this observations and reach $\sim$ 20 000 km s^{-1} (the ALMA Cycle 5). We also study the effects of the S2 star close flyby by Sgr A* on the disk (the ALMA Cycle 4 and Cycle 5).

The discovery of a 10^4 K disk within $\sim 2 \times 10^4 R_{\text{Sch}}$ around Sgr A* provides a new model independent window into studying the accretion onto supermassive black hole, bringing us closer to understanding its mechanisms.

3.5   Acknowledgements:
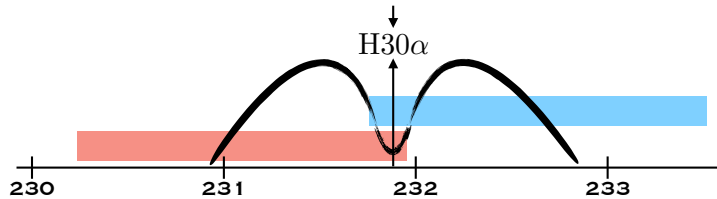
Figure 3.4: ALMA spectral window configurations for our ALMA Cycle 3 observations. The observations have two spectral windows (blue and red) positioned across the line with an overlap. The frequency of the H30α line is marked with an arrow. The double peaked line between 231 GHz and 233 GHz is a schematic drawing of the detected line.

senting its member states), NSF (USA) and NINS (Japan), together with NRC (Canada) and NSC and ASIAA (Taiwan) and KASI (Republic of Korea), in cooperation with the Republic of Chile. The Joint ALMA Observatory is operated by ESO, AUI/NRAO and NAOJ.

The National Radio Astronomy Observatory is a facility of the National Science Foundation operated under cooperative agreement by Associated Universities, Inc.

3.6   Appendix

3.6.1   Observations

These ALMA Cycle 3 observations in H30α line were obtained in 2016 April and August for project 2015.1.00311.S.

The observations discussed here were conducter in receiver Band 6; the correlator was configured in the time division mode (TDM) with 4 spectrometers. Each spectrometer had a full bandwidth of 1875 MHz with 1.95 MHz resolution spectral channels. Because the width of the line was comparable with the bandwidth of the individual spectrometers, we positioned two spectral windows centred at 231.058 GHz and 232.608 GHz to overlap, see Figure 4.28; the remaining two spectral windows were centred at 217.801 GHz and 215.801 GHz to image the SgrA* continuum.

The observations were primarily done in ALMA configuration C40-5 with baselines up to 1.1 km and one execution was done in configuration C36-2/3 with baselines up to 460 m. For the C40-5 telescope configuration, good flux recovery is expected out to scales of ~ 3.4 arcsec and for C36-2/3 it is expected up to ~ 10.7 arcsec. Extended emission with spatial size greater than this will be partially resolved out. The data were taken with 43 12 m antennas and the total AMA time used by the observations was 5.1 hours (including calibra-

tions). The total integration time (excluding calibration) was 1.6 hours. The synthesized beam size was 0.4×0.3 arcsec^2 with PA$\simeq 0$.

J1924-2914 was used as a bandpass calibrator. J1744-3116 or J1717-3342 were used as a phase calibrators.

Following delivery of data products, the data was re-reduced and imaged using the Common Astronomy Software Applications package (CASA). We did not perform self-calibration, as it is a mathematically ill-defined procedure. The images were made with the parameter Robust $= 1$. The cleaned images with no continuum subtraction were used to identify the line free channels. We then performed UV continuum subtraction using these channels. Further analysis was performed in Python and Mathematica.

Channel averaging over 8 of the original channels was done to reduce noise, resulting in data with velocity resolution of $40\,\mathrm{km\,s^{-1}}$ with no compromise relative to the observed line width ($\delta V = 2200\,\mathrm{km\,s^{-1}}$). The 1σ (rms) sensitivity is 0.3 mJy beam^{-1} in each 40 km s^{-1} channel.

The velocities given here are $V_{\mathrm{radio}} = c\frac{\nu_{\mathrm{rest}} - \nu}{\nu_{\mathrm{rest}}}$ relative to the LSR. The Sgr A* observations were centered on $V_{\mathrm{LSR}} = 0.0\,\mathrm{km\,s^{-1}}$.

3.6.2 Observational difficulties and reliability

We observed $\sim 2200\,\mathrm{km\,s^{-1}}$ wide ~ 2 mJy line emission on top of the 3.5 Jy of primarily synchrotron continuum of Sgr A*. To achieve this we needed excellent bandpass calibrations, the bandpass to be repeated at least every 30 min.

The width of the line was comparable with the width of the spectral window, so the observation required one line to be observed in two spectral windows. But because the ALMA spectral windows are calibrated separately, and there is usually a misalignment in the absolute value and the spectral slope of the data taken with one spectrometer with respect to the other, we positioned spectrometers with overlap and used the overlapping parts of the spectra to ensure that separate spectra windows are consistently aligned. We used an overlap of about 25 channels, which left us with ~ 15 useful channels, as about 10 channels at the end of each spectral window are unusable.

To test the reliability of our data we performed the following tests:

1. We divided the data into pieces and processed them independently without reference to each other and then compared the final spectra. We
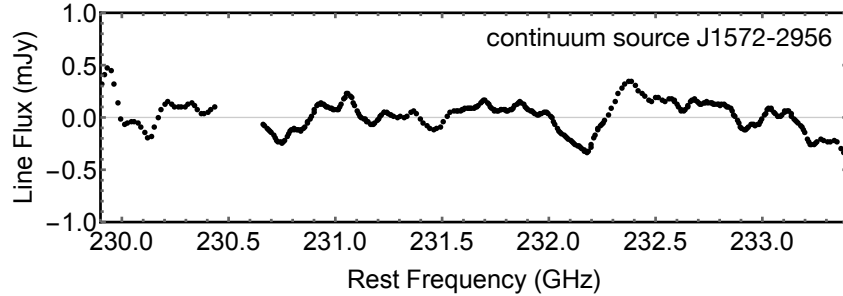
Figure 3.5: The spectrum of a continuum source J1572-2956 used as a check source. The gap in the spectra around 230.5 GHz is due to the CO (2-1) emission. No similar double peaked emission centered on $\nu_{\text{H30}\alpha} = 231.9$ GHz is seen here.

recovered the same spectral features as in the combined data;

2. We observed a continuum sources J2000-1748 or J1752-2956, which were then calibrated in the same way as Sgr A*, to check for the possible technical or data reduction errors (Figure 3.5). No spectral features analogues to those on Figure 3.3 were detected.

3.6.3   Uncertainties

1. We assumed the mass of the black hole and the distance to the Galactic Center as given in Boehle et al. (2016). Replacing these values by those in Gillessen et al. (2017) we will see a 5% increase of our estimations of the scale of the disk. And therefore $\sim$ 3% decrease in density.

2. The sensitivity of the observation is $\delta S = 0.3$ mJy in each 40 $\text{km}\,\text{s}^{-1}$ channel.

3. We tested possible uncertainties which can be introduced by the combination of the imperfect continuum subtraction, caused by the use of incorrect "line free" channels, subsequent task TCLEAN applied to the sloped spectra, and then matching the overlapping parts of the spectra by removing the slope from the spectra through subtraction of a straight line $a\nu + b$, with a and b constants. We experimented primarily with the imperfect continuum subtraction resulting in the slope of the order $\leq 10 \times S_{\text{max}} \sim 30$ mJy. We concluded that uncertainties introduced this way are $\leq 7\%$ relative to the value of each point in the spectra. The trend is that the task TCLEAN makes point with a high value even higher. We estimate the uncertainties due to variations in UV continuum subtraction and subsequent TCLEAN at 5% on average.

4. Overlapping channels constraining the alignment of the separate spectral windows allow variation of the total alignment. The variations in the spectral windows alignment might result in up to 10% discrepancy.

5. The molecules with lines within ~ 1 GHz around H30α are too complex to be present in substantial quantities in 10^4 K ionized gas – acetone, methanol, sulfur dioxide $^{33}SO_2$, and similar ones (Remijan et al., 2016). However it is hard to exclude possibility of narrow absorption or emission features from the foreground. A presence of the absorption feature might contribute to the to sharpness of the dip in the center of the double peaked profile of the H30α line. The spectrum also shows a relatively narrow $150\,\mathrm{km\,s^{-1}}$ bump at 231.43 GHz, which might be due to foreground emission. This feature is responsible for $0.2\,\mathrm{Jy\,km\,s^{-1}}$ in the total velocity integrated line flux $S\Delta V_{\mathrm{H}30\alpha}$ in Equation 3.13.

6. We explore a relatively narrow spectral range of frequencies, while the wings of the line might extend further than $\pm 1000\,\mathrm{km\,s^{-1}}$ from the central frequency. We are unable to test this with the observations presented here. This issue be resolved by our ALMA Cycle 5 observations which will be conducted in the spectral scan mode and cover $\sim 20\,000\,\mathrm{km\,s^{-1}}$.

Combining the above factors we access the uncertainties at $\sim \pm 20\%$.

Chapter 4

ANALYTIC CLOSURES FOR M1 NEUTRINO TRANSPORT

Carefully accounting for neutrino transport is an essential component of many astrophysical studies. Solving the full transport equation is too expensive for most realistic applications, especially those involving multiple spatial dimensions. For such cases, resorting to approximations is often the only viable option for obtaining solutions. One such approximation, which recently became popular, is the M1 method. It utilizes the system of the lowest two moments of the transport equation and closes the system with an ad hoc closure relation. The accuracy of the M1 solution depends on the quality of the closure. Several closures have been proposed in the literature and have been used in various studies. We carry out an extensive study of these closures by comparing the results of M1 calculations with precise Monte Carlo calculations of the radiation field around spherically-symmetric protoneutron star models. We find that no closure performs consistently better or worse than others in all cases. The level of accuracy a given closure yields depends on the matter configuration, neutrino type, and neutrino energy. Given this limitation, the maximum entropy closure by Minerbo (1978) on average yields relatively accurate results in the broadest set of cases considered in this work.

4.1 Introduction

Neutrinos play an important role in core-collapse supernovae (CCSNe), coalescence of binary neutron stars and many other astrophysical phenomena. Their collective behavior is described by the distribution function that obeys the Boltzmann transport equation. The state of the radiation field is characterized by spatial coordinates, the propagation direction (two angles), energy, and time, making the problem seven-dimensional in the most general case. Many astrophysical systems have dense and opaque central regions surrounded by transparent low-density envelopes. Radiation moves within the dense central regions via diffusion and, when it leaks into the outer regions, it streams freely. The transport equation has a parabolic character in the former region, while in the latter region, it has a hyperbolic character (e.g., Mihalas & Mihalas, 1984; Pomraning, 1983). In order to model such systems accurately, the solution techniques must handle not only the two different regimes, but also

the transition between the two. In the presence of scattering, the collision terms on the right-hand side of the Boltzmann equation contains the angular moments of the specific intensity, which makes the Boltzmann equation an integro-differential equation. These aspects make solving the transport equation a challenging computational task. For this reason, often one has to resort to approximations and simplifications to make the problem tractable.

One way of simplifying the problem is to assume spherical or axial symmetries to reduce the number of spatial dimensions. There are many situations where such assumptions have been employed. Spherically-symmetric calculations have been performed by, e.g., Liebendörfer et al. (2005); Mezzacappa & Bruenn (1993a,b,c); Rampp & Janka (2000); Sumiyoshi et al. (2005); Yamada (1997). 2D axisymmetric simulations have been performed by, e.g., Brandt et al. (2011); Burrows et al. (2016); Livne et al. (2004); Ott et al. (2008); Skinner et al. (2016). In addition, ray-by-ray approaches, in which multi-dimensional transport problem is approximated as a set of one-dimensional problems along radial rays, has been used widely (e.g., Bruenn et al., 2013, 2016; Buras et al., 2006; Burrows et al., 1995; Lentz et al., 2015; Marek & Janka, 2009; Melson et al., 2015a,b; Müller, 2015; Müller & Janka, 2015; Müller et al., 2012a,b). Most realistic problems, however, do not possess spatial symmetries. For these problems, the transport equation has to be solved in full three dimensions. The pioneering attempts to solve three-dimensional Boltzmann equation have been already taken (e.g., Radice et al., 2013; Sumiyoshi & Yamada, 2012; Sumiyoshi et al., 2015), yet the computational cost remains too high for solving it in realistic scenarios.

In order to further reduce the cost, one can approximate the Boltzmann equation either by neglecting the time dependence (*s*teady-state solution) and/or energy dependence (*g*ray schemes). The simplest treatment of the transport problem is the "light bulb" approach, in which simple parametrized neutrino heating and cooling rates are imposed (e.g., Murphy & Burrows, 2008; Ohnishi et al., 2006; Radice et al., 2016). The less cruder approximation, the so-called leakage/heating scheme, has been used extensively in the literature (e.g., Abdikamalov et al., 2015; Deaton et al., 2013; Mösta et al., 2014; O'Connor & Ott, 2011; Ott et al., 2012, 2013a,b; Rosswog & Liebendörfer, 2003; Ruffert et al., 1996). The leakage/heating scheme evaluates the local neutrino energy and number emission rates, which are then locally subtracted from the matter. A fraction of the emitted energy is deposited back as neutrino heating in the "gain" region outside the protoneutron star (PNS)(e.g., O'Connor & Ott, 2010;

Ott et al., 2013b).

In this paper we focus on an alternative approach, employing the reduction of the angular degrees of freedom of the problem, called the *m*oment scheme. The simplest version of the moment scheme is the diffusion approximation. One takes the zeroth moment of the transport equation, which yields an equation that contains the zeroth and first moments of the distribution function. For non-static moving media, the third moment is also present (e.g., Just et al., 2015). These three moments represent the energy density, flux, and pressure tensor of radiation, respectively. In the optically thick limit, the first moment can be approximated using the gradient of the zeroth moment via the Fick's law, while the second moment can be approximated as one-third of the zeroth moment (e.g., Pomraning, 1983). These relations allows us to "close" the zeroth moment of the transport equation. While the resulting equation is far simpler than the original Boltzmann equation, the diffusion approximation is not valid in the free-streaming regime and yields inaccurate results such as acausal flux. This can be mitigated by using the flux limiter (e.g., Burrows et al., 2000; Smit et al., 2000) or by using other advanced prescriptions (e.g., Dgani & Janka, 1992; Müller & Janka, 2015; Scheck et al., 2006). The way to obtain a more accurate solution is to incorporate higher-order moments.

The first moment of the transport equation results in an equation containing up to the second moments of the distribution function. In general relativity and for non-static media, the third moment is also present (Cardall et al., 2013; Just et al., 2015; Shibata et al., 2011). Together with the zeroth moment of the transport equation the system has four sets of unknowns: the zeroth, first, second, and third moments. There are two commonly used approaches for closing the system. In the first method, using the first and second moments as given, one can express the source terms of the Boltzmann equation due to interaction with matter as functions of only space, time, and momentum coordinates (Burrows et al., 2000; Rampp & Janka, 2002). This transforms the Boltzmann equation from a non-linear integro-differential equation into a linear differential equation. The solution of this simpler equations yields higher moments to close the original system of the lowest two moment equations, from which we can obtain updated zeroth and first moments. This procedure is iterated until convergence. Depending on the method for obtaining the closure, the approach can yield the full solution of the Boltzmann equation. This method is usually called the variable Eddington tensor method (Burrows et al., 2000; Cardall et al., 2013; Rampp & Janka, 2002).

Another approach for closing the system is by expressing the second and the third moments in terms of the lower-order moments using *a*pproximate analytical relations. This results in a closed system of two equations for the zeroth and first moments. Originally proposed by Kershaw (1976); Levermore (1984); Pomraning (1969), such methods are often called the M1 methods (Audit et al., 2002; Pons et al., 2000; Smit et al., 1997) or the "algebraic Eddington factor" methods (Just et al., 2015).

A common way to derive a closure relation by interpolating between optically thick and optically thin limits. In these limits, the second and third moments can be expressed precisely in terms of the zeroth and first moments[1]. The Eddington factor, which ranges from 1/3 to 1 between these limits, serves as an interpolation parameter. The functional form of the Eddington factor in terms of the local energy density and flux of radiation is a relation often called the M1 closure in the literature. Once this relation is established, the system is closed (e.g., Shibata et al., 2011)[2].

The M1 approach is particularly suitable for problems with not too complex geometries such as CCSNe and remnants neutron star mergers. In these problems, the radiation field is often arranged in such a way that there exists some approximate relationship between higher-order and lower-order moments. That said, not all problems possess such properties. A prominent example is a collision of radiation beams coming from multiple sources. For this problem, the closure relation depends not only on the local values of the first and second moments, but also on the spatial distribution of the radiation sources. In general, if the second and third moments are assumed to be functions of the zeroth and first moments, then the former two must be symmetric with respect to rotation around the direction of the radiation flux (e.g., Cardall et al., 2013). For problems with such symmetries, the M1 approach offers excellent compromise between computational cost and accuracy.

Moreover, the moment equations constitute a hyperbolic system, which allows

---

[1]More specifically, in the optically thin limit, one can derive an expression for the second and third moments for a freely propagating radiation beam (e.g., Shibata et al., 2011).

[2]This is not the only approach for closing the system that exists in the literature. In principle, if the second and third moments are assumed to be functions of the local values of the lowest two moments, then the second moment can be expressed in terms of the latter two via the Eddington factor (e.g., Just et al., 2015). Similarly to the second moment, the third moment can be expressed in terms of the lowest two via the "third-order counterpart" of the Eddington factor. To close the system, this factor must be expressed in terms of the radiation energy density and flux, which has been achieved by, e.g., Vaytet et al. (2011) and Just et al. (2015) for two different closures.

us to utilize a wide variety numerical methods developed for solving hyperbolic system of conservations laws (e.g., Godunov-type methods) to calculate the solution of the transport problem (Pons et al., 2000). For these reasons and because of their relatively modest computational cost, such methods recently gained significant popularity in astrophysics.

The M1 method has been applied to a wide range of problems such as core-collapse supernovae (e.g., Kuroda et al., 2016; O'Connor & Couch, 2018; Roberts et al., 2016), evolution of protoneutron stars (Pons et al., 2000), accretion disks (e.g., Foucart et al., 2015; Just et al., 2015, 2016; Shibata & Sekiguchi, 2012), and many more in AGN accretion literature. A number of analytical closures have been suggested in the literature. The accuracy of the M1 solution depends on the quality of the closure used and it is a priori unclear which closure yields the best results for a given problem. While the quality of individual closures has been examined in different contexts (e.g., Janka, 1991; O'Connor, 2015; Smit et al., 1997), a systematic analysis for neutrino transport has been performed only by Janka (1991), Smit et al. (2000), and Just et al. (2015)[3]. The aim of this work is to extend these two works, consider a wider selection of M1 closures, verify them using a wider range of test problems that are relevant to neutrino transport, and present a quantitative assessment of their quality.

In this work, we evaluate the quality of various closures proposed in the literature by comparing the radiation field distribution in and around radiating objects obtained with the M1 method with the one obtained analytically or with Monte Carlo. We consider two types of radiating objects: a uniform sphere with a sharp surface and a protoneutron star with a hot envelope obtained from core-collapse simulations. These two objects possess the opaque central radiating source surrounded by a transparent envelope, i.e. the important characteristics common to many astrophysical systems. Since our goal is to study the quality of the analytical closures and in order not to contaminate our results with errors emanating from other sources such as hydrodynamics and non-linear radiation-matter coupling, we consider only static matter configurations in our tests. For simplicity, we limit ourselves to spherical sym-

---

[3]Note that there is a relation between the M1 scheme and the flux-limited diffusion approximation and each flux limiter is associated with an M1 closure relation (Levermore, 1984; Smit et al., 2000). The quality of some of the flux limiters has been explored by, e.g., Burrows et al. (2000); Just et al. (2015) using the flux-limited diffusion framework for neutrino transport in the context of core-collapse supernovae.

metry and ignore spacetime curvature around PNSs. Implications of these assumptions will be discussed in Section 4.5.

The uniform sphere problem consists of an opaque radiating sphere with a sharp surface surrounded by vacuum, and it has an analytical solution (cf. Section 4.4.2). In the PNS problem, we take three different post-bounce configurations (obtained from simulations of Ott et al. 2008) of a $20M_\odot$ progenitor star at 160, 260, and 360 ms after bounce. We obtain precise solution of this problem by performing Monte Carlo radiation transport calculations using the code of Abdikamalov et al. (2012) (cf. Section 4.4.3). These solutions are compared to M1 solutions obtained using the GR1D code (O'Connor, 2015; O'Connor & Ott, 2011, 2013) available at http://www.GR1Dcode.org.

We consider seven different closures. These are the closures by Kershaw (1976), Wilson et al. (1975), Levermore (1984), the classical maximum entropy closure of Minerbo (1978), and the maximum entropy closure with the Fermi-Dirac distribution by Cernohorsky & Bludman (1994). In addition, we consider two closures by Janka (1991) that are constructed by fitting closure relations to exact Monte Carlo solutions of the radiation field around PNSs (Janka, 1991).

This paper is organized as follows. In Section 4.2, we give a theoretical overview of the neutrino transport problem and the M1 scheme. In Section 4.3, we give a brief description of the seven closures we study in this work. Section 4.4 presents the details of the test problems. We also describe our tools for systematic quantitative assessment of the quality of the closure relations and present the results of our analysis. Our conclusions are provided in Section 4.5. In Appendix 4.6, we describe the two codes that we use in our analysis: the GR1D code for M1 transport and the Monte Carlo code of Abdikamalov et al. (2012).

4.2 Boltzmann Equation and M1 method

Neutrinos are described by the distribution function $\mathcal{F}$, which characterizes the number of neutrinos in a phase-space volume element and which obeys the relativistic Boltzmann equation (e.g., Lindquist, 1966; Mezzacappa & Matzner, 1989):

$$\frac{dx^\alpha}{d\tau}\frac{\partial \mathcal{F}}{\partial x^\alpha} + \frac{dp^i}{d\tau}\frac{\partial \mathcal{F}}{\partial p^i} = (-p^\alpha u_\alpha)S(p^\mu, x^\mu, \mathcal{F}) \ . \tag{4.1}$$

Here, τ is an affine parameter of the neutrino trajectory, u^μ is the four-velocity of the medium, and p^μ is the four-momentum of radiation, from which one can obtain the neutrino energy in the rest frame of the medium via relation $\varepsilon = -p^\alpha u_\alpha$. The Greek indices $\mu, \alpha = 0, 1, 2, 3$ run over space-time components and the Latin indices $i = 1, 2, 3$ runs over the spatial components. $S(p^\mu, x^\mu, \mathcal{F})$ is the collision term that describes the interaction of radiation with matter via absorption, emission and scattering. The evaluation of $S(p^\mu, x^\mu, f)$ is a domain of a separate field of study and it is beyond the scope of this work (e.g., Bruenn, 1985; Burrows et al., 2006). In this work, we treat neutrinos as massless particles and fix units using $\hbar = c = 1$.

The zeroth, first, and second moments of the distribution function represent the energy density,

$$E_\nu = \int \varepsilon \mathcal{F}(p^\mu, x^\mu)\delta(h\nu - \varepsilon)d^3p, \tag{4.2}$$

the radiation flux,

$$F_\nu^j = \int p^j \mathcal{F}(p^\mu, x^\mu)\delta(h\nu - \varepsilon)d^3p, \tag{4.3}$$

and the radiation pressure,

$$P_\nu^{ij} = \int p^i p^j \mathcal{F}(p^\mu, x^\mu)\delta(h\nu - \varepsilon)\frac{d^3p}{\varepsilon}. \tag{4.4}$$

Here, E_ν, F_ν^j, and P_ν^{ij} are the functions of neutrino energy $\varepsilon = p^0 = |\vec{p}|$. In order to obtain the total energy density, flux, and pressure, one has to integrate (4.2)-(4.4) over energy, as discussed in, e.g., Novikov & Thorne (1973); Thorne (1981).

The zeroth and the first moments of the Boltzmann equation constitute the system of equations for E_ν and F_ν^j. In Minkowski space, spherical symmetry, and neglecting the velocity of the medium, these two evolution equations are

$$\frac{\partial}{\partial t}E_\nu + \frac{1}{r^2}\frac{\partial}{\partial r}\left(r^2 F_\nu^r\right) = S[0]_\nu \tag{4.5}$$

$$\frac{\partial}{\partial t}F_\nu^r + \frac{1}{r^2}\frac{\partial}{\partial r}\left(r^2 P_\nu^{rr}\right) = S[1]_\nu^r, \tag{4.6}$$

where $S[0]_\nu$ and $S[1]_\nu$ are accordingly the zeroth and first moments of the collision term $S(p^\alpha, x^\beta, \mathcal{F})$. Note that, since we consider flat spacetime and

static matter, the third moment does not appear in this equation. As we pointed out above, this system is not closed. There are two equations (4.5) and (4.6), but three unknowns E_ν, F_ν^r, and P_ν^{rr}. This is a simple reflection of the fact that, although the system (4.5)-(4.6) is obtained from the Boltzmann equation, it does not capture all the information contained in the Boltzmann equation. To capture the complete information, one has to solve the complete system, which can be expressed as

$$\text{Function}(M[0]...M[k+1]) = S[k], \tag{4.7}$$

where

$$M[k]_{\varepsilon_0}^{\alpha_1...\alpha_k} = \int \varepsilon^2 \mathcal{F}(p^\mu, x^\mu)\delta(h\nu - \varepsilon)\frac{p^{\alpha_1}}{\varepsilon}...\frac{p^{\alpha_k}}{\varepsilon}\frac{d^3p}{\varepsilon}, \tag{4.8}$$

is the moment of order k. Note that subscripts and superscrips are omitted in this equation to avoid clutter. This is an infinite system of an infinite number of unknowns $M[k]$, which is not feasible to solve in practice.

This situation is somewhat analogous to the Taylor expansion. Function $f(x)$ can be represented through the infinite sum

$$f(x) = \sum_N \frac{1}{N!}\frac{d^N f(x)}{dx^N}\bigg|_{x=x_0}(x-x_0)^N. \tag{4.9}$$

This allows one to express the value of $f(x)$ at an arbitrary point x through its properties at a given point x_0. In order to calculate $f(x)$ exactly, one has to incorporate all the terms in the infinite series. The low-order terms yield accurate results only in the vicinity of the point x_0. Similar is true for the moments of the distribution function. When we constrain ourselves to the first few moments, we sacrifice the accuracy of our description. To capture all the information contained in the distribution function one needs to employ the whole infinite set of moments.

The M1 approach used in the literature is based on an interpolation of the radiation pressure P^{ij} between optically thick and thin limits (e.g., Shibata et al., 2011)

$$P_\nu^{ij} = \frac{3p-1}{2}P_{\text{thin}}^{ij} + \frac{3(1-p)}{2}P_{\text{thick}}^{ij}, \tag{4.10}$$

where P_{thick}^{ij} and P_{thin}^{ij} are the radiation pressure in these limits. In the former

limit, radiation is in thermal equilibrium with matter and is isotropic. This results in $F_\nu^i = 0$ and

$$P_{\text{thick}}^{ij} = \frac{1}{3} E_\nu \delta^{ij} \tag{4.11}$$

for the gas of ultrarelativistic particles such as photons and neutrinos (Mihalas & Mihalas, 1984). In the free-streaming limit, radiation propagates like a beam along a certain direction n and exerts pressure only along this direction, giving us $F_\nu^n = E_\nu$ and $F_\nu^{i \neq n} = 0$ and

$$P_{\text{thin}}^{nn} = E_\nu \frac{F_\nu^n F_\nu^n}{|F_\nu|^2}, \quad \text{and} \quad P_{\text{thin}}^{ij} = 0, \text{ if } i \text{ or } j \neq n. \tag{4.12}$$

The parameter p in equation (4.10) is known as the variable Eddington factor and it plays the role of the interpolation factor between the two regimes. The functional form of p in terms of the lower moments is referred to as the M1 closure.

Equation (4.10) is derived based on the assumption that the radiation is symmetric around the direction parallel to the flux. While the assumption is valid for the spherically symmetric matter and radiation distributions, it does not always hold in more general cases. Colliding radiation beams emanating from different sources is a prominent example. Therefore, equation (4.10), even before we fix the form of the function p, already contains an approximation.

Note that equation (4.10) in its modern form is often cited as derived by Levermore (1984) in the literature. While it is true, Kershaw (1976) also proposed the interpolation between thick and thin regimes like (4.10). He then suggested using the simplest among such interpolation

$$P_\nu^{ij} = E f^i f^j + \frac{E}{3} \delta^{ij} \left(1 - f^2\right), \tag{4.13}$$

where

$$f^i = F_\nu^i / E_\nu \tag{4.14}$$

and $f^2 = f^i f_i$. This relation is equivalent to equation (4.10) with a closure relation $p = (1 + 2f^2)/3$, which is known as the Kershaw closure. Even earlier, a formulation similar to M1 was discussed by Pomraning (1969).
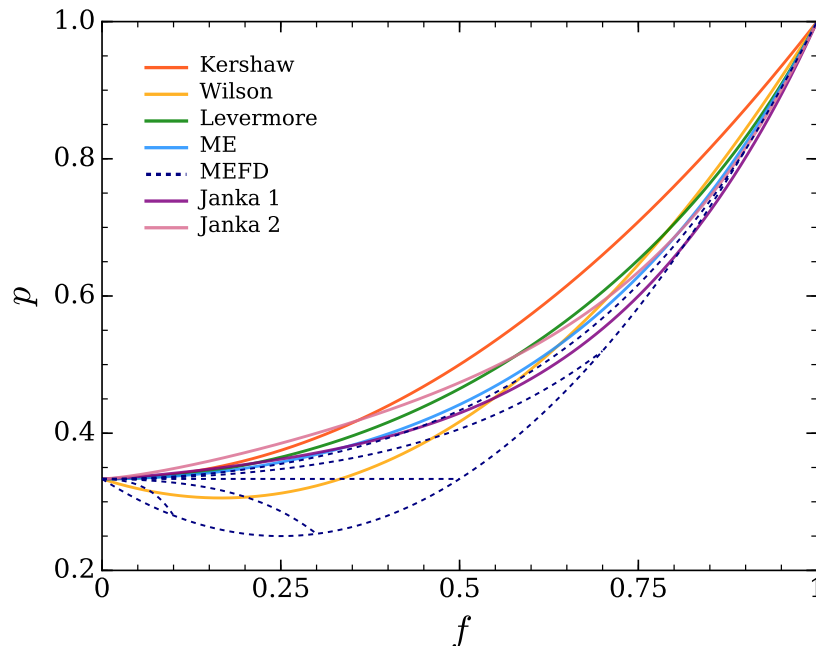
Figure 4.1: The closure relations for the Eddington factor $p = P_\nu^{rr}/E_\nu$ as the function of flux factor $f = F_\nu^r/E_\nu$. The `MEFD` closure is a two parameter function and is represented by series of curves for $e = 0.1,\ 0.2,\ 0.3,\ 0.5,\ 0.7$, and 0.9. The bottom curve is the limit of maximal packing. In the limit $e \to 0$, the `MEFD` closure reduces to its classical limit, the `ME` closure, represented by the solid sky blue line. (see Section 4.3.4).

4.3   Closures

In this section, we present a list of seven different closures most commonly used in the literature and describe their main properties.

4.3.1   Kershaw Closure

The Kershaw (1976) closure is a simple interpolation between the optically thick $(f \to 0)$ and the optically thin $(f \to 1)$ limits. In the spherically symmetric, case the Kershaw closure reads

$$p = \frac{1 + 2f^2}{3}. \tag{4.15}$$

This closure is shown with the solid red line in Fig. 4.1. In the following, we refer to this closure as the `Kershaw` closure.

4.3.2 Wilson Closure

Wilson et al. (1975) and LeBlanc & Wilson (1970) presented a flux-limiter for neutrino diffusion, which corresponds to the closure

$$p = \frac{1}{3} - \frac{1}{3}f + f^2. \tag{4.16}$$

Physically, this expression is equivalent to an interpolation of the diffusive and free-streaming fluxes via harmonic averaging (Smit et al., 2000). This ensures correct diffusive and free-streaming limits, but may yield imprecise results in the intermediate regime. This closure is shown with the solid yellow line in Fig. 4.1. Hereafter, we refer to this closure as the `Wilson` closure.

4.3.3 Levermore Closure

The Levermore closure can be derived assuming that the radiation is isotropic and satisfies the Eddington closure ($P_\nu^{ij} = P_{\mathrm{thick}}^{ij}$ or $p = 1/3$ everywhere) in the "rest frame" of radiation, i.e., in the frame in which the radiation flux is zero (Levermore, 1984; Sądowski et al., 2013):

$$p = \frac{3 + 4f^2}{5 + 2\sqrt{4 - 3f^2}}. \tag{4.17}$$

This closure is shown with the solid green line in Fig. 4.1. We refer to this closure as the `Levermore` closure.

4.3.4 MEFD: Maximum Entropy Closure for Fermionic Radiation

The idea to use the maximum entropy principle to construct the closure relation was first suggested by Minerbo (1978), who applied it to photons assuming a classical distribution. Later, Cernohorsky & Bludman (1994) applied it to fermions using the Fermi-Dirac distribution.

By maximizing the entropy functional

$$S[\mathcal{F}(\mu)] = (1 - \mathcal{F})\log(1 - \mathcal{F}) + \mathcal{F}\log\mathcal{F}, \tag{4.18}$$

under the constraints that the dimensionless zeroth and first moments,

$$e = \frac{E_\nu}{\nu^3} = \int_0^{2\pi} d\phi \int_{-1}^{1} \mathcal{F} \, d\mu, \tag{4.19}$$

$$f = \frac{F_\nu}{E_\nu} = \int_0^{2\pi} d\phi \int_{-1}^{1} \mu \mathcal{F} \, d\mu, \tag{4.20}$$

are given, one can obtain a distribution of radiation in terms of Lagrange multipliers η and a (e.g., Smit et al., 2000):

$$\mathcal{F} = \frac{1}{e^{\eta - a\mu} + 1}, \tag{4.21}$$

where $\mu = \cos\theta$. The second moment of equation (4.21) yields p as a function of η and a. The closure relation is obtained by expressing η and a in terms of e and f through inversion of $e(\eta, a)$ and $f(\eta, a)$:

$$p = \frac{1}{3} + \frac{2}{3}(1 - e)(1 - 2e)\chi\left(\frac{f}{1 - e}\right), \tag{4.22}$$

where $\chi(x) = 1 - 3/q(x)$ and $q(x)$ is the inverse Langevin function $L(q) \equiv \coth q - 1/q$. The lowest-order polynomial approximation to function $\chi(x)$ that has the correct free-streaming and diffusive limits is

$$\chi(x) = x^2(3 - x + 3x^2)/5, \tag{4.23}$$

which is $\sim 2\%$ accurate (Cernohorsky & Bludman, 1994; Smit et al., 2000). The substitution of this approximation into equation (4.22) yields an analytical closure that is a function of both f and e. We refer to this closure as the MEFD closure. It is shown in Fig. 4.1 as a a series of curves for $e = 0.1, 0.3, 0.5, 0.7,$ and 0.9 with dashed lines. Note that, in the limit of maximum packing, the MEFD closure reduces to (e.g., Smit et al., 2000)

$$p = \frac{1}{3}\left(1 - 2f + 4f^2\right). \tag{4.24}$$

This closure, shown with the bottom curve in Fig. 4.1, represents one boundary of the MEFD closure. The other boundary is the classical limit of this closure, the Maximum Entropy (ME) closure, discussed below.

4.3.5 ME: Maximum Entropy Closure in the Classical Limit

The classical limit of the `MEFD` closure is the closure by Minerbo (1978). It can be obtained from equations (4.22)-(4.23) by formally taking the $e \to 0$ limit:

$$p = \frac{1}{3} + \frac{2f^2}{15}(3 - f + 3f^2).$$ (4.25)

This closure is shown with the solid sky blue line in Fig. 4.1. We refer to this closure as the `ME` closure.

4.3.6 Janka Closures

Based on extensive Monte Carlo neutrino transport calculations in PNS envelopes, Janka (1991, 1992) constructed several analytic fits to energy-averaged radiation fields, which were parametrized as

$$p = \frac{1}{3} \left[1 + af^m + (2 - a)f^n\right],$$ (4.26)

where a, n, and m are the fitting parameters. We consider two closures corresponding to sets $\{a = 0.5, b = 1.3064, n = 4.1342\}$ `Janka_1` and $\{a = 1, b = 1.345, n = 5.1717\}$ `Janka_2`. The former is obtained by combining the MC outputs for electron neutrinos from two matter distribution models corresponding to extended hot shocked mantle and compact post bounce configuration. The latter closure is obtained from the ν_μ radiation field of the matter configuration at $300 \, \mathrm{ms}$ after bounce. These two closures are shown in Fig. 4.1 with dark and bright purple colors, respectively.

4.4 Results

In order to asses the quality of M1 results, we consider the radiation field in and around the uniform sphere (Section 4.4.2) and a set of protoneutron star models (Section 4.4.3). The former case has an analytical solution, while the latter is calculated with the MC method using the code of Abdikamalov et al. (2012). Both of these problems have the central opaque region and outer transparent envelope common to many astrophysical sources.

4.4.1 Quantitative Estimate of Accuracy

In order to estimate the accuracy of the M1 results, we use the normalized mean square deviation and the spectrum-weighted mean square deviation. The

former is defined as

$$\delta Y(X) = \sqrt{\frac{1}{N_X} \sum_{X_{\min}}^{X_{\max}} \left[1 - \frac{Y(X_i)}{Y_0(X_i)}\right]^2}. \tag{4.27}$$

Here, Y stands for any quantity we want to compare (e.g., energy density, flux factor, and etc.), while Y_0 is the "exact" value of this quantity obtained from the analytical solution or a Monte Carlo calculation. X is a variable on which both Y and Y_0 depend (e.g., the radial coordinate) and X_i are its discrete values ranging from $X_{\min}$ to $X_{\max}$. Thus, δY provides an estimate of how well the closure solution approximates the exact solution in the entire range from $X_{\min}$ to $X_{\max}$.

The spectrum-weighted mean square deviation is defined as

$$\bar{\delta}Y = \frac{\sum w_i \delta Y_i}{\sum w_i}, \qquad w_i = S_i / S_{\max}, \tag{4.28}$$

where i is the index of the neutrino energy group and δY_i is defined by equation (4.27) for each energy group independently. The spectral weights w_i are obtained using the spectral energy density S_i at energy ε_i and the peak value of spectral energy density $S_{\max}$. In our analysis of the spectral weighted quantities, we restrict ourselves to the energies lying near the spectral peak. More specifically, we consider only the energy groups with spectral energy densities greater than $0.3 S_{\max}$ in order to cut out low statistics energy groups.

4.4.2 Uniform Sphere

The uniform sphere problem consists of a static homogeneous and isothermal sphere of radius R surrounded by vacuum. Matter inside the sphere can absorb and emit radiation. This problem has an analytical solution and possesses important physical and numerical characteristics. The central opaque source with transparent outer regions are characteristics of many astrophysical systems, while the sharp surface represents a serious challenge for many numerical techniques. For this reason, this problem is often used as a test problem for radiation transport codes (O'Connor, 2015; Rampp & Janka, 2002; Schinder & Bludman, 1989; Smit et al., 1997)

The analytical solution for the distribution function is given as

$$\mathcal{F}(r, \mu) = B \left[1 - e^{-\kappa R s(r, \mu)}\right], \tag{4.29}$$
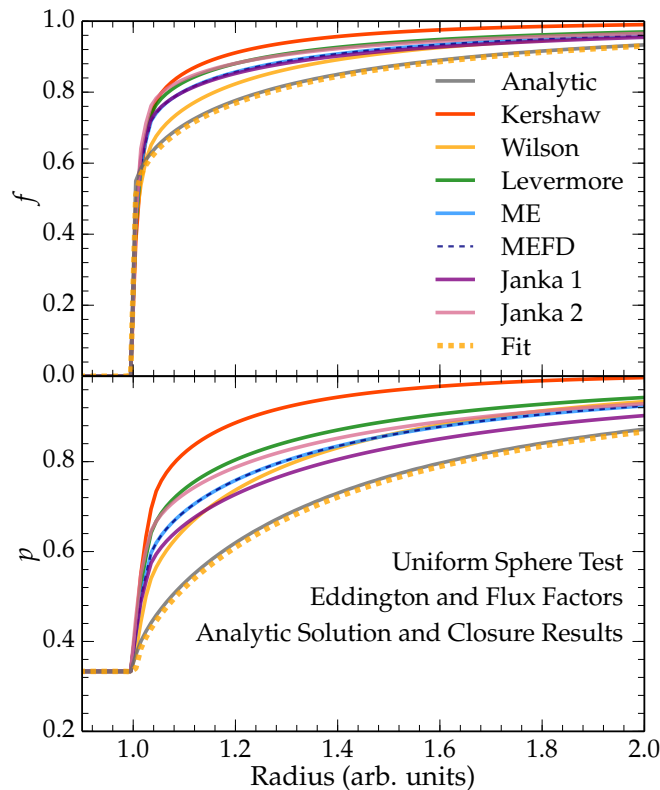
Figure 4.2: The flux factor f and the Eddington factor p as a function of radial coordinate. The matter background is a uniform radiative sphere with $\kappa R = 7500$. The dim gray line is the analytical solution and the colorful lines are the M1 approximations. The performance of the closures is quantitatively evaluated in Table 4.1. The dashed yellow line (Fit) belongs to (4.31), which is the fit to analytical closure obtained from (4.29).
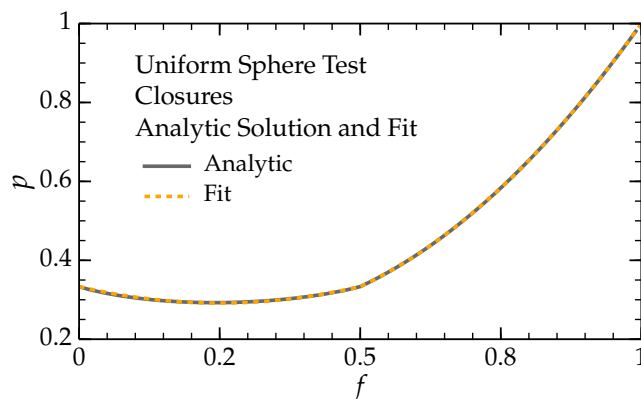
Figure 4.3: The closure reconstructed from the exact solution (4.29) of the uniform radiative sphere problem (solid black line) and analytical fit (4.31) to that solution (dashed yellow line). This closure is noticeably different from the analytical closures shown in Fig. 4.1. This explains why these closures yield poor results for the uniform sphere problem.

Closure prescription	$\delta f_\nu(r)$	$\delta p_\nu(r)$
Kershaw	0.13	0.32
Wilson	0.05	0.14
Levermore	0.10	0.22
ME	0.07	0.17
MEFD	0.07	0.17
Janka_1	0.07	0.13
Janka_2	0.10	0.21
Fit Closure	0.01	0.01

Table 4.1: Mean square deviation of the flux and the Eddington factors obtained with closure prescriptions from the analytical solution for the radiative uniform sphere problem. The sum in the formula for the normalized mean square deviation (4.27) is taken over radii from $r_{min} = 1.0$ to $r_{max} = 2.0$.

where r is the radial coordinate, R is the radius of the sphere, $\mu = \cos\theta$,

$$
s(r, \mu) = \begin{cases} \dfrac{r}{R}\mu + g(r, \mu) & \text{if } r < R, \quad -1 \le \mu \le 1 \\[2ex] 2g(r, \mu) & \text{if } r \ge R, \quad \sqrt{1 - \left(\frac{R}{r}\right)^2} \le \mu \le 1 \\[2ex] 0 & \text{otherwise} \end{cases}
$$

and

$$
g(r, \mu) = \sqrt{1 - \left(\frac{r}{R}\right)^2 (1 - \mu^2)}. \tag{4.30}
$$

Inside the sphere the absorption coefficient κ and emissivity B are constants. Outside the sphere, there is no emission and absorption. For our test, we use $\kappa R = 7500$ and $B = 1$, which ensures that radiation is fully isotropic inside the sphere and a tiny region $\sim 1/\kappa \ll R$ separates it from the free-streaming regime outside the sphere.

The flux factor f (top panel) and the Eddington factor p (bottom panel) as a function of the radial coordinate are shown on Fig. 4.2. The dim gray line represents the analytical solution, while the rest of the lines represent the solutions obtained with M1 approximations. The values of normalized mean square deviations of these solutions from the analytical result are listed in Table 4.1.

As we see, all closures perform poorly for this problem. The `Kershaw` closure yields significantly worse results than the rest of the closures. The normalized mean square deviation of the flux and Eddington factors obtained with closure prescriptions from analytical result are 0.13 and 0.32, respectively (cf. Table 4.1). The next worse performers are the `Levermore` and `Janka_2` closures. The normalized deviations of the Eddington factor are 0.22 and 0.21 for these two closures, respectively. The best performers are the `Wilson` and the `Janka_1` closures, for which the normalized deviations of the Eddington factor are 0.14 and 0.13. The rest of the closures yield intermediate results.

Such a poor result of the analytical closures has a simple explanation. The true closure for this problem, which can be reconstructed directly from the solution (4.29), is shown with a solid black line in Fig. 4.3. This closure is significantly different from all the aforementioned closures, as we can glean by comparing Fig. 4.3 with Fig. 4.2. Therefore, the reason why our closures yield inaccurate results is simply because these closures are different from the true closure for this problem.

Interestingly, the true closure in Fig. 4.3 can be fit well with the following simple analytical expression

$$p = \begin{cases} 1/3 - 1/3f + 2/3f^2, & f \leq 1/2, \\ 1/3 - 2/3f + 4/3f^2, & f > 1/2, \end{cases} \tag{4.31}$$

which is shown with the orange dashed line in Fig. 4.3. If we perform M1 calculations with this closure, it reproduces the analytical result (4.29) with excellent $\sim 1\%$ accuracy (cf. Table 4.1). Note that this fit closure is not expected to perform well for any other matter distributions except the uniform sphere. It is specific to this particular model problem.

4.4.3 Protoneutron Star

In this section, we evaluate the ability of the M1 closures to model the neutrino radiation field around spherically symmetric models of protoneutron stars (PNSs) formed in core-collapse supernovae. We take three different post-bounce configurations (obtained from 2D radiation-hydrodynamics simulations of Ott et al. 2008) of a $20M_\odot$ progenitor star at 160 ms, 260 ms, and 360 ms after bounce. We average the 2D profiles of Ott et al. (2008) over angle to obtain spherically symmetric configurations of PNSs. The radial profiles of density, temperature, and electron fraction are shown in the upper, center,
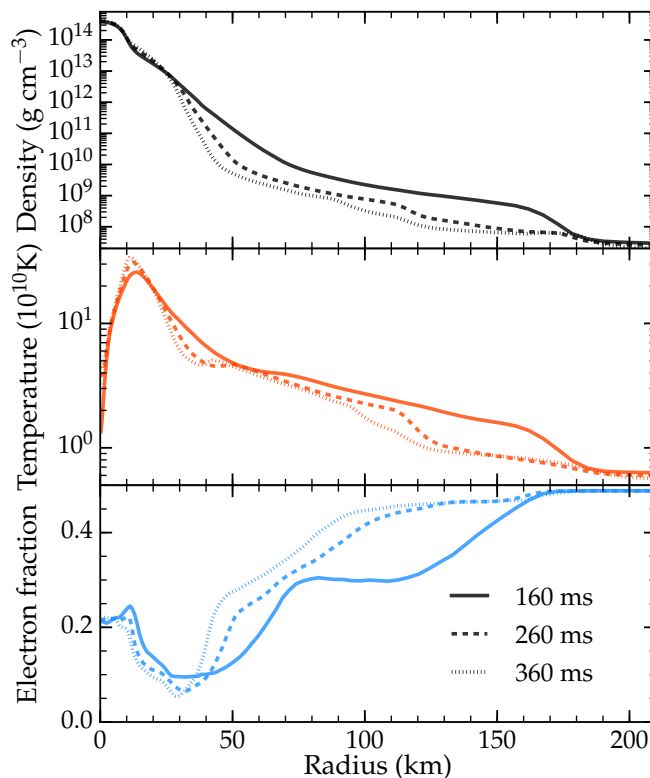
Figure 4.4: The radial profiles of density (upper panel), temperature (center panel), and electron fraction (bottom panel) for protoneutron star models of Ott et al. (2008) at 160 ms (solid line), 260 ms (dashed line), and 360 ms (dash-dotted line) after bounce. The radial profiles are obtained by angular averaging the 2D data of Ott et al. (2008).

and bottom panels of Fig. 4.4. The spectra of neutrino luminosity obtained from MC code at the radius of $100\,\mathrm{km}$ are shown in Fig. 4.5. The top, center, and bottom panels represent the PNS models at 160, 260, and 360 ms after bounce, respectively.

The "exact" solution of the problem is obtained from MC calculations using the code of Abdikamalov et al. (2012), while the M1 results are obtained using the GR1D code (O'Connor, 2015). We evolve our time dependent MC code until we reach steady-state neutrino radiation field for each model of PNS. This field is then averaged over many timesteps until we get rid of the stochasticity in the MC solution. Since the MC method does not use any approximations in the solution procedure (Abdikamalov et al., 2012), the solution obtained this way is exact for a given configuration of matter (i.e., a given configuration of opacities and emissivities). In order to ensure the consistency of the results,
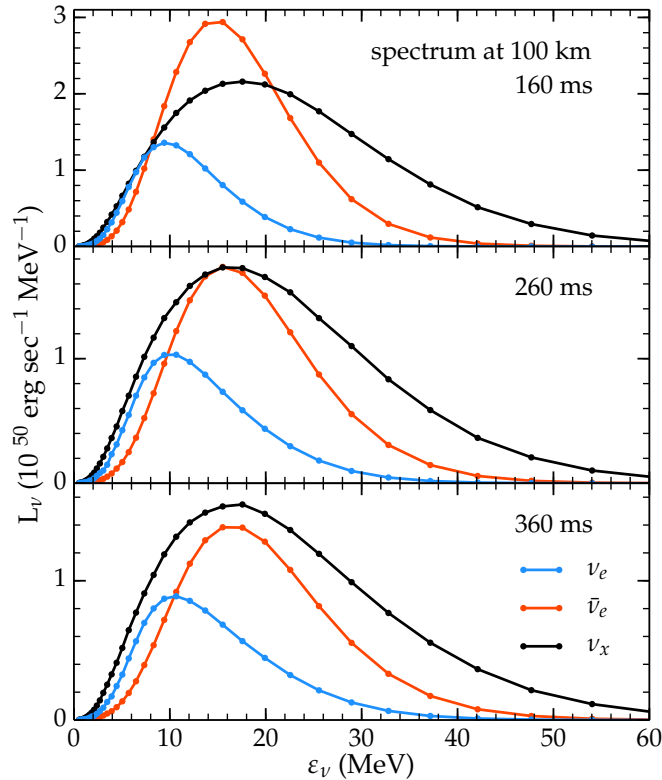
Figure 4.5: The spectra of neutrino luminosity measured at a radius of $100\,\mathrm{km}$ obtained from MC code. The **t**op, **c**enter, and **b**ottom panels represent the PNS models of Ott et al. (2008) at 160, 260, and 360 ms after bounce, respectively.

the two codes use identical microphysical inputs. Both use the Shen et al. (1998) equation of state (EOS) table and a `NuLib` opacity table (O'Connor, 2015) that was generated with the same EOS table. In both codes, we use 48 logarithmic energy groups ranging from $0.5\,\mathrm{MeV}$ to $200\,\mathrm{MeV}$. In the MC code, we use 150 radial logarithmically spaced zones with the central resolution of $0.2\,\mathrm{km}$. We have performed extensive resolution tests in order to ensure that our results are convergent.

We examine the quality of the closures in the free streaming, semi-transparent, and opaque regimes. We separate these regimes based on the value of the flux factor f. We choose the transparent regime as the one where $0.9 < f < 1$, the semi-transparent as $0.5 \leq f \leq 0.9$ and the opaque as $0.2 \leq f \leq 0.5$. We neglect the region of low f because the MC results suffer from noise in the highly diffusive region. It is more appropriate to separate the different regimes based on f rather than, e.g., the value of the radial coordinate, because at a
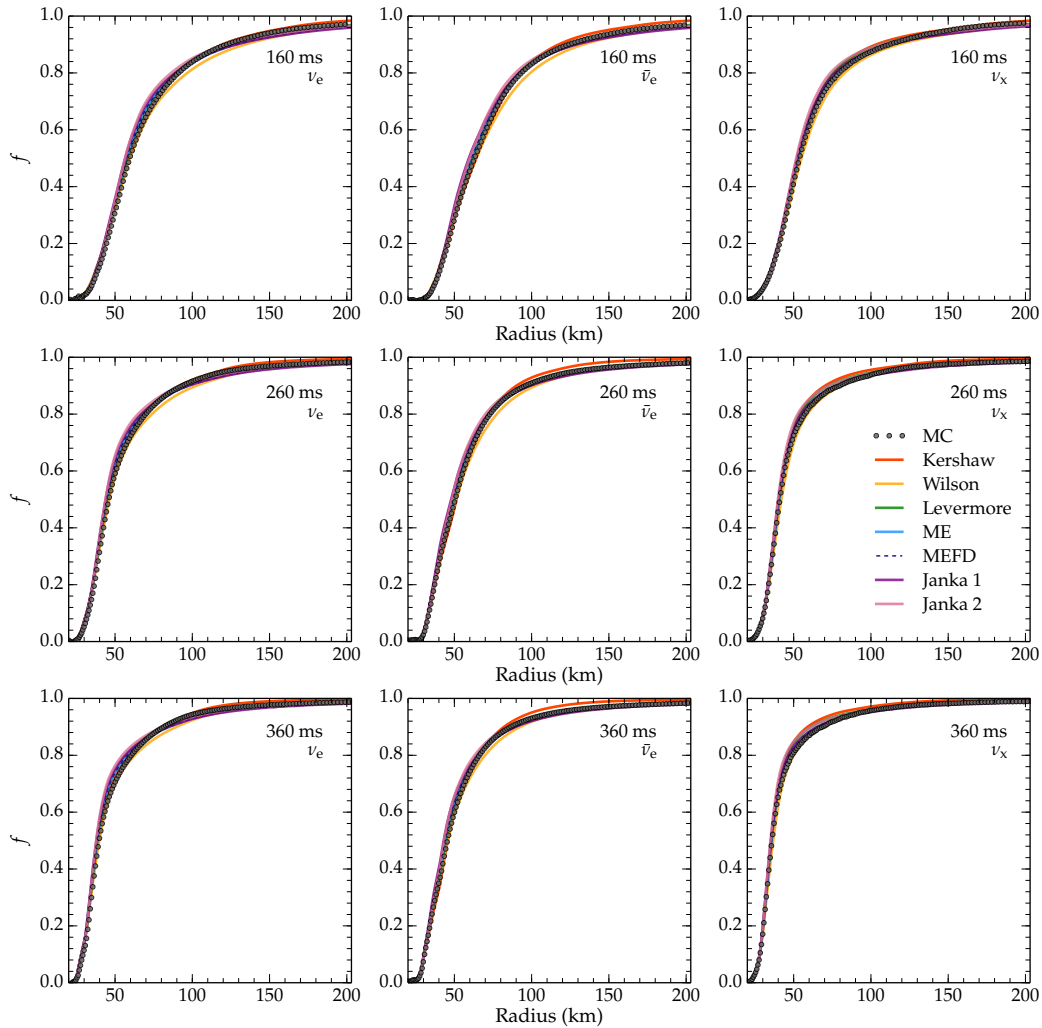
Figure 4.6: The radial profiles of the flux factor f obtained using the seven closures and from the Monte Carlo code (dotted line) for three different types neutrinos and three PNS configurations at 160, 260, and 360 ms after bounce. All quantities are measured at the neutrino energy groups corresponding to the peak luminosity at $100\,\mathrm{km}$ for each neutrino type. The spectra of neutrino luminosities at this radius are shown in Fig. 4.5 for each neutrino type and three PNS models.
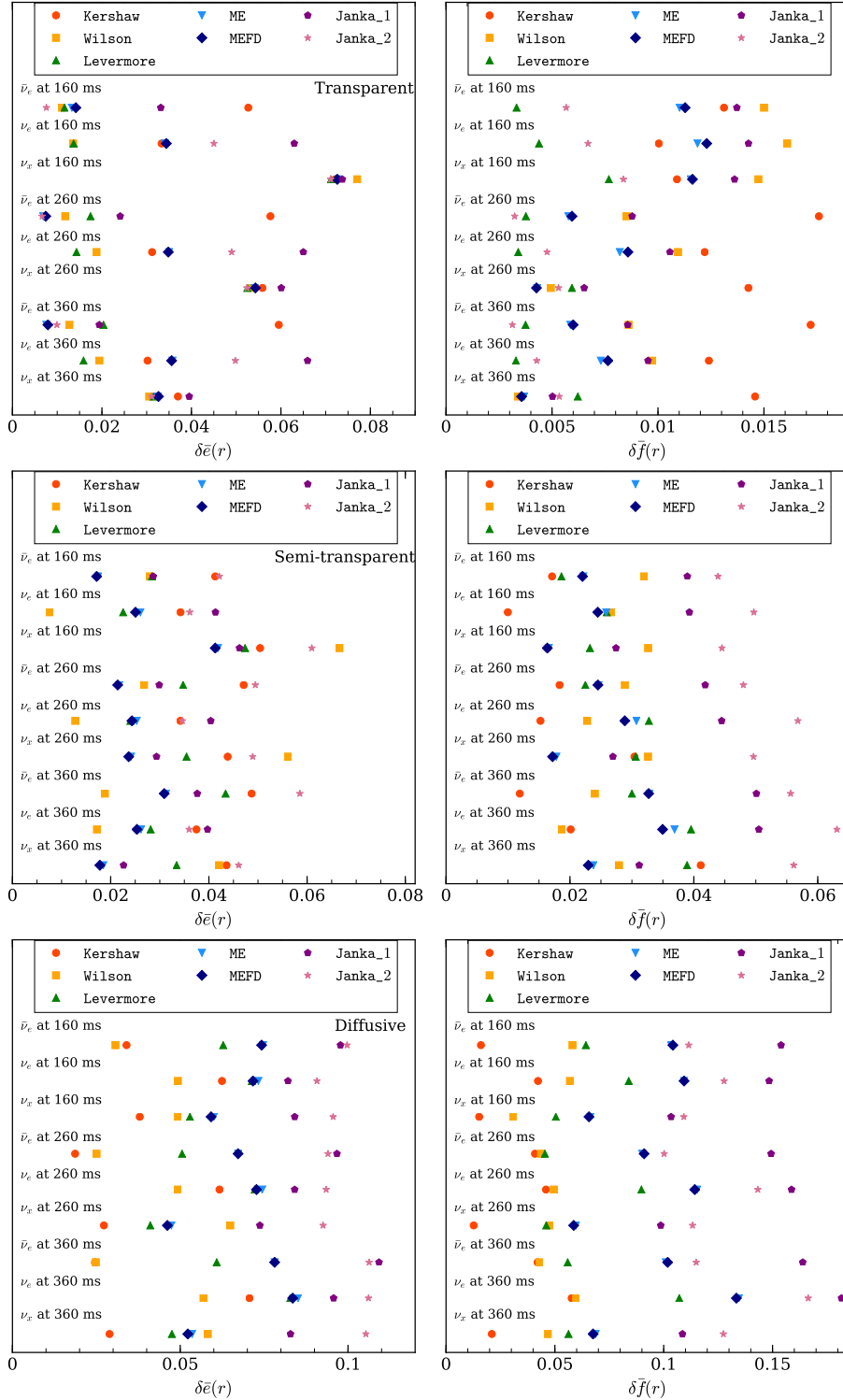
Figure 4.7: The spectrum-weighed mean square deviation of energy density e (left panel) and the flux factor f (right panel) for different neutrino types for PNS models at 160, 260, and 360 ms after bounce. The top, center, and bottom panels represent the transparent ($0.9 \leq f \leq 1$), semi-transparent ($0.5 \leq f \leq 0.9$), and diffusive ($0.2 \leq f \leq 0.5$) regimes, respectively.

given radius, neutrinos of different energies behave differently. For example, low-energy neutrinos have lower opacity and hence they propagate more freely compared to higher-energy neutrinos at the same radius.

The radial profiles of the flux factor f obtained using the seven closures and from the Monte Carlo code (dotted line) for three different types of neutrinos and three PNS configurations at 160, 260, and 360 ms after bounce are shown in Fig. 4.6. All flux factors are measured at the neutrino energy groups corresponding to the peak luminosity at $100\,\mathrm{km}$ for each neutrino type (cf. Fig. 4.5). As we can see, all M1 closures yield qualitatively correct results.

For a more precise quantitative estimate, we utilize the spectrum-weighed deviations of the flux factor and energy density from the MC results, equation 4.28. The spectrum-weighted deviation $\bar{\delta}e$ of the energy density e in the transparent regime for the seven different closures, for the three neutrino types, and the PNS models at 160, 260, and 360 ms are shown on the top left panel of Fig. 4.7. The deviations $\bar{\delta}e$ are calculated using formula (4.28), in which the spectrum is taken at $100\,\mathrm{km}$. In order to verify that our results are not too dependent on spectral information at different locations, we have calculated $\bar{\delta}e$ using spectra at several different radii and obtain results very similar to $\bar{\delta}e$ that use spectra at $100\,\mathrm{km}$. This suggests that the values of $\bar{\delta}e$ presented in Fig. 4.7 are robust measures of errors of the M1 closures for the radiation field around PNSs.

As we can see, different closures yield different levels of accuracy depending on the neutrino type and PNS model. No single closure performs consistently better (or worse) than other closures in all cases. That said, the `Wilson` and the `Levermore` closures perform better than others in most cases in the transparent regime, followed by the `ME` and `MEFD` closures. The `Janka_1` and the `Janka_2` closures exhibit $\bar{\delta}e \gtrsim 0.04$ in most cases, which is worse than $\bar{\delta}e$ for the rest of the closures. This is a remarkable result because the `Janka_1` and `Janka_2` closures were constructed from fitting to the exact solution for the neutrino radiation field around PNS. This demonstrates that a closure constructed for one PNS model (with a given EOS and opacity table) does not necessarily yield a good result for all other PNS models.

The behavior of the deviation of the flux factor $\bar{\delta}f$ is shown on the top right panel of Fig. 4.7. In this case, the `Levermore` closure performs better than other closures in almost all cases and yields small $\bar{\delta}f \sim 0.004$. The `Janka_2` closure performs only slightly worse than this closure, yielding $0.004 \lesssim \bar{\delta}f \lesssim$

0.009. However, this is $\sim 2-3$ times smaller than what the rest of the closures yield, which is a surprising result because the `Janka_2` closure yields relatively poor result for the energy density compared to most of the closures, as we discussed in the previous paragraph.

The `Kershaw` closure produces the least accurate f compared to the other closures in all models except the PNS models at $160\,\text{ms}$ after bounce, yielding deviations of $\bar{\delta}f \sim 0.015$ in all cases. The `Wilson` closure yields intermediate results in most situations except for the PNS model at 160 ms after bounce, for which it yields the largest deviation of $\bar{\delta}f \sim 0.015$. This again shows that a closure that yields the best result for the energy density does not necessarily yield the best result for the flux factor. As we see below, the reverse of this statement is also true.

The spectrum-weighed deviations $\bar{\delta}e$ and $\bar{\delta}f$ for the semi-transparent regime are shown in the left and right center panels of Fig. 4.7, respectively. In this regime, both the `ME` and `MEFD` closures often – but not always – yield the smallest deviations $\bar{\delta}e$. The `Janka_1` and `Janka_2` closures yield the largest $\bar{\delta}f$ of $\sim 0.04-0.06$ in all cases. The `Wilson` closure yields the smallest $\bar{\delta}e$ in most cases, but produces $\bar{\delta}f \sim 0.03$, which is roughly the mean of the values of $\bar{\delta}f$ produced by all of the closures. On the other hand, the `Kershaw` closure yields the smallest $\bar{\delta}f$ of $\sim 0.01-0.02$ in most cases, but yield relatively large $\bar{\delta}e$ of $\sim 0.035-0.05$.

In the opaque region, the situation is significantly different. The `Kershaw` closure, which often yields the largest $\bar{\delta}e$ and $\bar{\delta}f$ in the transparent and $\bar{\delta}e$ in the semi-transparent regimes, produces the smallest $\bar{\delta}e$ and $\bar{\delta}f$ of $\lesssim 0.05$ in the opaque regime. The `Wilson` closure yields slightly worse results than the `Kershaw` closure with $\bar{\delta}e \sim \bar{\delta}f \sim 0.05$. The `Janka_1` and `Janka_2` closures yield the largest errors ($\bar{\delta}e \sim 0.1$ and $\bar{\delta}f \sim 0.1-0.15$). This again shows that a closure that yields good results for one model of PNS does not necessarily produce good results for other PNS models.

In all cases, the `ME` and `MEFD` maximum entropy closures yield almost identical results. This is direct consequence of the fact the former closure is the classical limit of the latter and the radiation field, in the regions we considered, is predominately in the classical regime.

Overall, these two closures yield relatively good results in all cases and never result in the largest deviations compared to the other closures. This, in combination with the fact that the `ME` closure is simpler and requires fewer operations
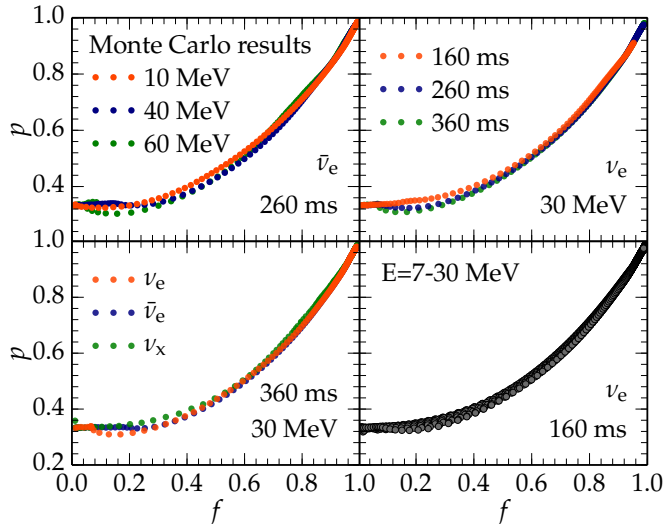
Figure 4.8: The closure relations obtained from Monte Carlo results as the function of the neutrino type (top left), the neutrino energy (top right), and the background matter distribution (bottom left). The bottom right shows the variation in the closures as a function of neutrino energy. Here, twelve groups are plotted together.

to compute than the `MEFD` closure, makes the former a more attractive option for neutrino transport applications involving protoneutron stars.

These results demonstrate that no single closure performs the best or the worst in all cases. Whether a specific closure is "correct" for a given problem depends on the parameters of the problem, such as the matter configuration (i.e., profiles of density, temperature, and composition) and the neutrino type. We find a similar level of differences between deviations of e and f for different neutrino energy groups (not shown here). Fig. 4.8 shows the functional form of the closures $p(f)$ extracted from the MC simulations for different neutrino types, different PNS models and different energy groups. We can clearly see variations between closures $p(f)$ corresponding to different problems.

4.5   Conclusion

We conducted a systematic, quantitative study of the accuracy of analytical closure relations for two-moment neutrino radiation transport schemes commonly used in the literature. We considered the neutrino field around two sets of radiating objects: the uniform radiative sphere and PNS models at 160, 260, and 360 ms after core bounce obtained from simulations of Ott et al. (2008). In all cases, the matter configuration is assumed to be static. This restriction al-

lows us to focus on the quality of the closure relations and exclude other sources of errors such as those stemming from non-linear radiation-matter coupling.

We considered seven different closures. These are the closures by Kershaw (1976), Wilson et al. (1975), Levermore (1984), and the maximum entropy closures of Cernohorsky & Bludman (1994) and Minerbo (1978). In addition, we considered two closures that are constructed by fitting to exact Monte Carlo solutions of the radiation field around PNSs by Janka (1991).

We find that no single closure, among those studied here, is consistently better or worse than any other. A closure that yields accurate results in one case may not yield as good results in other situations. The level of accuracy that a given closure yields varies for different quantities.

Given this limitation of the closures, the maximum entropy closure by Minerbo (1978) and Cernohorsky & Bludman (1994), which yield almost identical results, often yield better results among all the closures studied. These two closures never yielded the worst results compared to all other closures. In this sense, these two are a safe choice, as they are less likely to yield extremely erroneous result over a wide range of problems and variables. Since the Minerbo (1978) closure is simpler to compute than the one by Cernohorsky & Bludman (1994), we conclude that the former closure is the most attractive choice for problems involving neutrino transport around PNSs.

In this work, we assumed spherical symmetry, static matter, and flat spacetime. These assumptions limit the scope of the implications of our results. In particular, the hydrodynamic and general relativistic effects introduce shifts in the energy spectrum of neutrinos, which alter the moment equations (e.g, Cardall et al., 2013; Just et al., 2015). Also, in non-spherically-symmetric cases, we can have radiation sources at different spatial locations. Notable examples are the accretion disks formed in neutron star mergers and hot spots near the PNS surfaces in the context of core-collapse supernovae. The interaction of radiation beams from such sources cannot be modeled within our spherically-symmetric setup. It is *a priori* unclear the extent to which our results are valid in such cases. This will be the subject of a future study.

Acknowledgements

4.6 Appendix: Methods

4.6.1 The GR1D Radiation-Hydrodynamics Code

We employ the M1 radiation transport solver that is part of the GR1D radiation-hydrodynamics Code (O'Connor, 2015; O'Connor & Ott, 2011, 2013) available at http://www.GR1Dcode.org. The matter in our calculations is static and the metric is Minkowski. There is no coupling between different energy groups. For these conditions, GR1D implements M1 closures by setting the pressure tensor according to equation (4.10). Under these conditions, the transport equations read

$$\partial_t E_\nu + \frac{1}{r^2}\partial_r r^2 F_\nu^r = \eta_\nu - \kappa_{\nu,a} E_\nu, \tag{4.32}$$

$$\partial_t F_\nu^r + \frac{1}{r^2}\partial_r r^2 P_\nu^{rr} = -(\kappa_{\nu,a} + \kappa_{\nu,s})F_\nu^r +$$

$$E_\nu \frac{1-p}{r}, \tag{4.33}$$

where η_ν, $\kappa_{\nu,a}$, and $\kappa_{\nu,s}$ are the neutrino emissivity, absorption opacity, and scattering opacity, respectively. To numerically solve these equations we discretize the neutrino spectrum into 48 energy groups, logarithmically spaced between 0.5 MeV and 180 MeV. For each energy group and species, we compute the closure ($p = P_\nu^{rr}/E$), the spatial flux terms ($\partial_r r^2 F_\nu^r$ and $\partial_r r^2 P_\nu^{rr}$), and the values of the neutrino interaction coefficients (η_ν, $\kappa_{\nu,a}$, and $\kappa_{\nu,s}$) explicitly at the beginning of the time step (denoted via the index (n)). We then use a first order, implicit/explicit time integration method to solve for the values of the energy and momentum density at time $t + \Delta t$ (or the $(n + 1)$ time step),

$$E_\nu^{(n+1)} = [E_\nu^{(n)} - \Delta t(\partial_r(r^2 F_\nu^{r,(n)})/r^2 + \eta_\nu)] \times$$

$$1/(1 + \kappa_{\nu,a}\Delta t), \tag{4.34}$$

$$F_\nu^{r,(n+1)} = \{F_\nu^{r,(n)} - \Delta t[\partial_r(r^2 P_\nu^{rr,(n)})/r^2 +$$

$$E_\nu^{(n+1)}(1 - p_\nu^{(n)})/r]\}/[1 + (\kappa_{\nu,a} + \kappa_{\nu,s})\Delta t]. \tag{4.35}$$

The explicit calculation of the spatial flux remains valid in the diffusion limit due to corrections applied to the Riemann solution in high optical depth re-

gions (O'Connor, 2015). The neutrino interaction coefficients are computed using `NuLib`, an open-source neutrino interaction library available at http://www.nulib.org (O'Connor, 2015). For PNS calculations, we include elastic scattering of neutrinos on nucleons, and coherent elastic scattering on alpha particles and heavy nuclei as contributions to $\kappa_{\nu,s}$. Charged current absorption of electron neutrinos on neutrons and heavy nuclei and electron antineutrinos on protons is included in $\kappa_{\nu,a}$ and in η_ν via Kirchhoff's law. For heavy lepton neutrinos we determine the emissivity η_ν from pair processes (electron-positron annihilation and nucleon-nucleon Bremsstrahlung) and an effective absorption opacity via an approximation that works well for supernova conditions (O'Connor, 2015).

4.6.2   The Monte-Carlo Neutrino Transport Code

In order to asses the quality of the M1 closures, we compare the M1 results to Monte Carlo radiation transport calculations using the code of Abdikamalov et al. (2012). Here, we outline some salient aspects of such methods, while more in-depth discussion can be found in Abdikamalov et al. (2012).

Monte Carlo methods have been used for many applications (e.g., Burrows & van Riper, 1995; Densmore et al., 2007; Dolence et al., 2009; Janka, 1991, 1992; Janka & Hillebrandt, 1989; Kasen et al., 2006; Keil et al., 2003; Lucy, 2005; Richers et al., 2015; Wolf et al., 1999; Wollaeger et al., 2013). Such methods use sequences of pseudo-random numbers to simulate the transport of radiation using the concept of Monte Carlo particles. Each MC particle represents a group of physical particles with a given location, direction, and energy (or frequency). The number of physical radiation particles (i.e., photons or neutrinos) represented by a MC particle is called the weight of the MC particle. The smaller the weight, the larger the number of MC particles that are needed to model a given problem, which means higher precision at the price of higher computational cost.

The spatial problem domain is divided into a number of interconnected cells, and matter in each cell has its own temperature, density, and composition. Using this information, one calculates the number of MC particles that has to be emitted in each cell within a timestep. These particles are then randomly placed in each cell by randomly sampling their coordinates. The propagation direction is sampled randomly with isotropic distribution. The frequencies/energies of particles are chosen using the form of the energy-dependence of the emissivity function.

Once the MC particles are placed in each cell, they are then transported within a timestep. This can be achieved by calculating three distances for each particle: the distance to collision (absorption or scattering), the distance to the boundary of its cell, and the distance the particle would travel until the end of timestep if it were to travel freely (i.e., assuming that no collision happens). What happens to a particle depends on which of these distances is the smallest. If the distance to collision is the smallest, then the particle is either absorbed or moved to its new location and scattered. The probabilities of absorption and scattering are proportional to their relative opacities. If the distance to a cell boundary is the smallest, then the particle is moved to the boundary of the next cell and transported further in the new cell by calculating a new set of three distances. If the particle crosses the outer boundary of the computational domain, it is removed from the system. Finally, if the third distance is the smallest, then the particle moves by that distance within its cell. Once this step is accomplished for all of the MC particles, the remaining particles, i.e., the ones that have not been absorbed or left the domain, are stored in memory as a preparation for the next timestep. At the next timestep, the cells are populated with newly emitted MC particles, which together with the MC particles remaining from the previous step are then transported further within the second timestep. Subsequent timesteps are performed in the same manner until the end of the simulation.

Chapter 5

THERMAL CHIRAL VORTICAL AND MAGNETIC WAVES: NEW EXCITATION MODES IN CHIRAL FLUIDS

In certain circumstances, chiral (parity-violating) medium can be described hydrodynamically as a chiral fluid with microscopic quantum anomalies. Possible examples of such systems include strongly coupled quark-gluon plasma, liquid helium ^{3}He-A, neutron stars and the Early Universe. We study first-order hydrodynamics of a chiral fluid on a vortex background and in an external magnetic field. We show that there are two previously undiscovered modes describing heat waves propagating along the vortex and magnetic field. We call them the Thermal Chiral Vortical Wave and Thermal Chiral Magnetic Wave. We also identify known gapless excitations of density (chiral vortical and chiral magnetic waves) and transverse velocity (chiral Alfvén wave). We demonstrate that the velocity of the chiral vortical wave is zero, when the full hydrodynamic framework is applied, and hence the wave is absent and the excitation reduces to the charge diffusion mode. We also comment on the frame-dependent contributions to the obtained propagation velocities.

5.1 Introduction

Understanding of the transport phenomena in chiral systems progressed a lot in recent years. It was mainly driven by the realization that microscopic quantum anomalies (such as the axial and mixed gauge-gravitational anomalies) can lead to macroscopic effects (Erdmenger et al., 2009; Isachenkov & Sadofyev, 2011; Neiman & Oz, 2011; Son & Surówka, 2009), such as generation of unusual electric or axial currents and propagating excitations in rotating samples as well as in external electromagnetic fields. Interestingly, such phenomena are potentially observable in a wide span of physical situations, in, e.g., the Weyl/Dirac semimetals, strongly coupled quark-gluon plasma, in cold gases, superfluids and neutron stars; see Refs. (Kharzeev, 2015; Miransky & Shovkovy, 2015) for a review. Hydrodynamics is a natural and widely used approach for the studies of anomalous dynamics in such many-body systems (Zakharov, 2013). The anomaly-driven effects appear already at the first order of derivative expansion.

In this note we study first-order relativistic hydrodynamics with a single $U(1)$

charge and $U(1)^3$ triangle anomaly, in a background of a single vortex or external magnetic field. The hydrodynamic equations in their general form read

$$\partial_\mu T^{\mu\nu} = F^{\nu\alpha} J_\alpha, \qquad \partial_\mu J^\mu = C\, E^\alpha B_\alpha, \tag{5.1}$$

where $T^{\mu\nu}$ is the energy-momentum tensor, J_μ is the current, $E^\mu = F^{\mu\nu} u_\nu$ and $B^\mu = \frac{1}{2}\epsilon^{\mu\nu\alpha\beta} u_\nu F_{\alpha\beta}$ are the electric and magnetic fields in the fluid rest frame, u^μ is the fluid four-velocity, and C is the axial anomaly coefficient. The choice of a single $U(1)$ is due to simplicity, and the generalization for several charges is straightforward. In what follows, we will identify new propagating excitations, namely thermal chiral vortical and magnetic waves. Even though there were many instances when the vortical and magnetic waves were mentioned in the literature (see Ref. (Chernodub, 2016) and references therein), to our knowledge, there was no systematic study made in the hydrodynamic framework. The goal of our paper is to fill this gap and to identify the anomalous propagating modes.

5.2 Chiral vortical wave

In the absence of electromagnetic fields, the dynamics of a fluid is governed by the conservation laws

$$\partial_\mu T^{\mu\nu} = 0, \qquad \partial_\mu J^\mu = 0. \tag{5.2}$$

The velocity of the fluid in its own rest frame is $u^\mu = (1, 0, 0, 0)$ and, in general, $u^\mu = (1 - v^2)^{-1/2}(1, v)$. We choose the Minkowski metric $\eta^{\mu\nu} = \text{diag}(-1, 1, 1, 1)$ so $u^2 = -1$ and the transverse projector is defined as $\Delta^{\mu\nu} \equiv \eta^{\mu\nu} + u^\mu u^\nu$. In what follows we perform the calculations in the Landau frame (projections of first order terms in $T^{\mu\nu}$ and J^μ on u^μ vanish). This choice is due to the fact that we consider the case of zero average charge density, which is ill-defined in the Eckart frame. Constitutive relations for the chiral fluid are the standard constitutive relations for ordinary fluid, but with an additional vortical term in the current (Son & Surówka, 2009),

$$T^{\mu\nu} = \varepsilon u^\mu u^\nu + p\Delta^{\mu\nu} - \eta \Delta^{\mu\alpha}\Delta^{\nu\beta}$$
$$\times \left(\partial_\alpha u_\beta + \partial_\beta u_\alpha - \frac{2}{3}\eta_{\alpha\beta}\partial_\lambda u^\lambda \right) - \zeta \Delta^{\mu\nu}\partial_\lambda u^\lambda, \tag{5.3}$$

$$J^\mu = n u^\mu - \sigma T \Delta^{\mu\nu}\partial_\nu(\mu/T) + \xi\, \omega^\mu, \tag{5.4}$$

where n is the charge density, μ is the chemical potential, σ is the conductivity, $\omega^\mu \equiv \frac{1}{2}\epsilon^{\mu\nu\alpha\beta}u_\nu\partial_\alpha u_\beta$ is vorticity and ξ is the chiral vortical coefficient (Neiman & Oz, 2011)

$$\xi = c_T T^2 \left(1 - \frac{2\mu n}{\varepsilon + p}\right) + C\mu^2 \left(1 - \frac{2}{3}\frac{\mu n}{\varepsilon + p}\right). \tag{5.5}$$

The second term in ξ is uniquely fixed by the requirement on the entropy current s^μ to satisfy $\partial_\mu s^\mu \geq 0$, see (Son & Surówka, 2009). The prefactor for T^2 in the first term cannot be derived from hydrodynamics only (Neiman & Oz, 2011) and is a manifestation of additional microscopic properties of the chiral degrees of freedom (Kalaydzhyan, 2014). In a wide class of physical situations it is defined by the mixed gauge-gravitational anomaly (Jensen et al., 2013; Landsteiner et al., 2011; Volovik, 2006). In the simplest case, when the chirality is carried by non-interacting massless fermions of one chirality, flavor and color, $c_T = 1/6$ and $C = 1/(2\pi^2)$ (Vilenkin, 1979).

Linearization of equations (5.2) around equilibrium leads to vortical term dropping out, as a higher order correction, and recovery of the purely ordinary fluid dynamic equations studied in the literature (Minami & Kunihiro, 2009). In order to preserve the vortical term, we consider a vortex background given by the following velocity profile:

$$u_v^\mu = \left(1, -\epsilon^{ijk}x_j\Omega_k\right) \equiv (1, \boldsymbol{v}_v). \tag{5.6}$$

This corresponds to a constant external $\boldsymbol{\omega} = \boldsymbol{\Omega}$. It is important to emphasize that the rotation is driven by an external force and the velocity profile (5.6) is time-independent. In order to avoid relativistic corrections in u^μ coming from background rotation motion, we assume $R \ll 1/\Omega$, where R is the vortex radius (or a distance to the vortex center) and $\Omega = |\boldsymbol{\Omega}|$. The same will allow us to neglect contributions with $\omega^0 = \boldsymbol{v}\cdot(\boldsymbol{\nabla}\times\boldsymbol{v})/2$ and its variations. Consider now fluctuations on top of this background,

$$\varepsilon = \bar{\varepsilon} + \delta\varepsilon,\ p = \bar{p} + \delta p,\ u^\mu = u_v^\mu + \delta u^\mu,\ \delta u^\mu = (0, \delta\boldsymbol{v}),$$
$$n = \bar{n} + \delta n,\ \mu = \bar{\mu} + \delta\mu,\ T = \bar{T} + \delta T,\ s = \bar{s} + \delta s. \tag{5.7}$$

We can treat the background values as constants, because the leading variations of the thermodynamic parameters due to the external rotation are at

least quadratic in $\boldsymbol{\Omega}$ [1], e.g., $\Delta\bar{\varepsilon}/\bar{\varepsilon} \sim (\Omega R)^2 \ll 1$. At the same time, we allow the variations of the velocity $\delta\boldsymbol{v}$ to be the same order as the velocity $\boldsymbol{v}$, so they play the same role in the power counting. Substituting the variations into the conservations laws (5.2), we get

$$\partial_t \delta\varepsilon + \bar{w}\boldsymbol{\nabla} \cdot \delta\boldsymbol{v} = 0, \tag{5.8}$$

$$\bar{w}\partial_t \delta\boldsymbol{v} = -\boldsymbol{\nabla}\delta p + \eta\nabla^2\delta\boldsymbol{v} + (\zeta + \eta/3)\boldsymbol{\nabla}(\boldsymbol{\nabla} \cdot \delta\boldsymbol{v}), \tag{5.9}$$

$$\partial_t \delta n + \bar{n}\boldsymbol{\nabla} \cdot \delta\boldsymbol{v} - \sigma T \partial_\mu \Delta^{\mu\nu}\partial_\nu(\mu/T)$$
$$+ 2c_T\bar{T}\left(1 - \frac{2\bar{\mu}\bar{n}}{\bar{w}}\right)\boldsymbol{\Omega} \cdot \boldsymbol{\nabla}\delta T + 2C\bar{\mu}\boldsymbol{\Omega} \cdot \boldsymbol{\nabla}\delta\mu$$
$$- \frac{2c_T\bar{T}^2\bar{\mu}\bar{n}}{\bar{w}^2}\boldsymbol{\Omega} \cdot \boldsymbol{\nabla}\left(\frac{\bar{w}}{\bar{\mu}}\delta\mu + \frac{\bar{w}}{\bar{n}}\delta n - \delta\varepsilon - \delta p\right)$$
$$- \frac{2C\bar{\mu}^3\bar{n}}{3\bar{w}^2}\boldsymbol{\Omega} \cdot \boldsymbol{\nabla}\left(\frac{3\bar{w}}{\bar{\mu}}\delta\mu + \frac{\bar{w}}{\bar{n}}\delta n - \delta\varepsilon - \delta p\right) = 0, \tag{5.10}$$

where $\bar{w} \equiv \bar{\varepsilon} + \bar{p}$ is the enthalpy density. Here we also used the identity $\boldsymbol{\nabla} \cdot \boldsymbol{v}_{\mathrm{v}} = 0$ and dropped $\boldsymbol{v} \cdot \boldsymbol{\nabla}\delta X$ terms.

Let us now perform the Fourier transform of the hydrodynamic equations with the following convention

$$\Phi(t, \boldsymbol{r}) = \int_{-\infty}^{\infty} d\omega \int_{-\infty}^{\infty} d\boldsymbol{k}\, e^{-i\omega t + i\boldsymbol{k}\cdot\boldsymbol{r}}\, \Phi(\omega, \boldsymbol{k})\,. \tag{5.11}$$

Note that $\boldsymbol{\Omega}$ enters equations in a scalar product with $\boldsymbol{k}$, and, therefore, components of $\boldsymbol{k}$ perpendicular to $\boldsymbol{\Omega}$ do not contribute to anomalous terms. Therefore, to make the contribution of the anomaly more pronounced and for the additional simplicity, we assume that the wave-vector $\boldsymbol{k}$ is oriented along $\boldsymbol{\Omega}$. For some of the effects related to the general orientation $\boldsymbol{k}$, see Ref. (Abbasi et al., 2016). We further decompose $\boldsymbol{v} = \boldsymbol{v}_\parallel + \boldsymbol{v}_\perp$ into a sum of components parallel and transverse to $\boldsymbol{k}$, respectively. After that the system of equations

---

[1] Odd powers of Ω would lead to the change of sign with the change in rotation direction

(5.8)-(5.10) becomes

$$\omega \, \delta\varepsilon = k\bar{w} \, \delta v_\parallel, \tag{5.12}$$

$$\omega \, \delta v_\parallel = k\delta p/\bar{w} - ik^2\gamma_s\delta v_\parallel, \tag{5.13}$$

$$\omega\delta\boldsymbol{v}_\perp + i\frac{\eta}{\bar{w}}k^2\delta\boldsymbol{v}_\perp = 0, \tag{5.14}$$

$$\omega\left(\delta n - \frac{\bar{n}}{\bar{w}}\delta\varepsilon\right) + i\sigma k^2\delta\mu - i\sigma\frac{\bar{\mu}}{\bar{T}}k^2\delta T$$
$$- 2c_T\Omega\bar{T}k\left(1 - \frac{2\bar{\mu}\bar{n}}{\bar{w}}\right)\delta T - 2C\Omega\bar{\mu}k\delta\mu$$
$$+ \frac{2c_T\bar{T}^2\bar{\mu}\Omega k}{\bar{w}^2}\left(\frac{\bar{w}\bar{n}}{\bar{\mu}}\delta\mu + \bar{w}\delta n - \bar{n}\delta\varepsilon - \bar{n}\delta p\right)$$
$$+ \frac{2C\bar{\mu}^3\Omega k}{3\bar{w}^2}\left(\frac{3\bar{w}\bar{n}}{\bar{\mu}}\delta\mu + \bar{w}\delta n - \bar{n}\delta\varepsilon - \bar{n}\delta p\right) = 0, \tag{5.15}$$

where we denoted $\gamma_s \equiv (\zeta + 4\eta/3)/\bar{w}$, $k = |\boldsymbol{k}|$, $\delta v_\parallel = |\delta\boldsymbol{v}_\parallel|$. Below we analyze the possible hydrodynamic modes arising from the equations above.

Hydrodynamic modes in case $\bar{n} = 0$

We have five linearized equations (equation (5.14) is a vector equation) and expect to obtain five dispersion relations. Firstly, we notice that Eq. (5.14) is decoupled from all other equations, and we can write

$$\omega = -i\frac{\eta}{\bar{w}}k^2, \tag{5.16}$$

which is the viscous relaxation mode for the transverse velocity fluctuations. Such ω trivially satisfies all other equations, because we can set all fluctuations but $\delta\boldsymbol{v}_\perp$ to zero. Secondly, the condition $\bar{n} = 0$ decouples Eq. (5.15) from all other equations. Focusing on Eq. (5.15) with $\delta T = 0$, we obtain

$$\omega = 2\Omega\bar{\mu}\left(\frac{C}{\chi} - \frac{C\bar{\mu}^2}{3\bar{w}} - \frac{c_T\bar{T}^2}{\bar{w}}\right)k - i\frac{\sigma}{\chi}k^2, \tag{5.17}$$

where $\chi = (\partial n/\partial\mu)_{\mu=0}$ is the susceptibility. Formally, the dispersion relation above corresponds to the ("isothermal") chiral vortical wave (Jiang et al., 2015). Its speed of propagation is given by the factor in front of k in the linear term. In our case it vanishes, since $\bar{\mu} = \bar{n}/\chi = 0$, and we reproduce the usual charge diffusion. It is important to notice that, since the term $n\boldsymbol{v}$ is missing in the definition of the current in Ref. (Jiang et al., 2015), their case is equivalent to $\bar{n} = 0$, and the wave obtained in (Jiang et al., 2015) should not actually exist.

Finally, in case $\bar{n} = 0$ and arbitrary δT, we have a useful relation $s = c_v c_s^2$, where $c_v = \partial\varepsilon/\partial T$ is the specific heat and $c_s = \sqrt{\partial p/\partial\varepsilon}$ is the speed of sound. This allows us to rewrite equations (5.12), (5.13), (5.15) in the following form

$$\omega\, c_v \delta T = k\bar{w}\, \delta v_\parallel, \tag{5.18}$$

$$\omega\, \delta v_\parallel = k c_v c_s^2 \delta T/\bar{w} - ik^2\gamma_s\delta v_\parallel, \tag{5.19}$$

$$\left(\omega + i\frac{\sigma}{\chi}k^2\right)\delta n = 2c_T\Omega\bar{T}k\delta T, \tag{5.20}$$

where $\bar{\mu}$ was already put to zero. From here we obtain charge diffusion (5.17) together with the usual sound modes,

$$\omega = \pm c_s k - i\frac{\gamma_s}{2}k^2. \tag{5.21}$$

Above we reproduced the 5 familiar modes: two transverse relaxation modes, two sound modes and one thermal diffusion mode. Let us stress once again that the special case $\bar{n} = 0$ does not give rise to any new modes, contrary to (Jiang et al., 2015).

Hydrodynamic modes in case $\bar{n} \neq 0$

It is easy to see that the two transverse relaxation modes are still the same as in $\bar{n} = 0$ case, since $\delta\boldsymbol{v}_\perp$ are still decoupled from other fluctuations. Further, using the standard thermodynamic relations

$$d\varepsilon = T\,ds + \mu\,dn, \quad dp = s\,dT + n\,d\mu, \tag{5.22}$$

$$w = \varepsilon + p = Ts + \mu n, \tag{5.23}$$

we rewrite the Eq. (5.15) in a more convenient form

$$\begin{aligned}
\frac{\bar{n}^2\bar{T}}{\bar{w}}\delta(s/n)&\left(\omega + \frac{2c_T\Omega\bar{T}^2\bar{\mu}k}{\bar{w}} + \frac{2C\Omega\bar{\mu}^3 k}{3\bar{w}}\right)\\
&= i\frac{\sigma k^2}{\bar{n}\bar{T}}\left(\bar{T}\delta p - \bar{w}\delta T\right) - 2c_T\bar{T}\Omega k\left(1 - \frac{2\bar{\mu}\bar{n}}{\bar{w}}\right)\delta T\\
&\quad + \left(\frac{2C\bar{\mu}\bar{s}\bar{T}}{\bar{n}\bar{w}} - \frac{2c_T\bar{T}^2}{\bar{w}}\right)\Omega k\left(\bar{s}\delta T - \delta p\right)\\
&\quad - \left(\frac{2C\bar{\mu}^3\bar{n}}{3\bar{w}^2} + \frac{2c_T\bar{T}^2\bar{\mu}\bar{n}}{\bar{w}^2}\right)\Omega k\delta p.
\end{aligned} \tag{5.24}$$

Let us consider first the case $\delta p = 0$. We get

$$\omega = v_\Omega k - i D_T k^2, \qquad D_T \equiv \frac{\sigma \bar{w}^2}{\bar{n}^2 \bar{T} c_p},$$

$$v_\Omega \equiv 2\Omega \left(\frac{C \bar{\mu} \bar{s}^2 \bar{T}}{\bar{n}^2 c_p} - \frac{c_T \bar{T}}{\bar{n} c_p} (2\bar{w} - 3 \bar{\mu} \bar{n}) \right)$$
$$- \frac{2 \bar{\mu} \Omega}{\bar{w}} \left(c_T \bar{T}^2 + \frac{C}{3} \bar{\mu}^2 \right), \tag{5.25}$$

where $c_p \equiv nT(\partial(s/n)/\partial T)_p$ is the specific heat at constant pressure. The obtained dispersion relation corresponds to the usual thermal diffusion mode with diffusion coefficient D_T, in the limit $\Omega \to 0$. However, in the presence of the vortex, this mode propagates with the speed v_Ω along the vortex. To our knowledge, it has never been discussed in the literature. We call this excitation the "thermal chiral vortical wave". We also note that this excitation is different from the chiral heat wave described in Ref. (Chernodub, 2016).

Physical meaning of the second term for the velocity (5.25) is the subtraction of the difference between the no-drag and Landau frame velocities (Stephanov & Yee, 2016)[2],

$$u^\mu_{\text{Landau}} = u^\mu_{\text{no-drag}} + \frac{2\mu}{w} \left(c_T T^2 + \frac{C}{3} \mu^2 \right) \Omega^\mu$$
$$+ \frac{1}{2w} \left(c_T T^2 + C \mu^2 \right) B^\mu. \tag{5.26}$$

The seeming sign mismatch between the corresponding terms in Eqs. (5.25) and (5.26) comes from the fact that the velocities of the waves are defined with respect to the fluid flow.

To find the other modes, one has to perform a more general calculation, similar to (Kovtun, 2012; Minami & Kunihiro, 2009). In order to do so, we consider a system of coupled equations (5.12), (5.13), and (5.24) and employ the following thermodynamic identities, to reduce the number of independent variables to

---

[2]Since the wave excitations are considered on a background of fluid resting in the direction parallel to k, the wave velocity v_{ND} in the no-drag frame is given by the wave velocity v_{L} in the Landau frame with addition of the extra terms from Eq. (5.26).

three

$$\delta p = \frac{\bar{w}c_s^2}{\gamma}\left(\alpha_p\delta T + \frac{1}{\bar{n}}\delta n\right), \tag{5.27}$$

$$\delta(s/n) = \frac{1}{\gamma\bar{n}}\left(\frac{c_p}{\bar{T}}\delta T - \frac{\bar{w}c_s^2\alpha_p}{\bar{n}}\delta n\right), \tag{5.28}$$

$$\delta\varepsilon = \frac{c_p}{\gamma}\delta T + \frac{\bar{w}}{\bar{n}}\left(1 - \frac{\bar{T}c_s^2\alpha_p}{\gamma}\right)\delta n, \tag{5.29}$$

where $c_s = \sqrt{(\partial p/\partial\varepsilon)_{s/n}}$ is the speed of sound, $\alpha_p = -(1/n)(\partial n/T)_p$ is the thermal expansivity at constant pressure and $\gamma = (\partial(s/n)/\partial T)_p/(\partial(s/n)/\partial T)_n$ is the ratio of specific heats, see Appendix A in (Minami & Kunihiro, 2009) for useful relations between thermodynamic derivatives. With these substitutions made, the full system of equations can be written in the matrix form

$$A\begin{pmatrix} \delta n \\ \delta v_\parallel \\ \delta T \end{pmatrix} = 0, \tag{5.30}$$

where the matrix A is defined as

$$A = \\ \begin{pmatrix} -\frac{\omega\bar{T}c_s^2\alpha_p}{\gamma} - i\frac{\sigma\bar{w}c_s^2 k^2}{\bar{n}^2\gamma} & 0 & \frac{\omega\bar{n}c_p}{\bar{w}\gamma} + i\frac{\sigma\bar{w}k^2}{\bar{n}\bar{T}}\left(1 - \frac{c_s^2\alpha_p\bar{T}}{\gamma}\right) \\ \quad +\alpha_{11}\Omega k & & \quad +\alpha_{13}\Omega k \\ \omega\left(1 - \frac{c_s^2\alpha_p\bar{T}}{\gamma}\right) & -k\bar{n} & \omega\frac{c_p\bar{n}}{\gamma\bar{w}} \\ -\frac{c_s^2 k}{\bar{n}\gamma} & \omega + i\gamma_s k^2 & -\frac{c_s^2\alpha_p}{\gamma}k \end{pmatrix}. \tag{5.31}$$

Here the coefficients in front of Ωk are given by

$$\alpha_{11} = \frac{2Cc_s^2\bar{\mu}^3}{3\gamma\bar{w}}\left(1 - \alpha_p\bar{T} + \frac{3\bar{s}\bar{T}\bar{w}}{\bar{\mu}^2\bar{n}^2}\right) - \frac{2c_T c_s^2\bar{T}^3}{\gamma\bar{w}\bar{n}}\left(\alpha_p\bar{\mu}^2\bar{n} + \bar{s}\right), \tag{5.32}$$

$$\alpha_{13} = -2c_T\bar{T}\left(1 - \frac{2\bar{T}\bar{s}}{\bar{w}}\right) - \frac{2C\bar{\mu}\bar{s}^2\bar{T}}{\bar{n}\bar{w}} + \frac{2c_p\bar{n}\bar{\mu}}{\gamma\bar{w}^2}\left(c_T\bar{T}^2 + \frac{C\bar{\mu}^2}{3}\right)$$
$$+ \frac{c_s^2\alpha_p}{\gamma}\left(-\frac{2c_T\bar{T}^3\bar{s}}{\bar{w}} + \frac{2C\bar{\mu}^3\bar{n}}{3\bar{w}} + \frac{2C\bar{\mu}\bar{s}\bar{T}}{\bar{n}}\right). \tag{5.33}$$

Three dispersion relations can be obtained from the condition $\det(A) = 0$. One of them is Eq. (5.25). The other two are straightforward to obtain, but they are too long to be written in this paper. The speed of propagation of these

modes is a function of Ω and thermodynamic quantities. This mode describes a modified sound propagation. We can demonstrate it by taking the limit $\Omega \to 0$, and recovering the familiar sound modes

$$\omega = \pm c_s k - i\frac{\tilde{\gamma}_s}{2}k^2 \,, \tag{5.34}$$

where

$$\tilde{\gamma}_s = \gamma_s + \frac{\sigma \bar{w}^2}{\bar{n}^2 \bar{T} c_p}\left[\gamma - 1 + c_s^2 \bar{T}\left(\frac{c_p}{\bar{w}} - 2\alpha_p\right)\right] \tag{5.35}$$

is the modified damping rate that coincides with the one obtained in (Minami & Kunihiro, 2009).

5.3 Chiral magnetic wave

It is easy to repeat the analysis for the case of the chiral magnetic wave (Kharzeev & Yee, 2011). To this end we add two terms, $\sigma F^{\mu\nu}u_\nu + \xi_B B^\mu$, to the right-hand side of Eq. (5.4), where ξ_B is the chiral magnetic coefficient in the Landau frame (Neiman & Oz, 2011)

$$\xi_B = C\mu\left(1 - \frac{1}{2}\frac{n\mu}{\varepsilon + p}\right) - \frac{c_T}{2}\frac{n}{\varepsilon + p}T^2 \,. \tag{5.36}$$

We keep the electric field equal to zero, in order to satisfy the current conservation and keep the transverse velocity equations decoupled. Vorticity $\boldsymbol{\omega}$ is defined on the fluctuations of velocity (no vortex background). The Eq. (5.9) becomes

$$\begin{aligned}
\bar{w}\partial_t \delta\boldsymbol{v} + \boldsymbol{\nabla}\delta p - \eta\nabla^2\delta\boldsymbol{v} &- (\zeta + \eta/3)\boldsymbol{\nabla}(\boldsymbol{\nabla}\cdot\delta\boldsymbol{v}) \\
&= (\bar{n}\delta\boldsymbol{v} - \sigma T\boldsymbol{\nabla}(\mu/T) + \xi\boldsymbol{\omega}) \times \boldsymbol{B} \\
&\quad + \sigma\boldsymbol{B}(\boldsymbol{B}\cdot\delta\boldsymbol{v}) - \sigma B^2\delta\boldsymbol{v} \,.
\end{aligned} \tag{5.37}$$

Let us focus first on the equations involving fluctuations in the transverse velocity $\delta\boldsymbol{v}_\perp = (\delta v_\perp^1, \delta v_\perp^2)$. Assuming $\boldsymbol{k}\|\boldsymbol{B}$ for the same reason as for $\boldsymbol{k}$ the vorticity in the previous section, we obtain

$$(-i\bar{w}\omega + \eta k^2 - i\xi kB/2 + \sigma B^2)\delta v_\perp^1 - \bar{n}B\delta v_\perp^2 = 0, \tag{5.38}$$

$$(-i\bar{w}\omega + \eta k^2 - i\xi kB/2 + \sigma B^2)\delta v_\perp^2 + \bar{n}B\delta v_\perp^1 = 0, \tag{5.39}$$

where $B = |\boldsymbol{B}|$. Condition on the zero determinant of the coefficient matrix gives us two modes,

$$\omega = \pm\frac{B\bar{n}}{\bar{w}} - \frac{\xi B}{2\bar{w}}k - i\left(\frac{\eta}{\bar{w}}k^2 + \frac{\sigma}{\bar{w}}B^2\right), \tag{5.40}$$

where the first term corresponds to the Larmor frequency, and the second term describes a general form of the Chiral Alfvén Wave (Yamamoto, 2015) propagating with the speed $v_{\mathrm{CAW}} = \frac{\xi B}{2\bar{w}}$ in the direction opposite to $\boldsymbol{B}$. It is important to notice that the original velocity $v_{\mathrm{CAW}} = c_T\bar{T}^2 B/(2\bar{w})$ obtained in Ref. (Yamamoto, 2015) in the limit $T \gg \mu$ is nothing but the difference in velocities between the no-drag and Landau frames, see (5.26).

Let us switch to the fluctuations of density/temperature along the magnetic field. With the new terms in the current, Eq. (5.15) becomes

$$\begin{aligned}
&\omega\left(\delta n - \frac{\bar{n}}{\bar{w}}\delta\varepsilon\right) + i\sigma k^2\delta\mu - i\sigma\frac{\bar{\mu}}{\bar{T}}k^2\delta T - CBk\delta\mu \\
&+ \frac{c_T\bar{T}^2 Bk}{2\bar{w}^2}\left(\frac{2\bar{w}\bar{n}}{\bar{T}}\delta T + \bar{w}\delta n - \bar{n}\delta\varepsilon - \bar{n}\delta p\right) \\
&+ \frac{C\bar{\mu}^2 Bk}{2\bar{w}^2}\left(\frac{2\bar{w}\bar{n}}{\bar{\mu}}\delta\mu + \bar{w}\delta n - \bar{n}\delta\varepsilon - \bar{n}\delta p\right) = 0.
\end{aligned} \tag{5.41}$$

In the case $\bar{n} = 0$, we obtain the chiral magnetic wave dispersion relation,

$$\begin{aligned}
\omega &= v_\chi k - iD_\chi k^2, \\
v_\chi &\equiv \frac{CB}{\chi} - \frac{c_T\bar{T}^2 B}{2\bar{w}}, \quad D_\chi \equiv \frac{\sigma}{\chi}.
\end{aligned} \tag{5.42}$$

We see that the first term in v_χ, as well as the damping rate D_χ, reproduce the ones from Ref. (Kharzeev & Yee, 2011), while the second term in v_χ is due to the velocity difference (5.26). Let us now generalize the situation to $\bar{n} \neq 0$ and rewrite Eq. (5.41) as

$$\begin{aligned}
&\frac{\bar{n}^2\bar{T}}{\bar{w}}\delta(s/n)\left(\omega + C\bar{\mu}^2\frac{Bk}{2\bar{w}} + c_T\bar{T}^2\frac{Bk}{2\bar{w}}\right) \\
&= i\frac{\sigma k^2}{\bar{n}\bar{T}}\left(\bar{T}\delta p - \bar{w}\delta T\right) + \frac{CB\bar{s}\bar{T}k}{\bar{n}\bar{w}}\left(\bar{s}\delta T - \delta p\right) \\
&+ \frac{c_T B\bar{T}k}{\bar{w}}\delta T - \left(\frac{CB\bar{\mu}^2\bar{n}k}{2\bar{w}^2} + \frac{c_T B\bar{T}^2\bar{n}k}{2\bar{w}^2}\right)\delta p.
\end{aligned} \tag{5.43}$$

With $\delta p = 0$, this leads to a new "thermal chiral magnetic wave" mode

$$\omega = v_\chi^T k - i D_T k^2, \tag{5.44}$$

$$v_\chi^T \equiv \frac{B\bar{T}}{\bar{n}^2 c_p}(c_T + C\bar{s}^2) - \frac{B}{2\bar{w}}\left(c_T \bar{T}^2 + C\bar{\mu}^2\right). \tag{5.45}$$

To our knowledge, this mode has never been discussed in the literature before. The second term for the velocity in (5.45) is, again, due to (5.26).

5.4   Conclusions and outlook

The main result of this work is the discovery of new excitation modes in chiral fluid. They are described by wave solutions given in (5.25) and (5.45), and correspond to heat waves propagating along the vortex or magnetic field due to the quantum anomalies. We reproduced a general form of the chiral Alfvén wave (5.40), the chiral magnetic wave (5.45) and demonstrated that the discussed in the literature chiral vortical wave (Jiang et al., 2015) is absent and simply reduces to the charge diffusion mode (5.17). We identified frame-dependent contributions to the velocities of these waves. In particular, velocity of the chiral Alfvén wave from Ref. (Yamamoto, 2015) is simply a difference between velocities of the no-drag and Landau frames, meaning that the wave should be absent in the no-drag frame. As an outlook, we propose to study a more realistic situation with two charges: one vector and one axial. The equation on the current conservation in (5.2) will be replaced by two equations, $\partial_\mu J_V^\mu = 0$ and $\partial_\mu J_A^\mu = 0$, and, therefore, we expect an additional hydrodynamic mode. The expressions for the chiral magnetic and vortical coefficients will slightly change (Gahramanov et al., 2012; Kalaydzhyan, 2014; Kalaydzhyan & Kirsch, 2011; Neiman & Oz, 2011). The proposed calculations will be straightforward and similar to the presented in this paper.

5.5   Acknowledgements

with the National Aeronautics and Space Administration.

BIBLIOGRAPHY

Abbasi N., Davody A., Hejazi K., Rezaei Z., 2016, Physics Letters B, 762, 23

Abbott B. P., et al., 2016, Physical Review Letters, 116, 061102

Abdikamalov E., Burrows A., Ott C. D., Löffler F., O'Connor E., Dolence J. C., Schnetter E., 2012, ApJ, 755, 111

Abdikamalov E., et al., 2015, ApJ, 808, 70

Agol E., 2000, ApJ, 538, L121

Ahmad Q. R., et al., 2002, Physical Review Letters, 89, 011301

Allamandola L. J., Tielens A. G. G. M., Barker J. R., 1989, ApJS, 71, 733

Arnett W. D., Rosner J. L., 1987, Physical Review Letters, 58, 1906

Audit E., Charrier P., Chièze J. ., Dubroca B., 2002, ArXiv Astrophysics e-prints,

Baganoff F. K., et al., 2003, ApJ, 591, 891

Bahcall J. N., 1964, Physical Review Letters, 12, 300

Battersby C., et al., 2011, A&A, 535, A128

Baumann D., 2013

Berestetski V. B., Lifshitz E. M., Pitaevski L. P., 1982, Quantum Electrodynamics. Vol. 4, 2nd edn. Butterworth-Heinemann, Oxford, UK

Bindi L., Lin C., Ma C., Steinhardt P. J., 2016, Scientific Reports, 6, 38117

Blandford R. D., Begelman M. C., 1999, MNRAS, 303, L1

Boehle A., et al., 2016, ApJ, 830, 17

Bondi H., 1952, MNRAS, 112, 195

Bowen I. S., 1927, Nature, 120, 473

Brandt T. D., Burrows A., Ott C. D., Livne E., 2011, ApJ, 728, 8

Brown R. L., Lockman F. J., Knapp G. R., 1978, ARA&A, 16, 445

Bruenn S. W., 1985, ApJS, 58, 771

Bruenn S. W., et al., 2013, ApJ, 767, L6

Bruenn S. W., et al., 2016, ApJ, 818, 123

Buras R., Rampp M., Janka H.-T., Kifonidis K., 2006, A&A, 447, 1049

Burbidge E. M., Burbidge G. R., Fowler W. A., Hoyle F., 1957, Reviews of Modern Physics, 29, 547

Burrows A., van Riper K. A., 1995, ApJ, 455, 215

Burrows A., Hayes J., Fryxell B. A., 1995, ApJ, 450, 830

Burrows A., Young T., Pinto P., Eastman R., Thompson T. A., 2000, ApJ, 539, 865

Burrows A., Reddy S., Thompson T. A., 2006, Nuclear Physics A, 777, 356

Burrows A., Vartanyan D., Dolence J. C., Skinner M. A., Radice D., 2016, preprint, (arXiv:1611.05859)

Cardall C. Y., Endeve E., Mezzacappa A., 2013, Phys. Rev. D, 87, 103004

Carilli C., Walter F., 2013, preprint, (arXiv:1301.0371)

Cernohorsky J., Bludman S. A., 1994, ApJ, 433, 250

Chernodub M. N., 2016, Journal of High Energy Physics, 1, 100

Crockett N. R., et al., 2014, ApJ, 787, 112

Crowther P. A., 2007, ARA&A, 45, 177

Davis R., 1964, Physical Review Letters, 12, 303

Davis R., Harmer D. S., Hoffman K. C., 1968, Physical Review Letters, 20, 1205

Deaton M. B., et al., 2013, ApJ, 776, 47

Densmore J. D., Urbatsch T. J., Evans T. M., Buksas M. W., 2007, Journal of Computational Physics, 222, 485

Dgani R., Janka H.-T., 1992, A&A, 256, 428

Doeleman S., et al., 2009, in astro2010: The Astronomy and Astrophysics Decadal Survey. (arXiv:0906.3899)

Dolence J. C., Gammie C. F., Mościbrodzka M., Leung P. K., 2009, ApJS, 184, 387

Dunbar D. N. F., Pixley R. E., Wenzel W. A., Whaling W., 1953, Phys. Rev., 92, 649

Eguchi K., et al., 2003, Physical Review Letters, 90, 021802

Erdmenger J., Haack M., Kaminski M., Yarom A., 2009, Journal of High Energy Physics, 1, 055

Foucart F., et al., 2015, Phys. Rev. D, 91, 124021

Fowler R. H., 1926, MNRAS, 87, 114

Gahramanov I., Kalaydzhyan T., Kirsch I., 2012, Phys. Rev. D, 85, 126013

Gillessen S., et al., 2017, ApJ, 837, 30

Gordon M. A., Walmsley C. M., 1990, ApJ, 365, 606

Graciá-Carpio J., et al., 2011, ApJ, 728, L7+

Gruenwald A., 1887, Chemical News, p. 232

Huggins W., Miller W. A., 1864, Philosophical Transactions of the Royal Society of London Series I, 154, 437

Hummer D. G., Storey P. J., 1987, MNRAS, 224, 801

Isachenkov M. V., Sadofyev A. V., 2011, Physics Letters B, 697, 404

Janka H.-T., 1991, PhD thesis, , Technische Universität München, (1991)

Janka H.-T., 1992, A&A, 256, 452

Janka H.-T., Hillebrandt W., 1989, A&AS, 78, 375

Jensen K., Loganayagam R., Yarom A., 2013, Journal of High Energy Physics, 2, 88

Jiang Y., Huang X.-G., Liao J., 2015, Phys. Rev. D, 92, 071501

Just O., Obergaulinger M., Janka H.-T., 2015, MNRAS, 453, 3386

Just O., Obergaulinger M., Janka H.-T., Bauswein A., Schwarz N., 2016, ApJ, 816, L30

Kalaydzhyan T., 2014, Phys. Rev. D, 89, 105012

Kalaydzhyan T., Kirsch I., 2011, Physical Review Letters, 106, 211601

Kasen D., Thomas R. C., Nugent P., 2006, ApJ, 651, 366

Keil M. T., Raffelt G. G., Janka H.-T., 2003, ApJ, 590, 971

Kershaw D. S., 1976, Lawrence Livermore National Laboratory, Livermore, CA, UCRL-78378

Kharzeev D. E., 2015, Annual Review of Nuclear and Particle Science, 65, 150615185930000

Kharzeev D. E., Yee H.-U., 2011, Phys. Rev. D, 83, 085007

Kholupenko E. E., Ivanchik A. V., Varshalovich D. A., 2005, Gravitation and Cosmology, 11, 161

Kochhar R. K., 1991, Journal of the British Astronomical Association, 101, 95

Kovtun P., 2012, Journal of Physics A Mathematical General, 45, 473001

Kuroda T., Takiwaki T., Kotake K., 2016, ApJS, 222, 20

Kwok S., Zhang Y., 2011, Nature, 479, 80

Landau L., Lifshitz E., 1977, Quantum Mechanics: Non-Relativistic Theory Vol. 3, 3rd edn. Pergamon Press, Oxford, UK

Landsteiner K., Megías E., Pena-Benitez F., 2011, Physical Review Letters, 107, 021601

LeBlanc J. M., Wilson J. R., 1970, ApJ, 161, 541

Leger A., Puget J. L., 1984, A&A, 137, L5

Leitherer C., et al., 1999, ApJS, 123, 3

Lentz E. J., et al., 2015, ApJ, 807, L31

Levermore C. D., 1984, J. Quant. Spec. Radiat. Transf., 31, 149

Liebendörfer M., Rampp M., Janka H.-T., Mezzacappa A., 2005, ApJ, 620, 840

Lindquist R. W., 1966, Annals of Physics, 37, 487

Livne E., Burrows A., Walder R., Lichtenstadt I., Thompson T. A., 2004, ApJ, 609, 277

Lockyer J. N., 1868, Proceedings of the Royal Society of London Series I, 17, 91

Lucy L. B., 2005, A&A, 429, 19

Mahadevan R., 1998, Nature, 394, 651

Mahadevan R., Narayan R., Krolik J., 1997, ApJ, 486, 268

Marek A., Janka H.-T., 2009, ApJ, 694, 664

Marrone D. P., Moran J. M., Zhao J.-H., Rao R., 2007, ApJ, 654, L57

McCrea W. H., 1950, Nature, 166, 884

McKinney J. C., Tchekhovskoy A., Blandford R. D., 2012, MNRAS, 423, 3083

Melson T., Janka H.-T., Marek A., 2015a, ApJ, 801, L24

Melson T., Janka H.-T., Bollig R., Hanke F., Marek A., Müller B., 2015b, ApJ, 808, L42

Mezzacappa A., Bruenn S. W., 1993a, ApJ, 405, 637

Mezzacappa A., Bruenn S. W., 1993b, ApJ, 405, 669

Mezzacappa A., Bruenn S. W., 1993c, ApJ, 410, 740

Mezzacappa A., Matzner R. A., 1989, ApJ, 343, 853

Mihalas D., Mihalas B. W., 1984, Foundations of radiation hydrodynamics

Minami Y., Kunihiro T., 2009, Progress of Theoretical Physics, 122, 881

Minerbo G. N., 1978, J. Quant. Spec. Radiat. Transf., 20, 541

Miransky V. A., Shovkovy I. A., 2015, Phys. Rep., 576, 1

Morison I., 2008, Introduction to Astronomy and Cosmology

Mösta P., et al., 2014, ApJ, 785, L29

Müller B., 2015, MNRAS, 453, 287

Müller B., Janka H.-T., 2015, MNRAS, 448, 2141

Müller B., Marek A., Janka H.-T., Dimmelmeier H., 2012a, in Pogorelov N. V., Font J. A., Audit E., Zank G. P., eds, Astronomical Society of the Pacific Conference Series Vol. 459, Numerical Modeling of Space Plasma Slows (AS-TRONUM 2011). p. 137 (arXiv:1112.1920)

Müller B., Janka H.-T., Marek A., 2012b, ApJ, 756, 84

Murphy J. W., Burrows A., 2008, ApJ, 688, 1159

Murphy E. J., et al., 2011, ApJ, 737, 67

Narayan R., Yi I., 1995, ApJ, 452, 710

Neiman Y., Oz Y., 2011, Journal of High Energy Physics, 3, 23

Novikov I. D., Thorne K. S., 1973, in Dewitt C., Dewitt B. S., eds, Black Holes (Les Astres Occlus). pp 343–450

O'Connor E., 2015, ApJS, 219, 24

O'Connor E., Ott C. D., 2010, Classical and Quantum Gravity, 27, 114103

O'Connor E., Ott C. D., 2011, ApJ, 730, 70

O'Connor E., Ott C. D., 2013, ApJ, 762, 126

Ohnishi N., Kotake K., Yamada S., 2006, ApJ, 641, 1018

Osterbrock D. E., Ferland G. J., 2006, Astrophysics of gaseous nebulae and active galactic nuclei, first edn. University Science Books, Mill Valley, CA

Ott C. D., Burrows A., Dessart L., Livne E., 2008, ApJ, 685, 1069

Ott C. D., et al., 2012, Phys. Rev. D, 86, 024026

Ott C. D., O'Connor E. P., Gossan S., Abdikamalov E., Gamma U. C. T., Drasco S., 2013a, Nuclear Physics B Proceedings Supplements, 235, 381

Ott C. D., et al., 2013b, ApJ, 768, 115

O'Connor E. P., Couch S. M., 2018, ApJ, 854, 63

Phinney E. S., 1981, in Colgate S. A., ed., ESA Special Publication Vol. 161, ESA Special Publication. p. 337

Planck Collaboration et al., 2011a, A&A, 536, A21

Planck Collaboration et al., 2011b, A&A, 536, A25

Pomraning G. C., 1969, J. Quant. Spec. Radiat. Transf., 9, 407

Pomraning G. C., 1983, ApJ, 266, 841

Pons J. A., Ibáñez J. M., Miralles J. A., 2000, MNRAS, 317, 550

Puxley P. J., Mountain C. M., Brand P. W. J. L., Moore T. J. T., Nakai N.,

1997, ApJ, 485, 143

Quataert E., 2002, ApJ, 575, 855

Quataert E., 2004, ApJ, 613, 322

Quataert E., Gruzinov A., 2000, ApJ, 539, 809

Radice D., Abdikamalov E., Rezzolla L., Ott C. D., 2013, Journal of Computational Physics, 242, 648

Radice D., Ott C. D., Abdikamalov E., Couch S. M., Haas R., Schnetter E., 2016, ApJ, 820, 76

Rampp M., Janka H.-T., 2000, ApJ, 539, L33

Rampp M., Janka H.-T., 2002, A&A, 396, 361

Rees M. J., Begelman M. C., Blandford R. D., Phinney E. S., 1982, Nature, 295, 17

Remijan A., Seifert N. A., McGuire B. A., 2016, in 71st International Symposium on Molecular Spectroscopy. p. FB11, doi:10.15278/isms.2016.FB11

Ressler S. M., Quataert E., Stone J. M., 2018, MNRAS,

Richers S., Kasen D., O'Connor E., Fernández R., Ott C. D., 2015, ApJ, 813, 38

Richers S., Ott C. D., Abdikamalov E., O'Connor E., Sullivan C., 2017, Phys. Rev. D, 95, 063019

Roberts L. F., Ott C. D., Haas R., O'Connor E. P., Diener P., Schnetter E., 2016, ApJ, 831, 98

Rosswog S., Liebendörfer M., 2003, MNRAS, 342, 673

Ruffert M., Janka H.-T., Schaefer G., 1996, A&A, 311, 532

Salpeter E. E., 1952, ApJ, 115, 326

Sanders D. B., Soifer B. T., Elias J. H., Madore B. F., Matthews K., Neugebauer G., Scoville N. Z., 1988, ApJ, 325, 74

Sądowski A., Narayan R., Tchekhovskoy A., Zhu Y., 2013, MNRAS, 429, 3533

Scheck L., Kifonidis K., Janka H.-T., Müller E., 2006, A&A, 457, 963

Schinder P. J., Bludman S. A., 1989, ApJ, 346, 350

Scoville N., Murchikova L., 2013, ApJ, 779, 75

Scoville N., et al., 2015, ApJ, 800, 70

Sejnowski T. J., Hjellming R. M., 1969, ApJ, 156, 915

Shakura N. I., Sunyaev R. A., 1973, A&A, 24, 337

Shen H., Toki H., Oyamatsu K., Sumiyoshi K., 1998, Nuclear Physics A, 637, 435

Shibata M., Sekiguchi Y., 2012, Progress of Theoretical Physics, 127, 535

Shibata M., Kiuchi K., Sekiguchi Y., Suwa Y., 2011, Progress of Theoretical Physics, 125, 1255

Skinner M. A., Burrows A., Dolence J. C., 2016, ApJ, 831, 81

Smit J. M., Cernohorsky J., Dullemond C. P., 1997, A&A, 325, 203

Smit J. M., van den Horn L. J., Bludman S. A., 2000, A&A, 356, 559

Son D. T., Surówka P., 2009, Physical Review Letters, 103, 191601

Stephanov M. A., Yee H.-U., 2016, Physical Review Letters, 116, 122302

Storey P. J., Hummer D. G., 1995a, MNRAS, 272, 41

Storey P. J., Hummer D. G., 1995b, VizieR Online Data Catalog, 6064, 0

Sumiyoshi K., Yamada S., 2012, ApJS, 199, 17

Sumiyoshi K., Yamada S., Suzuki H., Shen H., Chiba S., Toki H., 2005, ApJ, 629, 922

Sumiyoshi K., Takiwaki T., Matsufuru H., Yamada S., 2015, ApJS, 216, 5

Thomson W., 1871, Nature, 4, 261

Thorne K. S., 1981, MNRAS, 194, 439

Vaytet N. M. H., Audit E., Dubroca B., Delahaye F., 2011, J. Quant. Spec. Radiat. Transf., 112, 1323

Vilenkin A., 1979, Phys. Rev. D, 20, 1807

Volovik G. E., 2006, Int. Ser. Monogr. Phys., 117, 1

Wadiak E. J., Sarazin C. L., Brown R. L., 1983, ApJS, 53, 351

Wilson J. R., Couch R., Cochran S., Le Blanc J., Barkat Z., 1975, in Bergman P. G., Fenyves E. J., Motz L., eds, Annals of the New York Academy of Sciences Vol. 262, Seventh Texas Symposium on Relativistic Astrophysics. pp 54–64, doi:10.1111/j.1749-6632.1975.tb31420.x

Wolf S., Henning T., Stecklum B., 1999, A&A, 349, 839

Wollaeger R. T., van Rossum D. R., Graziani C., Couch S. M., Jordan IV G. C., Lamb D. Q., Moses G. A., 2013, ApJS, 209, 36

Yamada S., 1997, ApJ, 475, 720

Yamamoto N., 2015, Physical Review Letters, 115, 141601

Yuan F., Narayan R., 2014, ARA&A, 52, 529

Yun M., Scoville N., Shukla H., 2004, in Aalto S., Huttemeister S., Pedlar A., eds, Astronomical Society of the Pacific Conference Series Vol. 320, The Neutral ISM in Starburst Galaxies. p. 27

Zakharov V. I., 2013, in Kharzeev D., Landsteiner K., Schmitt A., Yee H.-U., eds, Lecture Notes in Physics, Berlin Springer Verlag Vol. 871, Lecture Notes in Physics, Berlin Springer Verlag. p. 295 (arXiv:1210.2186), doi:10.1007/978-3-642-37305-3_11

Zhao J.-H., Morris M. R., Goss W. M., 2016, ApJ, 817, 171